Measurements of the W-pair production rate and the W mass using four-jet events at LEP

Daniël van Dierendonck

Measurements of the W-pair production rate and the W mass using four-jet events at LEP

Measurements of the W-pair production rate and the W mass using four-jet events at LEP

ACADEMISCH PROEFSCHRIFT

TER VERKRIJGING VAN DE GRAAD VAN DOCTOR
AAN DE UNIVERSITEIT VAN AMSTERDAM
OP GEZAG VAN DE RECTOR MAGNIFICUS
PROF. MR. P. F. VAN DER HEIJDEN
TEN OVERSTAAN VAN EEN DOOR HET COLLEGE VAN PROMOTIES
INGESTELDE COMMISSIE, IN HET OPENBAAR TE VERDEDIGEN
IN DE AULA DER UNIVERSITEIT
OP VRIJDAG 15 NOVEMBER 2002, TE 10:00 UUR

door

Daniël Nicolaas van Dierendonck

geboren te Maastricht

Promotor: Prof. Dr. F. Linde
Co-Promotor: Dr. Ir. P. de Jong

Faculteit der Natuurwetenschappen, Wiskunde en Informatica

ISBN: 90-6464-509-4

The work described in this thesis is part of the research program of the 'Nationaal Instituut voor Kernfysica en Hoge-Energie Fysica' (NIKHEF). The author was financially supported by the 'Stichting voor Fundamenteel Onderzoek der Materie' (FOM).

Cover: excerpts from a letter from Professor G. 't Hooft regarding the renormalization of a model involving hadrons.

Aan mijn ouders

Contents

Chapter 1

Introduction

Perhaps the most interesting challenge in physics is to describe as much of the world as possible with a model as simple and general as possible. Certainly the most successful model to date is the unimaginatively but perhaps appropriately called Standard Model. The essence of this theory, the Lagrangian, fits on a single page. However this compact theory successfully describes all electromagnetic, weak and strong interactions in a quantum mechanically correct way and is consistent with special relativity. It is hard to overestimate the magnitude of this accomplishment or the scope of its applications. The Standard Model ultimately describes processes ranging from chemical reactions throughout our body, through nuclear fusion in the sun, to electromagnetic processes in our television sets. Many tests of the theory have been performed, often with astonishing precision. Up to now, the theory has always been able to describe the observed phenomena - to the disappointment of some physicists. The main part of the model that still requires experimental verification is the confirmation of the existence of the Higgs boson. This crucial particle is predicted by the Standard Model, but has not yet been observed directly. Although a surprise would be most welcome, there are indications that the Higgs is just around the corner and will be found in the not so distant future.

The success of the Standard Model is especially intriguing as we know that it is not a complete theory: gravity is not included. At some scale the theory's description of nature should therefore break down. To gain insight into the missing part of the theory, it is essential to continue to challenge it experimentally. Therefore, accurate measurement are needed to verify Standard Model predictions and its fundamental properties.

In 1983, the existence of the W boson was demonstrated by the UA1 collaboration. In the Standard Model, the W boson is the charged mediator of the electroweak force. In this thesis precision measurements involving W bosons are presented. The first measurement described is the W pair production rate in e^+e^- collisions. This production rate is highly sensitive to possible anomalies in certain interactions, for example in the ZWW coupling.

Subsequently, the collected W pairs have been used to extract the mass of the W boson. This mass is a fundamental parameter of the Standard Model which is not fixed by theory.

This alone justifies a measurement of the W mass. In addition, the Standard Model can be tested to a level of great precision by comparing the directly measured W mass with the indirect W mass prediction. This prediction is obtained by performing a Standard Model fit to several precisely measured observables.

The layout of this thesis is as follows. In Chapter 2, the theory is briefly discussed. In Chapter 3, the LEP accelerator and the L3 detector are described, followed in Chapter 4 by an overview of some specific analysis methods and tools used to perform the measurements. In the next Chapter the selection of W pair events and the determination of the W pair production rate are described. Also in Chapter 5, the W mass is determined from the production rate at the center-of-mass energy where this rate is sensitive to the W mass: i.e. at the W-pair production threshold. In Chapter 6, the previously selected events are used for a direct measurement of the W mass. Finally, in Chapter 7, the results are discussed in the framework of the Standard Model. Also, some implications of the measurements for possible physics beyond the Standard Model are given.

Chapter 2

Theory

2.1 Weak Interactions and the Standard Model

Weak nuclear interactions play a role in nuclear fusion inside the sun, phenomena like β decay (a form of radioactivity involving the transition of a neutron into a proton: $\mathrm{n} \rightarrow \mathrm{pe}\bar{\nu}_e$), and certain decays of unstable particles like $\mu \rightarrow \mathrm{e}\bar{\nu}_e\nu_\mu$. The slowness of β decay, or the relatively long muon lifetime, implies that these interactions are, as their name suggests, much weaker than the other interactions that play a role in atoms and nuclei: electromagnetism and the strong nuclear interactions.

Fermi wrote this interaction as a 4-point interaction with strength G_F, the product of two currents connected with a vector interaction [1]. This is graphically shown in Figure 2.1 for the example of muon decay. A generalization of this interaction contains interactions of scalar, pseudo-scalar, vector, axial-vector and tensor type. Experiments on the shape of the energy spectrum and polarization of electrons from β decay and muon decay [2, 3], the discovery of parity violation in weak interactions [4], and the determination of the helicity of the neutrino [5], led to the conclusion that the interaction was of the V-A, or vector minus axial-vector type [6]. The Fermi constant G_F is precisely determined from the lifetime of the muon, and equals $G_\mathrm{F} = 1.16639(1) \times 10^{-5}$ GeV^{-2} [7]. However, in this simple formulation, typical weak cross sections are proportional to s, the center-of-mass energy squared, and thus violate unitarity at high energies.

Following the ansatz of Yukawa for strong interactions, Klein proposed the W boson as a mediator of the weak charged current interactions [8]. A diagram of muon decay in this approach is shown in the right section of Figure 2.1. The equivalence of the two approaches at low energies leads to a relation between G_F on the one hand, and the W boson mass m_W and the coupling strength g on the other hand:

$$\frac{G_\mathrm{F}}{\sqrt{2}} \approx \frac{g^2}{8m_\mathrm{W}^2}. \tag{2.1}$$

This suggests that the weakness of the weak interactions at low energies could, at least par-

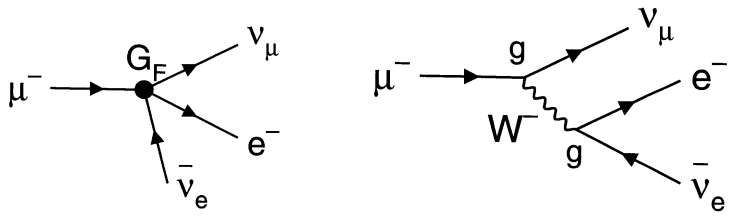

Figure 2.1: *Left: muon decay as written down by Fermi: a 4-point interaction with strength G_F. Right: muon decay mediated by a weak vector boson W, with coupling strength g to the fermions.*

tially, be caused by a large W boson mass. In equation 2.1, the numerical factors appearing left and right are due to Fermi's choice of normalization of the coupling, whereas the fact that the equation is quadratic in g, but linear in G_F, shows the splitting of Fermi's 4-point interaction into two separate vertices and a propagator.

A proper gauge theory of weak interactions can be constructed by a unified description of weak and electromagnetic interactions, as developed by Glashow, Weinberg and Salam [9]. This theory is now known as the Standard Model of electroweak interactions (or, together with QCD, simply as the Standard Model). Its mathematical consistency, i.e. renormalizability and respect of unitarity, was proven by Veltman and 't Hooft [10]. The Standard Model consists of a number of crucial elements:

- W bosons couple to a SU(2) doublet of left-handed fermions (for quarks the weak eigenstates are mixtures of the mass eigenstates, the mixing matrix is known as the Cabibbo-Kobayashi-Maskawa, or CKM, matrix);

- Lepton universality: the gauge bosons couple identically to the leptons from all three families. Lepton number is conserved;

- The existence of weak neutral currents mediated by Z bosons, with flavor-diagonal couplings, is predicted.

In the Standard Model Lagrangian, four massless spin-1 gauge bosons, W^+, W^-, W^3 and B appear. The physical Z bosons and photons are mixtures of the neutral bosons W^3 and B, the mixing angle θ_W is known as the weak mixing angle (sometimes denoted Weinberg angle). This mixing angle relates the strength of the electromagnetic coupling α, expressed as the electron charge $e = \sqrt{4\pi\alpha}$, to the strength of the weak coupling g:

$$e = g \sin\theta_W. \tag{2.2}$$

The gauge bosons acquire their mass through the Higgs mechanism [11]: a scalar field with a non-zero vacuum expectation value gives mass to the W and Z bosons, while leaving the photon massless. The W and Z boson masses are related in the following way:

$$\rho(1 - \sin^2\theta_W) = \rho\cos^2\theta_W = \frac{m_{\mathrm{W}}^2}{m_{\mathrm{Z}}^2}. \tag{2.3}$$

In the simplest formulation of the theory, the remainder of the scalar field is one neutral spin-0 boson with unknown mass, the Higgs boson, and at tree level $\rho = 1$. In more extended scenario's, more Higgs bosons can exist, and in general $\rho \neq 1$. Experimentally, ρ is found to be very close to 1, which puts limits on other Higgs scenario's. Also the fermions acquire their mass through their couplings with the Higgs field.

The Standard Model is a non-Abelian gauge theory: self-interactions are present between the gauge bosons in the form of triple gauge couplings WWγ and WWZ, and quartic gauge couplings WW$\gamma\gamma$, WWZγ, WWZZ, and WWWW.

Using the relations of equation 2.1 and 2.2, and keeping in mind that $e = \sqrt{4\pi\alpha}$, one derives at tree level the following expression for m_{W}:

$$m_{\mathrm{W}} = \sqrt{\frac{\pi\alpha}{\sqrt{2}G_{\mathrm{F}}}}/\sin\theta_W \approx \frac{37.3}{\sin\theta_W}\ \mathrm{GeV} \tag{2.4}$$

Here the mass is given in units of GeV, which is correct since the units in this thesis are chosen such that $\hbar = c = 1$. Weak neutral currents were discovered in neutrino scattering experiments [12]; the rate of charged current to neutral current interactions in neutrino and anti-neutrino beams gave an estimate of $\sin\theta_W$ and thus an estimate of m_{W} and m_{Z}. The W and Z bosons were discovered in 1983 by the UA1 and UA2 experiments at the Sp$\bar{\mathrm{p}}$S collider at CERN, close to the predicted masses [13]; an example of an event is shown in Figure 2.2. These discoveries provided a splendid confirmation of the Standard Model.

The strong nuclear interactions are also described by a gauge theory called quantum chromodynamics, or QCD [14]. Also QCD is non-Abelian. It is based on the symmetry group $\mathrm{SU(3)_C}$, where C stands for color, the "charge" that generates strong interactions. The mediators of the strong interactions are the massless gluons, their coupling strength is denoted as α_s.

In the Standard Model, all matter consists of the quarks and leptons listed in Table 2.1. These building blocks of matter are "glued" together by forces which are carried by boson fields as listed in Table 2.2. The gravitational force is outside the scope of the Standard Model, in fact a consistent quantum theory combining gravitation and the other fundamental interactions is still lacking. Due to its weakness at the energies attainable in current and near-future accelerators, it plays virtually no role in the phenomenology of experiments at those accelerators. In certain models involving large extra dimensions, however, interactions of quarks and leptons with real or virtual gravitons may lead to experimentally observable effects [15, 16].

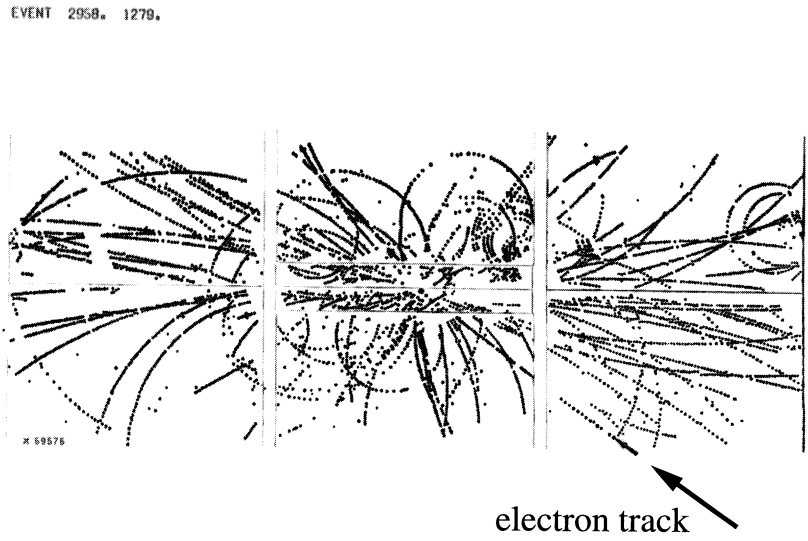

Figure 2.2: *A $W \rightarrow e\nu$ event recorded in the UA1 detector. The arrow, bottom right, points to the track of a high p_T electron from W decay.*

Fermion families				Electric charge [e]
Quarks	u	c	t	$+\frac{2}{3}$
	d	s	b	$-\frac{1}{3}$
Leptons	e	μ	τ	-1
	ν_e	ν_μ	ν_τ	0

Table 2.1: *Fermions in the Standard Model.*

Interaction	Boson	Electric charge [e]
Electromagnetic	γ	0
Weak	W^+	+1
	W^-	-1
	Z^0	0
Strong	g	0
	H^0	0

Table 2.2: *Bosons in the Standard Model.*

The search for the Higgs boson remains one of the most important tasks of elementary particle physics. The direct searches have excluded a Standard Model Higgs boson with a mass less than 114.1 GeV at 95% confidence level [17]. The final LEP data in 2000, however, had a tantalizing result: a hint for a signal of a Higgs boson with a mass of 115-116 GeV with a significance of 2.1 standard deviations, corresponding to a probability of a background fluctuation of 3.4% [17]. Since this hint is insufficient for a discovery, the current (highly unsatisfactory) situation is that the existence of a 115-116 GeV Higgs boson can neither be confirmed nor excluded, and further tests have to wait for high luminosity at the Tevatron (Fermilab, Chicago) or LHC (CERN, Geneva) colliders in the future.

The Standard Model has a number of input parameters whose values are not predicted but which are relevant for numerical calculations within the Standard Model. For the electroweak gauge sector, these consist of three parameters that can be chosen from the set $\{\alpha, m_{\mathrm{Z}}, m_{\mathrm{W}}, G_{\mathrm{F}}, \theta_W\}$. It is convenient to chose well measured ones, such as α, m_{Z} and G_{F}. When three have been chosen, the values of the other parameters are fixed at tree level. For the strong sector, α_s is a free parameter, and for the Higgs sector so is the Higgs boson mass m_{H}. Finally, the masses of the quarks and leptons, and four parameters in the CKM matrix are free. Within the Standard Model, the neutrino's are massless; an assumption that may need to be revised in the light of recent neutrino oscillation results [18].

Accurate quantitative calculations in the Standard Model need to go beyond the tree level, and take into account electromagnetic and weak radiative corrections. These corrections

modify equation 2.4 (and making use of equation 2.3) in the following way:

$$m_{\mathrm{W}}^2(1-\frac{m_{\mathrm{W}}^2}{m_{\mathrm{Z}}^2}) = \frac{\pi\alpha}{\sqrt{2}G_{\mathrm{F}}} \times \frac{1}{1-\Delta r} \tag{2.5}$$

The correction Δr has an electromagnetic component, denoted as $\Delta\alpha$, and a weak component Δr_w:

$$\frac{1}{1-\Delta r} = \frac{1}{1-\Delta\alpha(m_{\mathrm{Z}}^2)} \times \frac{1}{1-\Delta r_w} \tag{2.6}$$

The electromagnetic contribution arises from the photon self energy: modifications to the photon propagator due to fermion loops. This, in fact, can be interpreted as a dependence of the electromagnetic coupling strength α on the scale s:

$$\alpha \equiv \alpha(0) \rightarrow \alpha(s) = \frac{\alpha}{1-\Delta\alpha(s)}. \tag{2.7}$$

The coupling α is said to be running. All charged fermions contribute to $\Delta\alpha(s)$. The top contribution is very small, due to the large top mass. The contribution of the charged leptons is calculable with negligible uncertainty. The contributions of the light quarks, however, do introduce an uncertainty on $\alpha(s)$ due to the unknown quark masses, and are calculated by dispersion integral techniques from the measured cross section of $\mathrm{e^+e^-}$ annihilation into hadrons at low $\sqrt{s}$ [19]. Combining the leptonic and hadronic contributions, α at the m_{Z} scale is calculated to be [19]:

$$\frac{1}{\alpha(m_{\mathrm{Z}}^2)} = 128.936 \pm 0.046 \tag{2.8}$$

as compared to $1/\alpha(0) = 137.03599976(50)$ [7]. Virtually all electromagnetic corrections are absorbed in the running of α, so that equation 2.5 can also be written as:

$$m_{\mathrm{W}}^2(1-\frac{m_{\mathrm{W}}^2}{m_{\mathrm{Z}}^2}) = \frac{\pi\alpha(m_{\mathrm{Z}}^2)}{\sqrt{2}G_{\mathrm{F}}} \times \frac{1}{1-\Delta r_w}, \tag{2.9}$$

where Δr_w represent only the weak corrections.

Weak corrections arise due to vacuum polarization (oblique corrections), vertex and box corrections; examples of weak corrections to the W propagator due to the top and bottom quarks and the Higgs boson are shown in Figure 2.3. A rigorous treatment of all corrections is outside the scope of this thesis. An approximate formula for the dependence of Δr_w on the top quark and Higgs boson masses, assuming $m_{\mathrm{H}} \gg m_{\mathrm{W}}$, is as follows [20, 21]:

$$\begin{aligned}\Delta r_w \;= -\tfrac{G_{\mathrm{F}}m_{\mathrm{W}}^2}{8\sqrt{2}\pi^2} \;\Big[&3\cot^2\theta_W\frac{m_{\mathrm{t}}^2}{m_{\mathrm{W}}^2} + 2(\cot^2\theta_W - \frac{1}{3})\ln\frac{m_{\mathrm{t}}^2}{m_{\mathrm{W}}^2} - \\ &\frac{11}{3}\ln\frac{m_{\mathrm{H}}^2}{m_{\mathrm{W}}^2} + \\ &\frac{4}{3}\ln\cos^2\theta_W + \cot^2\theta_W + \frac{41}{18} + \ldots\Big].\end{aligned} \tag{2.10}$$

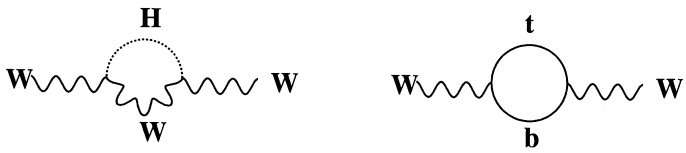

Figure 2.3: *Corrections to the W boson propagator (oblique corrections) involving the Higgs boson and the top and bottom quarks.*

It is interesting to note that heavy particles do not decouple: Δr_w is quadratically dependent on m_{t}, and thus quite sensitive to it. The dependence on the Higgs mass, however, is only logarithmic; this accidental effect is known as "Veltman screening" [22]. Thus a 40% uncertainty on the Higgs mass has the same effect on Δr_w as a 3% uncertainty on the top mass.

The uncertainty on $\alpha(m_{\mathrm{Z}}^2)$ plays a small but non-negligible role in the Standard Model fit: it leads to a 0.2 GeV error on the top quark mass, or a 0.1 error on the logarithm of the Higgs boson mass. Compared to the situation of a few years ago, considerable progress has been obtained using the results of the measurements of the hadronic cross section in $\mathrm{e^+e^-}$ annihilation by the BES experiment at the BEPC collider in Beijing [23].

The need for electroweak corrections is experimentally well established [24]. Using the measurements of many electroweak observables at LEP and SLD, the measurements of $\sin^2\theta_W$ in deep inelastic scattering, and the measurements of the top quark and W boson masses at the Tevatron, a combined fit to the Standard Model parameters can be done. A fit to all data except the direct top quark mass measurements predicts $m_{\mathrm{t}} = 181^{+11}_{-9}$ GeV [25], which agrees well with the direct Tevatron measurement $m_{\mathrm{t}} = 174.3 \pm 5.1$ GeV [26]. A fit to all data except the direct W mass measurements predicts $m_{\mathrm{W}} = 80.379 \pm 0.023$ GeV [25]. Clearly, a direct measurement with similar uncertainty is very interesting as a Standard Model test. In supersymmetric models a large number of new particles appear as bosonic/fermionic partners of the Standard Model fermions and bosons. These particles will contribute to the radiative corrections Δr_w of equation 2.9, and may, depending on their mass, give up to 100 MeV shifts in m_{W} in the Minimal Supersymmetric Standard Model [27]. The Tevatron experiments have measured $m_{\mathrm{W}} = 80.454 \pm 0.060$ GeV [28]. A fit of all data including the direct W mass measurements will constrain the Higgs boson mass. It is interesting to note that the dependence of m_{W} on m_{H} is less influenced by the uncertainty on $\alpha(m_{\mathrm{Z}}^2)$ than most other observables [24].

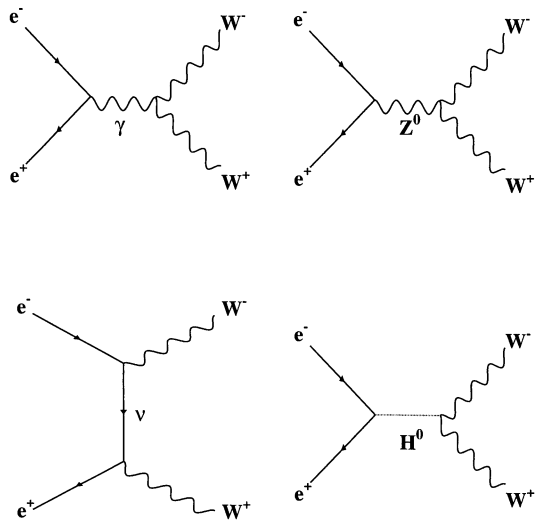

Figure 2.4: $e^+e^- \rightarrow W^+W^-$ *Feynman diagrams. The Higgs-boson-exchange diagram is usually ignored in calculations, while the other three are referred to as the CC03 set.*

2.2 W-Pair Production in e^+e^- Collisions

Production of W pairs is possible in e^+e^- collisions at center-of-mass energies above approximately $2m_W$. Experimentally, e^+e^- colliders offer significant advantages over pioneering $p\bar{p}$ machines from the point of view of precision studies of the W boson. The backgrounds for $e^+e^- \rightarrow W^+W^-$ event selections do not dominate and allow the study of all decay modes of the W in a clean way. An e^+e^- collision has a well-defined initial state, which makes it possible to reconstruct the full event kinematics, unlike $p\bar{p}$ experiments which are restricted to transverse energies, momenta and masses.

The $e^+e^- \rightarrow W^+W^-$ process proceeds through the four diagrams shown in Figure 2.4. The contribution of the s-channel Higgs exchange diagram is strongly suppressed relative to the other diagrams due to the small electron-Higgs Yukawa coupling, and thus usually ignored [1]. The remaining three diagrams constitute the "CC03 set", where "CC" stands for "charged current".

[1] However, when the electron mass is not neglected in calculations of the cross section, this diagram is needed in principle to save unitarity.

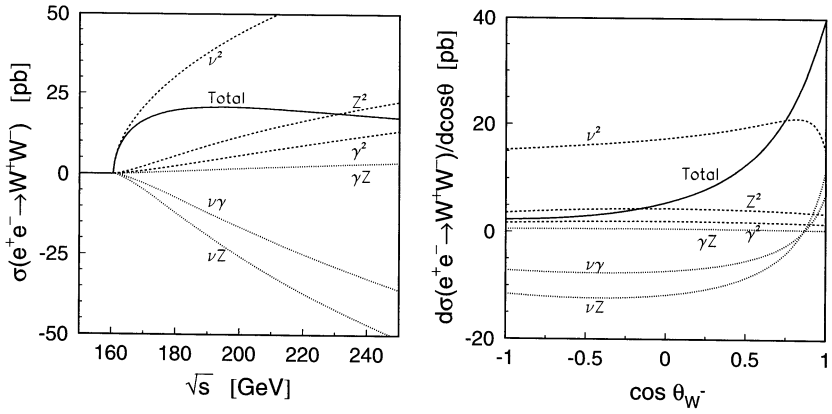

Figure 2.5: *Left: contribution of the three diagrams and their interferences to the total cross section as a function of* $\sqrt{s}$. *Right: contribution of the three diagrams and their interferences to the differential cross section* $d\sigma/d\cos\theta_{W^-}$ *at* $\sqrt{s} = 189$ GeV. *The cross sections shown in both figures are calculated in the zero-width approximation.*

The matrix element is thus a sum of three contributions: t-channel neutrino-exchange, and s-channel γ and Z exchange involving the WWγ and WWZ vertices.

In Figure 2.5, the individual contributions of the three diagrams and their interferences to the cross section are shown. Close to threshold, the t-channel neutrino exchange diagram dominates; above threshold also the s-channel diagrams and their interferences become important and are in fact necessary to preserve unitarity. A measurement of the cross section is thus a direct test of the non-Abelian structure of the electroweak gauge group.

In the right figure of Figure 2.5, the differential cross section $d\sigma/d\cos\theta_{W^-}$ is shown. Clearly, W boson production is enhanced at high values of $|\cos\theta_{W^-}|$, i.e. close to the beam pipe. For the produced W-pairs, nine helicity states $(\lambda, \bar{\lambda})$ are possible. The states $(+-)$ and $(-+)$ can be reached only through t-channel neutrino exchange. The polarization of the W influences the angular distributions of its decay products, which will be further treated in the next section. It should be noted that anomalous (non-Standard Model) contributions to the gauge couplings affect the production angle of the W bosons as well as their polarization states.

In the previous paragraphs WW production has been treated in the zero-width approximation ($\Gamma_{\mathrm{W}} = 0$). However, the W boson has a finite width of about 2.1 GeV. This modifies the production cross section as shown in Figure 2.6; the finite width softens the sharp rise of the cross section at threshold $\sqrt{s} \approx 2m_{\mathrm{W}}$.

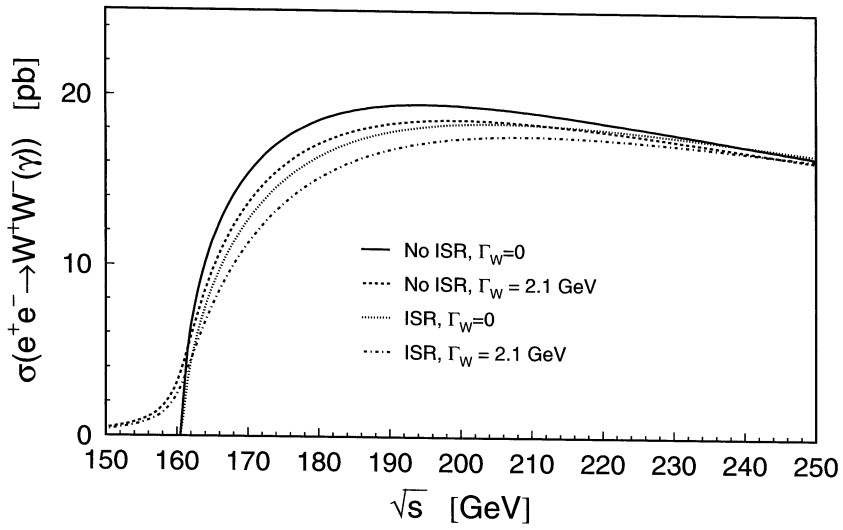

Figure 2.6: *Effects of the finite W width and ISR corrections on the total CC03 cross section for* $e^+e^-\to W^+W^-$.

2.3 W Decay

Once produced, the W bosons can decay into the kinematically allowed SU(2) doublets $f\bar{f}'$. W bosons can decay hadronically, $W^\pm \to q\bar{q}'$, or leptonically, $W^+ \to \ell^+\nu$ and $W^- \to \ell^-\bar{\nu}$. In the remainder of this thesis these decays will simply be written as $W \to q\bar{q}'$, or $W \to q\bar{q}$ for short, and $W \to \ell\nu$, for both W^+ and W^-. The partial width of the decay $W \to f\bar{f}'$ is given by:

$$\Gamma(W \to f\bar{f}') = \frac{G_F m_W^3}{6\pi\sqrt{2}} |V_{f\bar{f}'}|^2 R_{QCD}. \tag{2.11}$$

The matrix V relates mass and SU(2) eigenstates, and is the unity matrix for leptons, and the CKM matrix for quarks. The QCD correction factor R_{QCD} ($\equiv 1$ for leptons) takes into account the color degrees of freedom and QCD radiative corrections for quarks, and is to first order in α_s given by:

$$R_{QCD} = 3(1 + \frac{\alpha_s(m_W^2)}{\pi}). \tag{2.12}$$

In these equations, fermion masses have been neglected, which is, given the high W mass, an acceptable assumption for most kinematically allowed fermion pairs. Due to the structure of the CKM matrix, non-diagonal decays like $W^+ \to c\bar{b}$ are suppressed.

The dominant hadronic W^+ decays, with almost equal probabilities, are thus $W^+ \to u\bar{d}$ and $W^+ \to c\bar{s}$ [2]. This results in about 45.6% of WW events being of the $q\bar{q}'q\bar{q}'$ type, about 43.6% of the $q\bar{q}'\ell\nu$ type, and some 10.8% of the $\ell\nu\ell\nu$ type.

The total width of the W boson in the Standard Model,

$$\Gamma_W = \Gamma_{e\nu} + \Gamma_{\mu\nu} + \Gamma_{\tau\nu} + \sum_{q,\bar{q}' \neq t,\bar{t}} \Gamma(W \to q\bar{q}') = \frac{3G_F m_W^3}{2\pi\sqrt{2}}\left(1 + \frac{2\alpha_s(m_W^2)}{3\pi}\right), \tag{2.13}$$

equals 2.093 ± 0.003 GeV, using the PDG value for m_W [7], and is proportional to m_W^3.

The branching fraction of the hadronic W decay, $\mathrm{Br}(W \to q\bar{q}')$, is defined as:

$$\mathrm{Br}(W \to q\bar{q}') = \frac{\sum_{q,\bar{q}' \neq t,\bar{t}} \Gamma(W \to q\bar{q}')}{\Gamma_W}. \tag{2.14}$$

It follows that

$$\frac{\mathrm{Br}(W \to q\bar{q}')}{1 - \mathrm{Br}(W \to q\bar{q}')} = \left(1 + \frac{\alpha_s(m_W^2)}{\pi}\right) \sum_{i=u,c;j=d,s,b} |V_{ij}|^2, \tag{2.15}$$

where V is the CKM matrix. Thus a measurement of the hadronic branching fraction of the W is a test of the unitarity of the CKM matrix, excluding the top quark row. Using the measured values of the other matrix elements, the least well known element, $|V_{cs}|$, can be determined.

To describe the W decay in its rest frame, the coordinate system shown in Figure 2.7 is used. The $e^+e^- \to W^+W^-$ scattering plane is defined as the $x - z$ plane, with the z axis along the W^- direction. The $W^\pm$ rest frames are then reached by a Lorentz boost along the z-direction. The polar angle θ^* in the rest frame is defined with respect to that z-axis.

In the W rest frame, each decay (anti)fermion obtains an energy equal to half the W mass, neglecting fermion masses. The distributions of the polar angle θ^* of the decay particles in the W rest frame however are different for fermions and antifermions, as shown in Figure 2.8 (top left) for $W \to q\bar{q}'$ decays. This is a consequence of the polarization of the W and the V-A structure of the W decay.

The distribution of the polar angle of the W^- in the laboratory is shown in Figure 2.5 (right). W^- bosons are produced predominantly in the original e^- direction, and W^+ bosons predominantly in the original e^+ direction. This is a consequence of the interference of the t-channel neutrino exchange diagram with the s-channel diagrams.

After a Lorentz boost in the lab frame, the distributions of quark and antiquark energies and angles are shown in Figure 2.8, for $\sqrt{s} = 189$ GeV.

[2] Of course for the W^- the corresponding decay modes are $W^- \to d\bar{u}$ and $W^- \to s\bar{c}$. In the remainder of this thesis, the used terminology implies both the mentioned decay mode as well as the charge-conjugated one, unless explicitly mentioned otherwise.

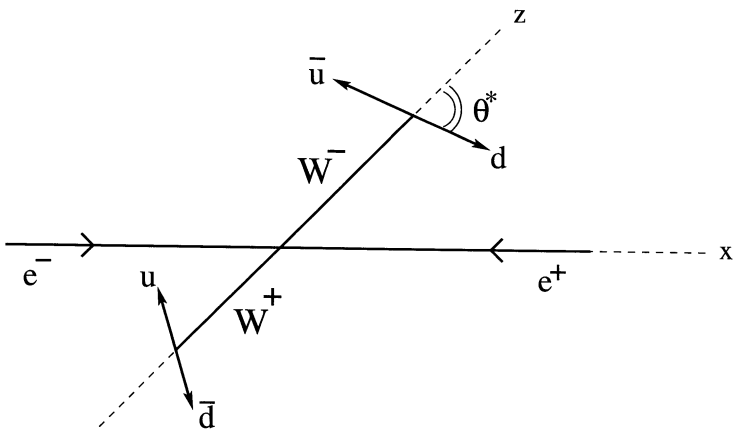

Figure 2.7: *Schematic view of the coordinate system used to describe W decay, for an example* $e^+e^- \to u\bar{d}\bar{u}d$ *event. The W decay products are schematically drawn back-to-back, to illustrate the W rest frame. The x-axis is taken to be the* e^- *direction, and the z-axis the* W^- *direction. The decay angle* θ^* *is calculated with respect to the positive z-axis.*

Experimentally it is virtually impossible to distinguish between jets created by quarks and those created by antiquarks. The distributions of jet energies and angles are therefore a sum of the quark and antiquark distributions.

2.4 Four-Fermion Production

Taking into account W decays, $W \to q\bar{q}'$ and $W \to \ell\nu$, the final state really consists of four fermions. Typically, a four-fermion final state can be obtained through more Feynman diagrams than the double-resonant CC03 diagrams, such as single-resonant and non-resonant graphs. For WW-like four-fermion final states, the number of contributing diagrams ranges from 9 to 56 depending on the final state, with both charged- and neutral current graphs present generally. This is shown in Table 2.3. The CC11 family is shown in **boldface** and consists of final states with non-identical particles, nor electrons or electron neutrinos; there are less than 11 diagrams if neutrinos are produced since these do not couple to photons. The CC20 family consists of final states with one $e^\pm$: the additional diagrams have a t-channel boson exchange; for a purely leptonic final state there are 18 diagrams. The remaining diagrams in *italic* produce two mutually charge-conjugated fermion pairs, and can also be produced via neutral current diagrams.

Figure 2.9 shows all 11 diagrams contributing to $e^+e^- \to u\bar{d}s\bar{c}$. The additional diagrams

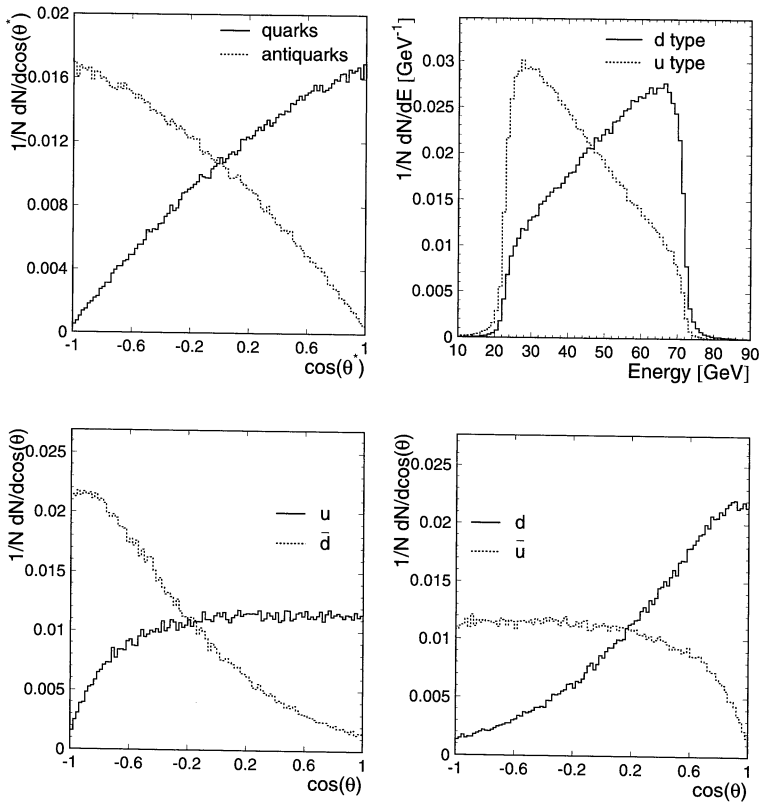

Figure 2.8: *Top left: distribution of the polar angle θ^* (defined in the text) of quarks and antiquarks, produced in* $\mathrm{W} \rightarrow \mathrm{q}\bar{\mathrm{q}}'$ *decays, in the parent W rest frame. Full histogram: quarks; dashed histogram: antiquarks. Top right: distribution of the energy in the laboratory of down-type quarks and antiquarks* ($\mathrm{d}, \bar{\mathrm{d}}, \mathrm{s}, \bar{\mathrm{s}}, \mathrm{b}, \bar{\mathrm{b}}$) *(full histogram), and up-type quarks and antiquarks* ($\mathrm{u}, \bar{\mathrm{u}}, \mathrm{c}, \bar{\mathrm{c}}$) *(dashed histogram) produced in W decays. Bottom left: distribution of the polar angle θ in the laboratory of* u *(and* c*) (full histogram) and* $\bar{\mathrm{d}}$ *(and* $\bar{\mathrm{s}}$ *and* $\bar{\mathrm{b}}$*) (dashed histogram) produced in* W^+ *decays. Bottom right: distribution of the polar angle θ in the laboratory of* d *(and* s *and* b*) (full histogram) and* $\bar{\mathrm{u}}$ *(and* $\bar{\mathrm{c}}$*) (dashed histogram) produced in* W^- *decays. All figures are for* $\sqrt{s} = 189$ GeV.

CC	$u\bar{d}$	$c\bar{s}$	$e^+\nu_e$	$\mu^+\nu_\mu$	$\tau^+\nu_\tau$
$d\bar{u}$	*43*	**11**	20	**10**	**10**
$e^-\bar{\nu}_e$	20	20	*56*	18	18
$\mu^-\bar{\nu}_\mu$	**10**	**10**	18	*19*	**9**

Table 2.3: *Number of lowest-order Feynman diagrams contributing to "CC"-type final states. Combinations not in the table are obtained from family generation symmetry and particle/anti-particle exchange. See text for further explanation.*

contribute to the four-fermion cross section and interfere with the CC03 diagrams. Typically, the single-resonant and non-resonant graphs are suppressed with respect to the CC03 graphs by powers of Γ_W/m_W. Nevertheless, when the CC03 cross section is extracted from the data, neutral current contributions to certain final states will need to be subtracted, and the interferences will need to be investigated and, if necessary, corrected for.

For an accurate calculation of the $e^+e^- \rightarrow W^+W^-$ cross section, radiative corrections are important. Initial state radiation decreases the W^+W^- cross section by $\mathcal{O}(10\%)$ [29], as shown in Figure 2.6. The Coulomb singularity [30, 31] is another QED process especially important at the threshold. It is due to the electromagnetic attraction between slowly moving charged W bosons. The correction amounts to about 5% right at the threshold and smaller values at higher energies. The dominant QED corrections are explicitly taken into account in the analytical programs and the used Monte Carlo event generators. The bulk of other electroweak radiative corrections is incorporated in the calculations by using energy-scale-dependent (running) values of EW parameters. Recently, progress has been made in the calculation of the non-factorizable radiative corrections using the double pole approximation [32, 33, 34]. Further details on the remaining uncertainties due to radiative corrections are given in Section 2.5.1.

Taking all corrections into account, Standard Model calculations predict a total $e^+e^- \rightarrow W^+W^- \rightarrow$ four-fermion cross section of approximately 3 pb at the threshold, rising fast to approximately 16 pb at $\sqrt{s}$ = 189 GeV(see Figure 2.6).

Obviously, the total cross section for $e^+e^- \rightarrow W^+W^-$ depends on the W mass. This dependence is shown in Figure 2.10 for 155 GeV $\leq \sqrt{s} \leq$ 175 GeV; for higher values of $\sqrt{s}$ the dependence is small. Close to threshold, a measurement of the cross section can thus be used to extract m_W; a detailed analysis shows that the optimal $\sqrt{s}$ equals $2m_W + 0.5$ GeV [35].

A precise measurement of the WW cross section is a test of the Standard Model and puts limits on physics beyond the Standard Model. Anomalous contributions to the triple gauge couplings will affect the cross section. In fact, the Standard Model solves the unitarity problems in the Fermi theory at high energies through delicate cancellations that follow from

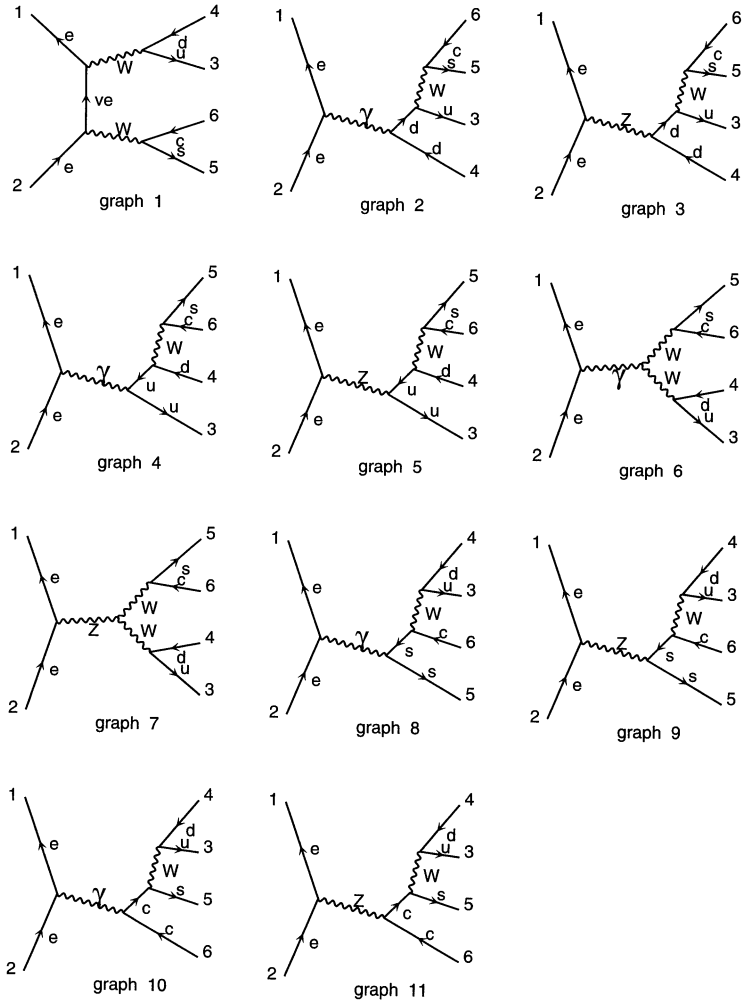

Figure 2.9: *The lowest-order Feynman diagrams for the process* $e^+e^- \rightarrow u\bar{d}s\bar{c}$.

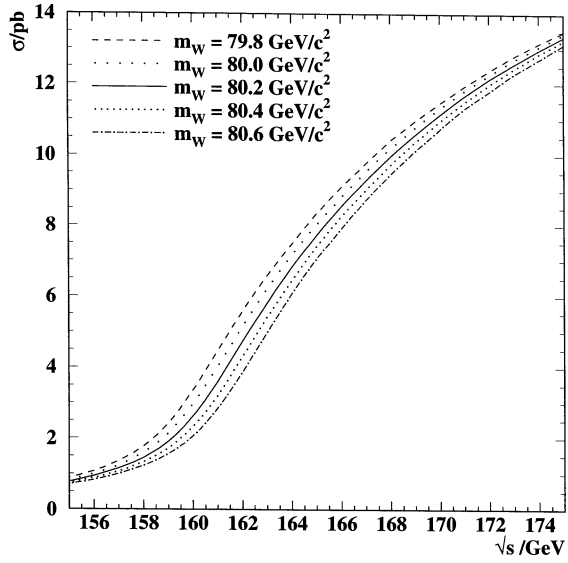

Figure 2.10: *Dependence of the* $e^+e^- \rightarrow W^+W^-$ *cross section on* $\sqrt{s}$ *for various values of* m_W.

the gauge boson self-couplings. Deviations from these couplings will generally increase the WW cross section.

Certain theories predict deviations from the Standard Model in $e^+e^- \rightarrow W^+W^-$ already at the tree level. For example, adding more gauge groups to the Standard Model leads to additional neutral intermediate vector bosons, $e^+e^- \rightarrow Z' \rightarrow W^+W^-$ diagrams, and large effects on the W^+W^- total and differential cross sections [36].

Another extension of the Standard Model postulates existence of a few additional compact time-space dimensions and an electroweak-gravitation "unification scale" M_S of the order of a few hundred GeV [15]. These extra dimensions, depending on their size, affect Newton's law at very small (sub-millimeter) distances. They also lead to non-negligible graviton exchange between Standard Model particles. The $e^+e^- \rightarrow W^+W^-$ cross section can be shifted by up to several percent due to additional graviton diagrams [16].

2.5 Theoretical Uncertainties

The experimental analysis of the WW production cross section and the W mass at LEP is affected by a number of theoretical uncertainties that will enter the results as systematic

errors. In this section, the most important of these uncertainties will be discussed: radiative corrections and fragmentation and hadronization. Some aspects of the fragmentation are specific to $W^+W^- \rightarrow q\bar{q}q\bar{q}$ events only, due to the presence of two hadronically decaying W bosons. There are intrinsic uncertainties in the modeling of these aspects, which can only be studied with Z data in a very limited way. Bose-Einstein correlations and color reconnection are the two most significant of these effects.

2.5.1 Radiative Corrections

WW production at LEP is affected by the radiation of one or more photons from the initial state (the electron or positron) or the final state (the 4 fermions produced in W decay), and the interference between the two, as well as by the exchange of virtual photons in many ways, such as between the W's (Coulomb corrections). These photonic corrections are, in principle, all calculable in QED, although in practice this is not always easy. Radiation of weak bosons is negligible.

Final state radiation (FSR) is preferentially emitted along the direction of the quark or the lepton, and is typically contained in the jet or combined with the reconstructed lepton. Calculations of FSR do not have large uncertainties.

The Coulomb correction can to first approximation be included as a correction to the Born cross section, inversely proportional to the relative velocity of the W bosons. This correction is thus largest close to threshold, $\sqrt{s} \approx 2m_W$.

Initial state radiation (ISR) can be emitted from the electron or positron, and can take away a significant amount of energy from the interaction, effectively reducing $\sqrt{s}$. In first approximation, the effects of ISR factorize as the product of a radiator function (which effectively gives the probability for an electron of certain energy to radiate a photon with certain energy) and a cross section at reduced $\sqrt{s}$. Various methods exist to implement this in Monte Carlo programs: YFS exponentiation [37], the structure function approach [38], or the QED parton shower approach [39].

However, the current precision of the measurements of WW production at LEP exceeds the precision of the factorization approach, and one has to worry about non-factorizable corrections. Such non-factorizable corrections include for example radiation between charged fermions originating from different W's. In principle, the full electroweak corrections to at least $\mathcal{O}(\alpha)$ are desired, but these have not yet been calculated for off-shell WW production. Instead, the Monte Carlo programs RacoonWW [33] and YFSWW3 [34] implement these corrections in the double pole approximation (DPA); they lower the previously calculated cross sections by some 2-2.5%. It is estimated that an uncertainty on the WW cross section of 0.5%, and on the W mass of $\mathcal{O}(10)$ MeV remains [40].

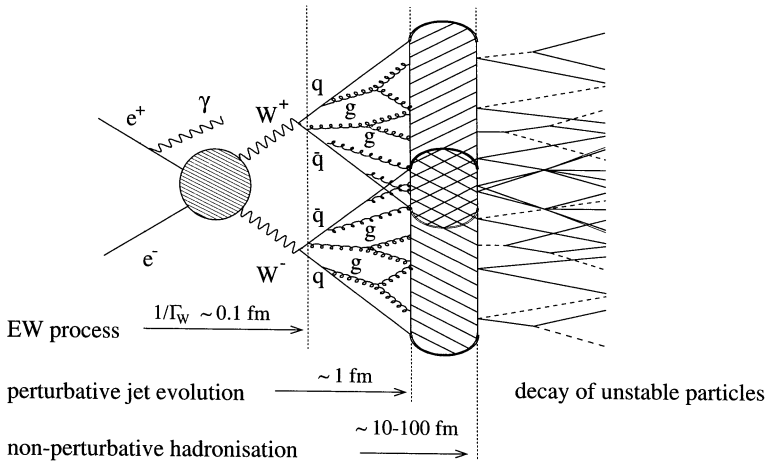

Figure 2.11: *Schematic illustration of the process of fragmentation and hadronization, see text.*

2.5.2 Fragmentation and Hadronization

In QCD, quarks cannot exist as free particles, and experimentally free quarks indeed have never been observed. Instead, the final state of any process involving the production of quarks and antiquarks consists of a collection of stable and unstable hadrons; the unstable hadrons in turn decay into stable hadrons, leptons and/or photons. The transformation of the original quarks and antiquarks into hadrons takes place initially through a series of strong interaction processes such as the radiation of gluons off quarks and gluon splitting into quark-antiquark pairs or gluon pairs. Generally, the quarks and gluons created and participating in these processes are called partons. Each parton is characterized by some virtuality scale Q^2; this virtuality scale is highest at the beginning of the fragmentation process, and decreases towards the end of it, as more and more partons are created. Finally, the produced partons combine into the final state hadrons. A schematic illustration of this process is shown in Figure 2.11.

Gluons are radiated off their mother quarks preferentially in the mother's flight direction. Together with the Lorentz boost of the quark-gluon system into the laboratory frame, this leads to the observation that the final state hadrons, produced in the fragmentation and hadronization process, will mostly follow directions close to that of the original quark. They are collimated in a cone of finite size, a so-called jet.

The radiation of a gluon off a quark, or the splitting of gluons, is characterized by the QCD coupling strength α_s. This coupling strength is a strong function of the virtuality scale

Q^2 of the process, and QCD dictates that α_s is small voor high Q^2, in the initial phase of the fragmentation, but large for small Q^2 in the final phase. When α_s is small, the parton radiation process can be described by perturbative methods by perturbative QCD, which is relatively well understood. For large α_s, however, perturbative methods fail, and the final phase of the fragmentation is referred to as the non-perturbative phase. The perturbative phase of the fragmentation of quarks from W decay takes place on a distance scale of $\mathcal{O}(1)$ fm; the non-perturbative phase however can take tens or hundreds of fm.

The original quark-antiquark pair is a color singlet, as are the individual hadrons in the final state. The individual partons, however, carry color charges, and as more and more partons are radiated the color flow becomes very complicated. The process of the creation of the final state hadrons from this collection of colored partons is not well understood.

The difference between the perturbative and non-perturbative phases in the fragmentation process is reflected in the simulation of fragmentation by Monte Carlo programs. These programs typically simulate the perturbative phase by parton showers (PS), which contain the leading logarithms of all orders of the parton splitting processes. The showers are allowed to propagate until the virtually scale Q^2 reaches a cut-off value Q_0^2; typically Q_0 is of order $1-2$ GeV. Exact matrix elements (ME) for the parton splitting processes exist up to second order in α_s, but not at higher orders, and are therefore not sufficient to describe the full fragmentation process. Simultaneous use of the matrix elements, for the lowest order(s), and parton showers, for higher orders of the parton splitting processes, is difficult: one must avoid double counting. The matching of ME and PS has been achieved for the first order ME, but not yet for higher orders.

The Monte Carlo programs used in this thesis, JETSET [41], HERWIG [42] and ARIADNE [43], all contain a first order ME plus PS approach. ARIADNE hereby uses the color dipole model in its parton shower.

Below Q_0, perturbative models fail, and one is forced to fall back to a number of phenomenological models.

A first approach is independent fragmentation: the assumption that partons fragment in isolation from each other [44]. However, this model fails to describe experimental data [45].

The JETSET program is intimately connected to the Lund string model. As the initial quark and antiquark move apart, they are connected by a color flux tube that stretches between them. JETSET models this flux tube as a string, with a certain intrinsic string tension. As the quark and antiquark move apart, the potential energy in the string increases, and the string may break into two pieces by the production of a new $q\bar{q}$ pair. Gluons radiated off quarks form kinks on the string. Hadrons are formed by combining quark antiquark pairs from two adjacent string breakings. A large number of free parameters exist in this model, the most important ones are related to the transverse and longitudinal momentum of quarks and antiquarks produced in the string breakings. Also ARIADNE uses JETSET for the non-perturbative phase of the fragmentation.

HERWIG uses a different approach. Gluons remaining after the parton shower are made

to decay into $q\bar{q}$ pairs. Together with the quarks present in the shower, they form colorless clusters of various masses. Heavy clusters decay again into lighter clusters, lighter clusters decay directly into hadrons. The most important free parameters of HERWIG are related to the maximum allowed cluster mass, and the details of cluster decay.

Finally, hadrons result from the fragmentation and hadronization process. Some of these are unstable; the Monte Carlo programs decay them according to internally stored tables of branching fractions.

It is important to realize that the free parameters of JETSET and HERWIG have little or no physical meaning outside the context of the model in which they live. The parameters must be tuned to describe the data. Although ARIADNE uses JETSET for the non-perturbative phase, the fact that it differs in the parton shower phase and the fact that one cannot make a strict distinction between the two phases implies that the JETSET parameters must be retuned when ARIADNE is used. The parameter tuning is performed with $Z \rightarrow q\bar{q}(g)$ events taken from the LEP1 data [46]. For all three programs, values for the parameters can be found that describe the data to satisfaction, although the overall description of HERWIG is poorer than JETSET and ARIADNE [46]. Nevertheless, within each model an uncertainty on its predictions remains due to the statistical and systematic uncertainties on the free parameters. In addition, uncertainties in fragmentation remain due to differences between the various models.

The cross section for radiation of a gluon off a quark is largest for radiation in the direction of the quark (collinear radiation), and for low gluon energies. It follows that most gluons are radiated in a direction close to the parent quark, and are in fact located in its observed jet. However, occasionally a high energy gluon will be emitted away from the quark and form a separate jet.

The major background for the $W^+W^- \rightarrow q\bar{q}q\bar{q}$ signal consists of QCD 4-jet events, $e^+e^- \rightarrow Z(\gamma) \rightarrow q\bar{q}gg(\gamma)$, where two hard gluons are radiated in the final state and form independent jets. From the discussion in the previous paragraph it follows that gluon jets are typically softer than quark jets, and are typically closer to an other jet. This provides a handle to their identification and rejection, as will be explained in chapter 5. Nevertheless, a fraction of the background will pass the cuts and end up in the final sample; in order to calculate the WW cross section the number of such events in the final sample must be estimated and subtracted. Although the exact $\mathcal{O}(\alpha_s^2)$ matrix elements for the $q\bar{q}gg$ process are known, they have not yet been implemented in parton shower based Monte Carlo programs, such as PYTHIA [41], for reasons described above. Instead, PYTHIA uses the exact first order ME plus the parton shower, which does not give a perfect description of the 4-jet structure of the events [46]. In the analysis of the WW cross section, a correction is made for this effect; the uncertainty of the correction will enter as a systematic error.

2.5.3 Bose-Einstein Correlations

Bose-Einstein correlations are the effect of the quantum-mechanical requirement of symmetry of multi-boson production amplitudes. They manifest themselves for example as an enhancement in the two-particle correlation function for identical bosons at small distances [47]. The currently available probabilistic Monte Carlo models of parton showering and string fragmentation do not actually calculate the multi-boson production amplitudes, and are therefore not able to implement Bose-Einstein correlations through symmetrization of these amplitudes. Instead, a number of ad-hoc algorithms are used to reproduce in the Monte Carlo the two-particle correlation function observed in the data.

For the study of the effects of Bose-Einstein correlations on the analysis presented in this thesis the LUBOEI routine as implemented in PYTHIA 6.1 is used [48]. In this routine, particles in the final state are reshuffled such as to reproduce phenomenologically the two-particle correlation function for like-sign particles. In order to subsequently restore energy-momentum conservation, a reshuffling involving all particles, including the unlike-sign particles, is performed. In LUBOEI there exist various options to do this [48]. In the studies reported here, the variants labeled BE_0 and BE_{32} are used[3].

Bose-Einstein correlations between two or more identical bosons coming from the decay of two different W bosons introduce an interconnection, or cross-talk, between the two hadronic systems. This may affect the invariant mass of each of these systems, and therefore the W mass measurement. In LUBOEI this can be studied through the options of including correlations between all pions, including only correlations between pions from the same W, or including no correlations at all. In addition, we will make use of results of a dedicated analysis into the existence of these correlations [49, 50].

Other algorithms have been suggested as an alternative to LUBOEI in order to implement Bose-Einstein correlations [51, 52, 53, 54]. However, all of these currently have a number of problems that inhibit their use. These models, however, all predict only small effects on W mass and cross section measurements.

2.5.4 Color Reconnection

The two W bosons in an $e^+e^- \rightarrow W^+W^-$ event decay typically at distances of $\mathcal{O}(0.1)$ fm of each other, much smaller than the typical hadronization scale of $\mathcal{O}(1)$ fm. Thus, the development of the QCD parton shower, the fragmentation of the $q\bar{q}(g)$ system and the formation of hadrons take place for the decay products of both W's in the same spacetime region. It is natural to assume that in this process color charges originating from one W boson feel the presence of color charges from the other W boson, and interact with them, leading to cross-talk between the two W's [55]. These effects are suppressed in the hard perturbative phase: hard gluons are emitted incoherently by the two original color singlets.

[3] For some studies, also variant BE_3 was used, with results similar to BE_{32}.

Calculations have shown that color exchange in the perturbative phase lead to only small effects [56]. Soft gluons, $E_g < \Gamma_W$, however, feel the collective action of both systems and can lead to non-negligible effects in the non-perturbative phase of the hadronization process.

These effects are difficult to incorporate in the currently available fragmentation models. In the string model, the fragmentation of a $W^+W^- \rightarrow q_1\overline{q_2}'q_3\overline{q_4}'$ event proceeds through stretching and decay of two strings, each binding a color singlet $q_1\overline{q_2}'$ (c.q. $q_3\overline{q_4}'$), with quark and antiquark as endpoints of the string, connected through hard gluons radiated in a parton shower or by a QCD dipole radiation model. In this model, the strings develop independently of each other. Alternative configurations, interconnecting the two strings, are not predicted and have to be put in explicitly by hand, i.e. by making use of other models [56, 57, 58, 59].

The models implemented in PYTHIA are SK I, SK II and SK II' [56, 57]. In the SK I model, the string has a finite transverse size. In a $W^+W^- \rightarrow q\overline{q}q\overline{q}$ event, the overlap O of the two strings is calculated, and the probability of reconnection of the two strings is based on this overlap:

$$P_{CR} = 1 - \exp(-\kappa \cdot O). \tag{2.16}$$

The model has one free parameter κ. In the SK II and SK II' models, the string is a vortex line without transverse dimensions, and reconnections only take place when two strings intersect. In the SK II' model, reconnection only takes place if this reduces the overall string length. These models have no free parameters.

The models implemented in ARIADNE are based on the reconfiguration of radiating QCD color dipoles [58, 59]. Reconnection only takes place if this is energetically favorable, i.e. leads to strings with lower mass. The AR1 model allows only reconnections within a single string (i.e. a single W), and in principle does not lead to any effects on the W mass. In the AR2 model, reconnection between different W's is confined to low energy gluons ($E < \Gamma_W$) only, since only these feel both W's. In the AR3 model, reconnection is allowed for all gluons; this should be considered as too extreme from a theoretical point of view.

Also HERWIG allows for color reconnections [42], by reconfiguration of the partons from the parton shower before cluster formation.

For assessment of the systematic error to be assigned to the W mass measurement we will again make use of dedicated studies of color reconnection [60].

Chapter 3

Tools

3.1 LEP

The Large Electron Positron (LEP) collider has been built to study the carriers of the electroweak force, the Z and $W^{\pm}$ bosons. For this purpose electrons are collided on positrons with energies sufficient to produce these particles. The collisions take place at four interaction points, where the LEP detectors ALEPH [61], DELPHI [62], L3 [63] and OPAL [64] are located.

In the first phase of the LEP program, a center-of-mass energy sufficient to produce a Z-boson at rest was used. The first physics data at this energy have been taken in 1989, while this phase has been finished in 1995. In the second phase, the LEP collider has been upgraded, so that the leptons can be accelerated to energies exceeding 100 GeV. In this phase the center-of-mass energy is such that the threshold for W^+W^- production is exceeded, i.e. two W bosons can be produced. The integrated luminosity at different center-of-mass energies collected by the L3 detector in the years 1990–1998 is summarized in Table 3.1.

The LEP collider consists of an accelerator ring with a circumference of about 26.7 km, and is situated between 50 and 150 meters underground on the French-Swiss border near Geneva. A schematic view is shown in Figure 3.1. The electron and positron beams are provided by the LEP injector chain [65] using the previously existing Proton Synchrotron (PS) and Super Proton Synchrotron (SPS), see Figure 3.2. Positrons are created in a tungsten converter target by a 200 MeV electron beam from a high-intensity linear accelerator (LINAC). A second LINAC accelerates the electrons and positrons up to 600 MeV, to be accumulated in the Electron–Positron Accumulation Ring (EPA). The PS and SPS are subsequently used to accelerate the beams up to 3.5 GeV and 20 GeV respectively, after which they can be injected to LEP. Once in the LEP collider the leptons are accelerated to the desired energy by radiofrequency cavities. In the first phase of LEP copper cavities were used, for the second phase of LEP, dedicated to W-pair production, superconducting cavities were installed to achieve the required increase of center-of-mass energy. More details about the

Year	$\sqrt{s}$ (GeV)	$\mathcal{L}$ (pb^{-1})	Year	$\sqrt{s}$ (GeV)	$\mathcal{L}$ (pb^{-1})
1990	91.3	5.8	1995	130.3	2.8
1991	91.2	13.3	1995	136.3	2.3
1992	91.3	22.7	1996	161.3	10.3
1993	91.3	33.0	1996	172.1	10.3
1994	91.2	49.7	1997	182.7	55.3
1995	91.3	30.1	1998	188.6	174.4

Table 3.1: *The integrated luminosity $\mathcal{L}$ at different center-of-mass energies collected by the L3 detector during 1991–1998. For years where data was collected at several slightly different energies the average energy is given.*

LEP accelerator and its energy upgrade can be found in References [66, 67].

3.1.1 LEP Beam Energy Determination

For the analysis of the W mass, as described in this thesis, a precise knowledge of the LEP beam energies is important. The LEP Energy Working Group has constructed a LEP Beam Energy Model that calculates the center-of-mass energies $\sqrt{s}$ in each of the 4 interaction points as a function of time, taking into account all RF and magnet configurations, as well as additional effects that influence the beam energy, such as tides, the water level in Lake Geneva, and parasitic currents due to electric trains. The LEP Beam Energy Model provides $\sqrt{s}$ in each of the 4 interaction points separately, since the beam energy is very much influenced by the different layout of RF accelerating voltage in the straight sections.

At LEP1, the LEP beam energy was accurately calibrated using the technique of resonant depolarization. In $\mathrm{e^+e^-}$ synchrotrons, the beams obtain a natural transverse polarization due to the emission of synchrotron radiation. The polarization is destroyed by the application of a small RF field if the applied RF frequency matches the electron spin precession frequency, which is proportional to the beam energy. Since this frequency can be accurately measured, the beam energy is known to a precision of $\mathcal{O}(1)$ MeV.

Unfortunately, above beam energies of about 60 GeV, transverse polarization of the beams no longer builds up due to the presence of depolarizing resonances and the increased beam energy spread. Thus, the technique of resonant depolarization can no longer be applied. The LEP beam energy is proportional to the strength of the magnetic field in the dipoles, and a measurement of the dipole fields thus provides a handle on the beam energy. This is done in two ways: with sixteen Nuclear Magnetic Resonance (NMR) probes in the arcs of LEP, and with a flux loop system that sees 96.5% of the dipole field. The NMR probes are calibrated using resonant depolarization at beam energies between 40 and 60 GeV, and extrapolation

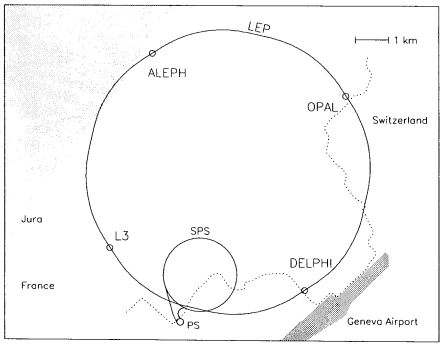

Figure 3.1: *Top view of the LEP collider and storage ring. The locations of the four LEP experiments are indicated.*

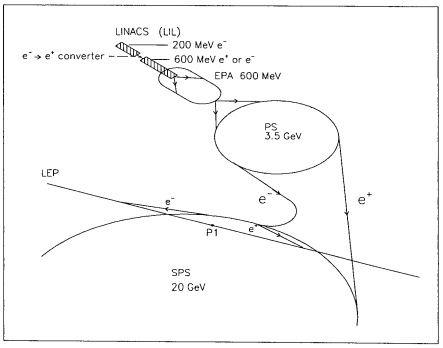

Figure 3.2: *Pre-accelerator chain for the electron and positron beams.*

into the high energy regime then provides the beam energy calibration at LEP2 energies. The accuracy achieved is 25 MeV at $\sqrt{s} = 183$ GeV, and 20 MeV at $\sqrt{s} = 189$ GeV; the better accuracy achieved at 189 GeV is due to the fact that more data was taken in a longer running period. The uncertainty is dominated by observed differences between the NMR's and the flux loop system, by fluctuations in the NMR's, by uncertainties in the field not measured by the flux loop, and by the RF model.

A number of alternative methods to calibrate the beam energies are under investigation, but have not yet yielded conclusive results. The LEP spectrometer project consists of the replacement in 1998 of a standard dipole by a steel dipole with accurately calibrated magnetic field plus two arms of high precision beam position monitors. The bending of the beams in the dipole is measured, which is inversely proportional to the beam energy. In order to reach 10 MeV precision on the beam energy, the beam positions must be measured to accuracies of $\mathcal{O}(1)$ μm. It is not yet clear whether this can be achieved. Another approach consists of the measurement of the energy loss by the beams through the measurement of the synchrotron tune. An accuracy of 15 MeV may be achieved. Finally, experimental measurements of radiative return events, $e^+e^- \to Z\gamma \to f\bar{f}\gamma$, can be used to measure the beam energy; it is still uncertain what precision can be achieved.

3.2 The L3 Detector

The L3 detector is designed to study high energy e^+e^- collisions up to center-of-mass energies of about 200 GeV, with emphasis on high resolution energy measurement of electrons and photons, as well as on high resolution muon spectroscopy. An extensive description of

the detector can be found in Reference [63], while shorter descriptions can for example be found in [68, 69].

An impression of the total detector is shown in Figure 3.3. The central part is shown in more detail in Figure 3.4. The L3 subdetectors are arranged in layers of increasing size surrounding the interaction point and are supported by a 32 m long and 4.5 m diameter steel tube. Starting from the interaction point radially outwards, the main detector components are:

- a Silicon Microvertex Detector (SMD), a central tracking detector (a Time Expansion Chamber, TEC), Forward Tracking Chambers (FTC), and z-chambers. This system measures the direction and momenta of charged particles;
- an electromagnetic calorimeter (ECAL), mainly measuring the energies and directions of electrons and photons;
- scintillation counters, providing timing information;
- a hadron calorimeter (HCAL), measuring the energies and directions of hadrons;
- muon chambers (MUCH), measuring the directions and momenta of muons.
- another layer of scintillation counters, exclusively used to study cosmic ray muons [70].

In addition, luminosity monitors are installed close to the beam pipe at a distance of 2.8 meters from the interaction point. These consist of BGO crystals (the LUMI) with a silicon strip detector in front (the SLUM).

The entire detector is surrounded by a solenoidal magnet (inside radius of the coil 5.9 m, length 11.9 m), providing a magnetic field of 0.5 T along the beam axis. Additional coils, installed on the magnet doors for LEP2 data taking, provide a 1.2 T toroidal field for muon momentum measurements in the endcaps. In the following sections the subdetectors are described in greater detail. The beam axis is chosen as the z-axis.

L3 Tracking System

The aim of the L3 tracking system is to reconstruct charged particle trajectories in the central region of L3, to measure particle charge and momentum, and to reconstruct secondary vertices from decays in flight. It includes a Silicon Microvertex Detector (SMD), a Time Expansion Chamber (TEC), z-chambers and Forward Tracking Chambers (FTC). A view of this part of the detector in the plane perpendicular to the beam axis is shown in Figure 3.5.

The SMD [71] consists of two layers of double-sided silicon ladders 35.5 cm long, situated at radial distances of 6 cm and 8 cm from the z-axis and covering the polar angles $22° - 158°$. The outer silicon surface of each ladder is read out with a 50 μm pitch for the

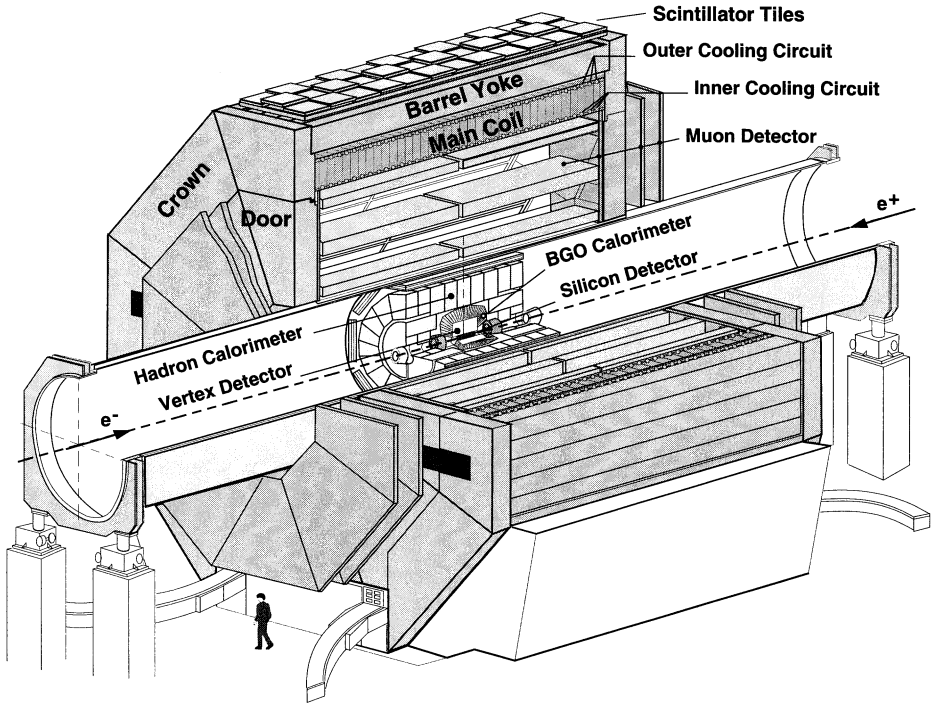

Figure 3.3: *Perspective view of the L3 detector at LEP. A man is drawn near the magnet to give an idea of the scale. The inner detector is shown in more detail in Figure 3.4.*

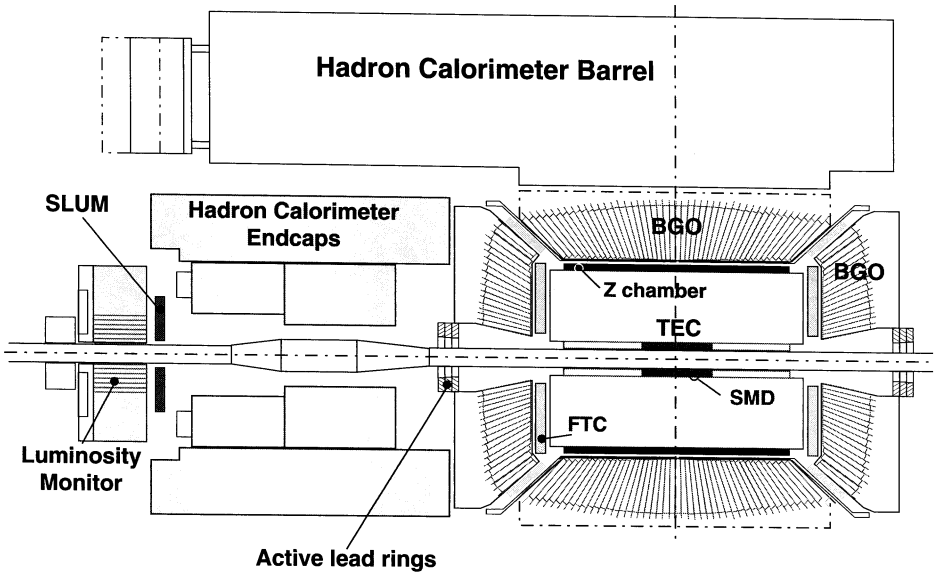

Figure 3.4: *View of the inner part of the L3 detector, shown in the yz plane.*

$r\phi$ coordinate measurements; the inner surface is read out with a 150 μm pitch (central region) or 200 μm pitch (forward regions) for the z coordinate measurements. The single track resolution of the SMD is 6 μm in the $r\phi$ direction and 20–25 μm in the z direction.

The TEC [72] is a drift chamber with an inner radius of 8.5 cm, an outer radius of 47 cm, and a length of 98 cm. Radial cathode wire planes divide the TEC into 12 inner and 24 outer sectors. The sectors are subdivided radially by a plane of mixed anode sense wires and additional cathode wires. Planes of closely spaced grid wires on either side of each anode plane provide a homogeneous low electric field in most of the sector (drift region), and a small high-field region near the anode plane (amplification region). Secondary particles, produced by ionization along a charged track, drift slowly in the low field region towards the high field region, where they produce further ionization particles in an avalanche that amplifies the original signal. The timing of the signal, measured at each anode, determines the distance to the track along a line perpendicular to the anode plane with an average resolution of about 50 μm.

The z coordinate of a track is measured by two layers of proportional chambers surrounding the cylindrical outer surface of TEC and covering the polar angles $45° < \theta < 135°$.

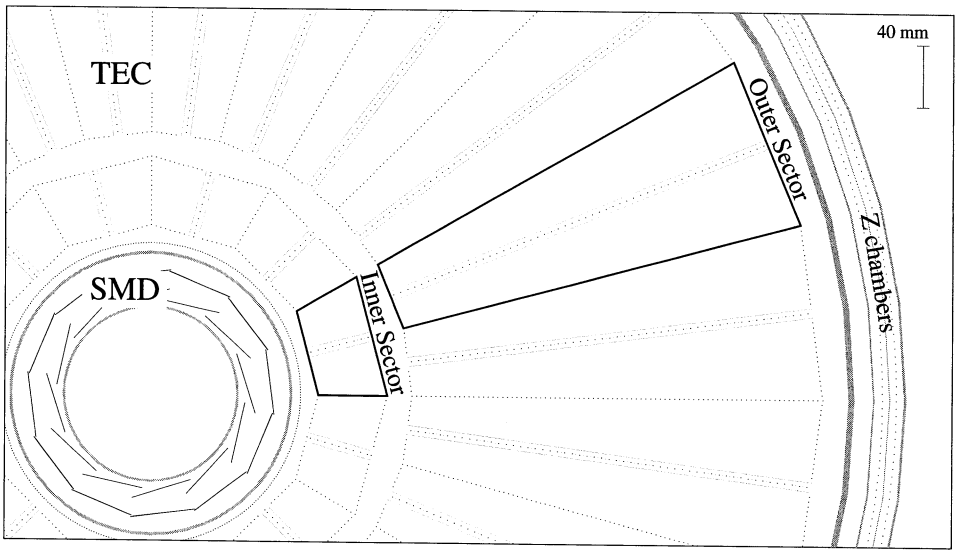

Figure 3.5: *View of the innermost part of the L3 detector in the plane perpendicular to the beam axis. Going outwards from the interaction point, the Silicon Microvertex Detector (SMD), Time Expansion Chamber (TEC) and the z-chambers are drawn, respectively.*

Another two layers of proportional chambers with strips at an angle 70.1° with respect to the beam axis provide additional stereo information. The z-chambers provide a single track resolution of approximately 300 μm.

In Fig 3.6(a) an event is shown with four tracks in the TEC.

Electromagnetic Calorimeter

The electromagnetic calorimeter uses about 11000 bismuth germanium oxide ($Bi_4Ge_3O_{12}$, usually abbreviated as BGO) crystals as the showering medium for electrons and photons. Since BGO is a scintillator, part of the energy of the incoming particles is converted to light. The small radiation length of this material allows the construction of a compact calorimeter. Electrons and photons traversing the BGO calorimeter interact electromagnetically, producing secondary electrons and photons that also interact in a chain reaction leading to an electromagnetic shower. When the energy of an electron in a shower falls below 10 MeV, it loses its remaining energy primarily by ionization, creating excitations in the crystal lattice. The excitations decay producing photons, so that the total amount of scintillation light produced by the shower is proportional to the energy deposited. The light yield is measured using two photodiodes, glued to the rear of each crystal. Electrons and photons produce

practically indistinguishable electromagnetic showers, leaving most of their energy in the calorimeter. Hadrons in the BGO can lose energy through nuclear interactions, which then result in diffuse deposits with large fluctuations. Usually hadrons are not stopped by the BGO, and deposit most energy in the hadronic calorimeter, located behind the electromagnetic calorimeter. Muons do not interact strongly in the BGO and produce small signals that are almost independent of their energy (Minimum Ionizing Particles, or MIPs).

The BGO barrel calorimeter consists of two symmetrical half barrels which contain in total 7680 crystals and surround the central tracking system, covering a polar angle range of $42° < \theta < 138°$. Two BGO endcap calorimeters (1527 crystals each) cover a polar angle of $10° < \theta < 37°$ and $143° < \theta < 170°$, as can be seen in Figures 3.4. The barrel crystals are 24 cm long truncated pyramids about 2×2 cm^2 at the inner and 3×3 cm^2 at the outer end. In the theta direction the crystals are aligned with their long axis pointing to the interaction point. In the phi direction the crystals are tilted by about $0.6°$ to minimize the chance that a particle escapes undetected through the inactive material between the crystals.

For electrons and photons of more than 5 GeV the energy resolution is better than 2% with an angular resolution better than 2 mrad. A more detailed description of the electromagnetic calorimeter can be found in Reference [69].

In 1996 the gap between the barrel and endcap parts of the calorimeter was filled with blocks of lead threaded with plastic scintillating fibres. This so called SPACAL detector improves the hermeticity of the L3 detector.

An example of an electromagnetic energy deposit is shown in Fig 3.6(b). A considerable amount of energy is not matched to a track, which indicates the presence of one or more photons, for example from π^0 decay.

Scintillation Counters

The purpose of the plastic scintillation counters, located between the electromagnetic and hadronic calorimeters, is to provide time-of-flight information to reject background from muons originating from cosmic rays. One of these passing near the interaction point can fake a muon pair event produced in e^+e^- collisions. In this case the time difference between opposite scintillation counter hits is about 6 ns, while for signal events the time difference is zero. The timing information provided by the scintillators is accurate enough to distinguish between cosmic ray muons and muons produced in e^+e^- interactions. In addition, the scintillator counters are used in the trigger.

Hadron Calorimeter

The hadron calorimeter surrounds the ECAL and is designed to measure the energy of hadrons, typically depositing only a fraction of their energy in the ECAL. Hadrons traversing the HCAL loose their energy through nuclear interactions in layers of depleted uranium initiating showers of low energy particles that are detected in proportional wire chambers

interspersed with the absorber. The wires in successive layers of the wire chambers in the barrel area are rotated by 90° thus providing the coordinate measurements in both, ϕ and z directions. In the endcaps, wires in successive chambers are rotated each by 22.5°.

The HCAL barrel is divided into 16 modules in ϕ and 9 modules in z, with an angular coverage between $35° < \theta < 145°$. The HCAL endcaps consist of three rings: an outer ring and two inner rings, covering the polar angle regions $5.5° < \theta < 35°$ and $145° < \theta < 174.5°$.

The hadron calorimeter acts as a filter as well as a calorimeter, allowing only non-showering particles to reach the precision muon detector. The thickness of the HCAL together with the electromagnetic calorimeter and support structures is about 6 nuclear interaction lengths in the barrel part and 6–7 nuclear interaction lengths in the endcaps.

A muon filter surrounds the barrel HCAL, and is mounted on the inside wall of the support tube. It consists of eight octants of brass absorber plates (thickness about 1 nuclear absorption length), interleaved with five layers of proportional chambers. The aim of the muon filter is to ensure that only muons and neutrinos pass through to the muon chambers.

In Fig 3.6(c), a significant amount of hadronic energy deposit is shown on one side, whereas the energy deposited in the top of the calorimeter is consistent with a minimum ionizing particle.

Muon Chambers

The barrel muon chambers consist of octants, each containing three layers of drift chambers: MI (inner), MM (middle) and MO (outer). Each layer consists of "P"-chambers, measuring the $r\phi$ coordinates; in addition the MI and MO layers contain "Z"-chambers, measuring the z coordinate. The barrel muon chambers cover the angular range $43° < \theta < 137°$.

To improve hermeticity, forward-backward muon chambers have been installed before LEP2. These consist of three additional layers of drift chambers mounted on the magnet doors in either side of the interaction point, extending the angular coverage down to 22° from the beam pipe.

The barrel muon chambers provide a momentum resolution for muons of 3%, at 45 GeV. The momentum resolution of the endcaps is between 3% and 30%, at low polar angles the resolution becomes worse, mostly due to multiple scattering in the magnet doors.

In Fig 3.6(d), a muon is shown in the barrel muon system, measured in three layers of drift chambers.

L3 Luminosity Measurement

The luminosity measurement at L3 is based on small-angle Bhabha scattering, $e^+e^- \rightarrow e^+e^-$. The accepted cross section σ_{accepted} for this process is high and can, using only QED, be calculated with high precision. This means that the measured number of Bhabha events N_{bhabha} can be converted to a measurement of the luminosity $\mathcal{L}$ using the relation $N_{\text{bhabha}} = \sigma_{\text{accepted}}\mathcal{L}$.

As the Bhabha cross section peaks at low polar angles the original luminosity detector of L3 consisted of a BGO calorimeter (LUMI) at both sides of the interaction point with polar angle coverage 31–62 mrad, see Figure 3.4. Before the 1993 run this setup was upgraded with a silicon tracker (SLUM) in front of LUMI, providing better position measurement for electrons and positrons entering the calorimeter, and thus allowing a more accurate measurement of the experimental acceptance. Using these detectors the luminosity can typically be measured with a precision of the order of 0.1%.

Trigger and Data Acquisition

The aim of the trigger system is to decide after each beam crossing, whether an e^+e^- interaction took place, in which case the detector signals are read out, digitized and written to tape (the event is triggered).

Triggering is done in three levels of increasing complexity. The level 1 trigger uses signals from subdetectors and either initiates digitization, or clears the front end electronics in time for the next beam crossing. After a positive decision the detector data are stored within 500 μs in multi-event buffers. As during that time all further data taking is stopped, it is important to keep the frequency of positive level 1 decisions low. The level 2 trigger combines the fast digitized trigger data from all subdetectors, whereas level 3 trigger uses already fully digitized signals from all subdetectors to make a final decision. The level 1 trigger rate varies between 5–20 Hz, the final event rate written to tape is about 1–5 Hz. At these rates, the detector dead time introduced by the readout of accepted events is kept to 3% or smaller. Various subtriggers that can lead to a positive level 1 decision are listed below.

- The energy trigger checks the total calorimetric energy, the energy in the ECAL alone, the ECAL and HCAL energies in the barrel part only, or searches for localized clusters of large energy deposits. If any of these quantities exceeds a preset threshold, the event is accepted.

- The TEC trigger uses 14 sense wires from outer TEC chambers to search for tracks. Events are triggered, if at least two tracks are found with transverse momentum exceeding 150 MeV and acolinearity less than 60°.

- The scintillator trigger selects high multiplicity events, where at least 5 out of 30 scintillation counters are hit within 30 ns of the beam crossing time and the hits are spread by more than 90° in azimuth.

- The luminosity trigger selects events with two back-to-back energy deposits of at least 15 GeV in LUMI calorimeters; at least 25 GeV in one of the calorimeters together with at least 5 GeV in the other calorimeter; or at least 30 GeV in one of the calorimeters (this last "single tag" trigger is prescaled by a factor 40).

- The muon trigger selects events with at least one particle penetrating the muon chambers.

Any of these five triggers suffices for level 1 selection. Almost all W^+W^- events are triggered by more than one of the above criteria.

The level 2 trigger aims to reject background events selected by the level 1 trigger. Events with more than one first level subtrigger are automatically accepted, whereas part of the remaining events will be rejected on the basis of more detailed calorimetric and track analyses, and the matching (or lack thereof) between tracks, calorimeters and scintillators.

The level 3 trigger uses the complete data available for the event. The event energies are recalculated and more stringent criteria are applied for track quality and scintillator timings. As for the level 2 trigger, events triggered by more than one level 1 subtrigger are accepted automatically.

3.3 Monte Carlo Simulation

For most processes that are being studied, many particles are produced in the e^+e^- collision. This holds especially if quarks are involved in the production process. The particles subsequently interact in the detector materials. It is important to understand these complex processes, for instance to determine the fraction of the events of a certain process that will pass all detection criteria. The most convenient way to do this is to produce and study a set of simulated events. For the production of simulated events, the first step is to generate particles with distributions as predicted by the theory. The programs used for that are called event generators. Next, the detector response is modeled by the detector simulation program, which is based on GEANT [73]. Finally, the simulated events are passed through the standard event reconstruction program, in the same way as the data events.

The event sample obtained in this way is called the Monte Carlo sample. Using it, most quantities of interest can be calculated with a statistical accuracy decreasing as $\frac{1}{\sqrt{N_{\mathrm{MC}}}}$ when one increases the number of Monte Carlo events N_{MC}. Below the two steps important in the generation of Monte Carlo events are described in more detail.

3.3.1 Event Generators

Usually the generation of the particles produced in a simulated e^+e^- collision happens in two steps. First the particles that are produced in the electroweak part of the physics process are generated by programs dedicated to this. An example of this would be the generation of four quarks for the process $e^+e^- \rightarrow W^+W^- \rightarrow q\bar{q}q\bar{q}$. The particles are then stored, and if necessary a second program is called for the fragmentation and hadronization. In the example just given this would be done to describe the production of hadrons from the four quark system.

Electroweak Event Generators

The following programs are commonly used in L3 .

- **KORALW** [74, 75]. This is the L3 standard event generator for the generation of WW events. KORALW can generate events according to the CC03 diagrams for WW production, or alternatively it can generate more general $e^+e^- \to f\bar{f}f\bar{f}$ using the matrix elements of GRACE [76]. In L3 it is typically used in the CC03 mode. KORALW can generate multiple photons from initial and final state radiation using an $\mathcal{O}(\alpha)$ YFS exponentiated calculation. Radiation in higher orders of α are included in the leading log approximation. KORALW treats τ decays with an interface to the TAUOLA [77] program. The full CKM matrix is included, so that also CKM-suppressed W decays, such as $W^+ \to u\bar{s}$, are included. The Coulomb interaction between the two W's is included in approximation. The matrix elements are, for technical reasons, calculated assuming zero fermion masses. For the event kinematics, however, the proper masses are used.

- **YFSWW3** [34] implements the $\mathcal{O}(\alpha)$ radiative corrections, including the non-factorizable ones, in the double pole approximation, and will mainly be used to estimate uncertainties due to radiative corrections.

- **EXCALIBUR** [78]. This program has as main advantage that all 4-fermion diagrams and their interferences are calculated, using a Weyl-van Waarden spinor technique. However, the program is of limited use for final calculations due to the fact that only collinear initial state radiation is implemented, using structure functions, no final state radiation is implemented by the authors, massless matrix elements and phase space are used, only a diagonal CKM matrix is implemented, and no Coulomb interactions are taken into account.

- **PYTHIA** [41]. This program is a versatile multi-purpose event generator with many options. It is not meant to be a state-of-the-art WW event generator, but it is used for systematic studies of color reconnection and Bose-Einstein correlations in WW events, as well as for the simulation of the $e^+e^- \to q\bar{q}(\gamma)$ and $e^+e^- \to ZZ$ backgrounds.

Fragmentation and Hadronization

For the simulation of fragmentation and hadronization, the programs JETSET [41], ARIADNE [43], and HERWIG [42] are used, as explained in Section 2.5.2. Each of these programs contain a number of free parameters that must be tuned such as to make the predictions of these programs agree with the data. The statistics of the LEP2 data is not sufficient to do this precisely, therefore high statistics Z data from LEP1 is used. The L3 tuning of these parameters is described in Reference [46]. A short summary is given here.

The HERWIG Monte Carlo event samples used in this thesis were generated with HERWIG version 5.9, the parameters $\Lambda_{\rm MLLA}$, CLMAX and CLPOW were tuned [79]. Here $\Lambda_{\rm MLLA}$ denotes the cut-off parameter used in the simulation of the perturbutive QCD shower, calculated using the Modified Leading Log Approximation. The paramaters CLMAX and CLPOW control whether a cluster will split before hadronisation. In JETSET 7.4 and ARIADNE 4.08 (linked to PYTHIA 5.7), the tuned parameters were $\Lambda_{\rm LLA}$, b and $\sigma_{\rm q}$ [46]. Here $\Lambda_{\rm LLA}$ is again the QCD cut-off parameter, where LLA indicates that JETSET uses the Leading Log Approximation. The parameter b is part of the Lund fragmentation function, and $\sigma_{\rm q}$ controls the smearing of the hadronic transverse momenta. The tuning was performed on corrected Z data distributions of four variables, which were chosen such as to minimize the correlations between them: y_{34} in the JADE algorithm, the minor thrust evaluated in the hemisphere with the narrow jet, the fourth Fox-Wolfram moment, and the charged multiplicity distribution. The quality of the tuning was subsequently tested on 14 other variables, including the major event shape variables. A χ^2 per degree of freedom, $\chi^2/\text{d.o.f.}$, was calculated for each tuning, with the simplification of not taking into account the correlations between the variables:

- JETSET: For the four variables used in the tuning, $\chi^2/\text{d.o.f.} = 30.3/53$, and for all 18 variables $\chi^2/\text{d.o.f.} = 237/226$;
- ARIADNE: $\chi^2/\text{d.o.f.} = 25.9/53$ for the four tuning variables, and $\chi^2/\text{d.o.f.} = 188/226$ for all 18 variables;
- HERWIG: $\chi^2/\text{d.o.f.} = 85.4/53$ for the four tuning variables, and $\chi^2/\text{d.o.f.} = 347/226$ for all 18 variables.

It is clear that HERWIG does not describe the Z data as well as JETSET or ARIADNE, even after the tuning. This holds not just for one or two distributions, but for the majority of them. Further investigation of differences between JETSET and HERWIG revealed a number of problems with version 5.9 of HERWIG, which were corrected in a later version HERWIG 6.1. At the time of writing of this thesis, tuning of HERWIG 6.1 was still in progress, and no event samples were available yet.

The tuning of JETSET was performed with Bose-Einstein correlations switched on, using the BE_0 variant of the LUBOEI algorithm. A set of tuned variables also exists for JETSET without Bose-Einstein correlations [80]. It has been checked that the set with Bose-Einstein correlations switched on also describes the data well if the BE_{32} variant is used [81].

The parameter tuning used in the Monte Carlo samples used in this thesis was performed on L3 data taken at $\sqrt{s} \approx m_Z$ in 1991. Recently, the parameters were retuned for PYTHIA 6.1, which incorporates JETSET, with a larger sample of Z data events [82]. Although no Monte Carlo event samples were available yet at the time of writing of this thesis, it is interesting to look at the new tuning results. The new tuned parameters differ from the old

parameters by 0.3 to 1.3 (old) standard deviations, and have errors that are 2.0 to 2.5 times smaller.

3.3.2 Detector Simulation

The L3 detector simulation tries to mimic as best as possible the response of the L3 detector to particles created in the collision and entering the detector. It is based on the GEANT [73] package, which offers a modular framework to define the detector geometry, define particles and their properties, track particles through the detector including the effects of the magnetic field, deposit energy in sensitive detector elements, and simulate the response of the detector to such energy deposits.

During the tracking, particles may interact with the material they cross, leading to processes like ionization energy loss, bremsstrahlung, multiple scattering, pair production or nuclear interactions, or they may decay into other particles. GEANT contains a set of routines to simulate each of these processes, as well as general bookkeeping routines to ensure that the cross sections of the interactions and the particle lifetimes are correct. GEANT keeps tracking the particles until their decay or capture, or until their energy falls below a predefined cut-off, below which the detector is no longer sensitive to the particle.

Most particles that enter the ECAL or HCAL will start a shower of secondary and further particles, and will eventually be absorbed, depositing all their energy in the calorimeter. In the L3 detector simulation program, electromagnetic and hadronic showers are fully simulated, no use is made of any shower libraries or parametrizations. Electromagnetic showers are simulated by GEANT itself, whereas the hadronic shower simulation is based on the GHEISHA [83] program.

Detector parts can be declared "sensitive" if they correspond to a part of the real detector that actually contributes to a measurement of a property of the particle passing through it. Energy deposits in these detector parts form "hits", which are used to simulate as accurately as possible the actual detector output in the form of "digitizations".

Although the detector simulation tries to simulate the response of L3 as accurately as possible, it cannot simulate very well a number of time-dependent effects. These effects include inactive cells or wires in the TEC or muon chambers, inactive silicon sensors in the SMD, inactive BGO crystals in the ECAL, noise in the SMD, ECAL or HCAL, small variations in the drift gas in the TEC or muon chambers, and the time dependence of the BGO light output. For a good description of the data, simulation of these effects is required. This is performed in a dedicated step after the initial simulation. Samples of simulated events are mapped onto the data taking period for which they are simulated, proportional to the amount of luminosity gathered. Then, using a data base of time-dependent effects, corrections to the initial simulation are applied in this so-called "realistic detector simulation". All Monte Carlo simulated events used in the analyses described in this thesis have been subjected to this procedure.

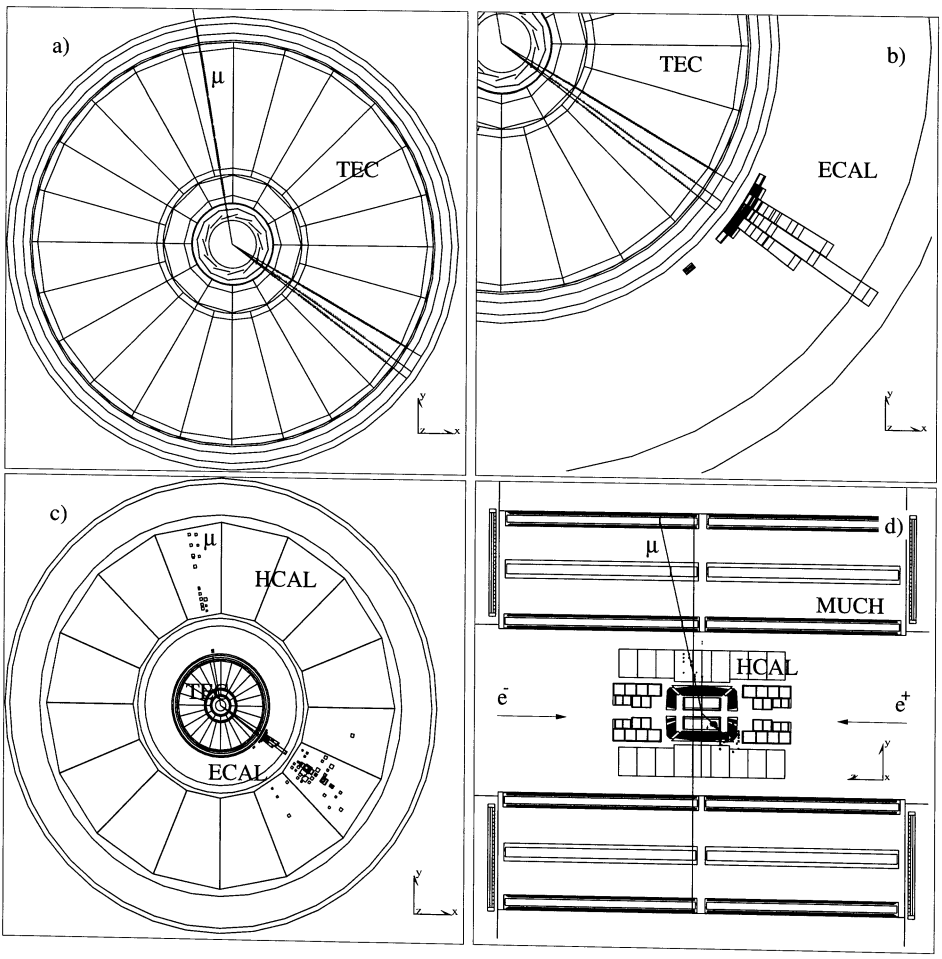

Figure 3.6: *Various views of an* $e^+e^- \rightarrow W^+W^- \rightarrow \mu^-\bar{\nu}_\mu\tau^+\nu_\tau$ *event candidate. a): TEC view. b): view of the energy in the EM calorimeter (ECAL). c): HCAL view showing hadronic energy deposit and a minimum-ionization trail for the muon. d): View of the muon chambers (MUCH).*

Chapter 4

Event Reconstruction

The reconstruction of data taken with the L3 detector is done in several steps. First the raw data are processed. In this phase the digitized output signals of all detectors are converted to physically meaningful quantities, like energies and locations of hits, using the most recent calibrations available. Next, the individual subdetector signals are combined into higher level objects, for instance clusters or tracks. From these, quantities relevant for the detection and reconstruction of W^+W^- events are calculated. This procedure is briefly summarized in this Chapter.

4.1 Track Reconstruction

To construct tracks, the hits in the SMD, TEC and z-chambers have to be combined into a number of patterns. In events with multiple charged particles there can be hundreds of hits, making this a difficult task. The procedure adopted is to start the pattern recognition by analyzing the hits in the TEC using a Minimum Spanning Tree [84] algorithm. In short, the algorithm starts by combining hits on adjacent wires into a doublet. Then, doublets having a hit in common are added together to form trees. If more than one doublet can be added, the one that gives the smallest increase in the tree length is taken. Once no more doublets can be added, a circle is fitted to the tree. If the fit is good, the tree is accepted as a valid track segment. When all track segments have been found, the compatible ones are combined, in such a way that the longest possible tracks are formed.

After the tracks in the TEC have been found, each track is extrapolated to the z-chambers. With the combined z and $r\phi$ information obtained using the 70° angle between the second and third z-chamber plane and the z-axis, hits in the z-chamber can be matched to the tracks. Similarly, tracks are extrapolated to the SMD, and matching hits are again added. Once it is determined which hits are assigned to a track, a circle fit is performed to all hits to determine the optimal track parameters.

4.2 Cluster Formation in the Calorimeters

To form clusters, nearby hits in the individual calorimeter components (crystals for the ECAL, towers for the HCAL) have to be combined. For the ECAL, clusters are defined as continuous regions of crystals where at least 10 MeV is deposited in each crystal. For the HCAL, the minimum energy of a tower is nine MeV. As the HCAL segmentation is three dimensional, the clustering is in this case done in three dimensions. The principle behind the algorithm is again the association of nearby hits.

In the next phase, ECAL and HCAL clusters are combined into so-called "smallest resolvable clusters". This is also done on basis of proximity. Three dimensional information is used, for instance ECAL clusters are never combined with HCAL clusters which only have energy deposits in the outermost part of the detector.

4.3 Energy Determination

Finally, the energy of the cluster formed as described above has to be determined from the energy deposits in the individual detector components associated to the cluster. For this it is important to realize that the cluster can reflect a single particle, but this is not always the case. For instance, for a high energy tau lepton in the process $\tau^- \rightarrow \pi^-\pi^0\nu_\tau$, all decay products are frequently reconstructed as one cluster, reflecting the original tau lepton instead of its decay products. In practice, the L3 detector has insufficient precision to distinguish between all different cluster types and perform a complete energy flow analysis, so that for most clusters no attempt has been made to make a particle identification. The only exceptions are isolated photons, electrons and muons. The first two, electromagnetic, particles can usually be recognized by a narrow shower in the ECAL, with most energy concentrated in the central crystal and no or relatively low energy deposit in the hadronic calorimeter. In this case the energy of the particle is estimated by the energy measured in the ECAL. Muons can be recognized by a number of hits in the muon chambers, consistent with a track coming from the vertex where the electron positron pair collides. The momentum of the muon is estimated by measuring the curvature of the track. For all clusters not explicitly identified a pragmatic approach is taken instead: these clusters are considered to be massless, and the energy measurement is done as described below, without any assumptions regarding the particle identity.

In the schematic layout of the L3 detector in Figure 4.1 the subdetectors are shown and grouped into twelve classes (for historical reasons no detector is associated with the number five, the energy here is set to zero). For the energy measurement, the energies measured in the subdetectors have to be combined. The energy of a cluster can be written as

$$E_{clus} = \sum_{i=1}^{12} g_i E_i, \tag{4.1}$$

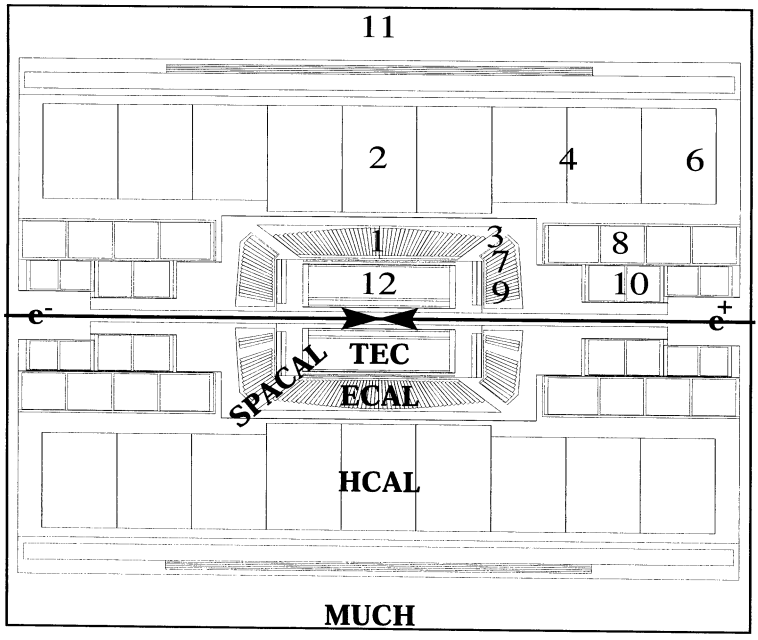

Figure 4.1: *Schematic view of the* L3 *detector with the twelve regions used for the energy measurement. For historical reasons no detector is associated with region five.*

where the E_i are the energies measured in subdetector i and g_i are the so called g-factors. In principle one would expect that the best measurement would be obtained with all g_i equal to one, assuming all subdetectors have been calibrated correctly. For a variety of reasons this is not the case. The ECAL, for example, has been calibrated under the assumption that the particle loses energy in the detector due to an electromagnetic shower, as is the case for photons and electrons. For particles with an electromagnetic signature , the g-factors corresponding to the ECAL are therefore indeed set to one. For hadronic particles in the ECAL the interaction mechanism is different, with sizable energy deposits mainly arising from nuclear interactions. The standard ECAL calibration will in this case not give the best estimate for the energy deposition, which is one of the reasons why the g_i deviate from one for particles without electromagnetic signature. Other reasons can be energy absorption in front of the detector, for example by cables or support structures, so that only a part of the particle energy can be measured. In this case, even a perfect measurement of the energy deposited in the detector would still underestimate the energy of the original particle. This can be partially compensated by a g-factor larger than one. Likewise, the g-factors can compensate for energy leakage due to holes in the detector, or undetected particles like

neutrinos.

A separate issue is the reconstruction of clusters which have an energy deposition in the calorimeter that has been matched to one or more tracks in the central drift chamber, the TEC. In this case, the energy of the charged particles associated with the cluster is measured by the TEC, again assuming the particles are massless, as well as by the calorimeters. Simply adding both measurements would clearly lead to some double counting. For clusters reflecting just one charged particle one would expect the optimal energy resolution to be obtained by taking a weighted average of the TEC and calorimeter measurements. However, in practice it is not always possible to distinguish between clusters with only charged particles and clusters containing both charged and neutral particles. A more pragmatic approach is taken, and two sets of g-factors are created: one for clusters with energy measured in the TEC, and one without. The first set will then correct for the double counting by lowering the g-factors, while the second set will give an optimal energy measurement using the calorimeters alone.

To determine the values for the g_i giving the best energy resolution, a high statistics sample of hadronic events, $e^+e^- \rightarrow q\overline{q}$, is selected. For this channel a high efficiency and purity are obtained. The total visible energy per event can be defined as the sum of all $N_{\rm clus}$ cluster energies, i.e. $E_{\rm vis} = \sum_{j=1}^{N_{\rm clus}} E_j$. If all energies are measured perfectly, the visible energy should be equal to twice the beam energy $E_{\rm beam}$. This provides an excellent way of determining the g-factors using the data by minimizing the visible energy resolution

$$\sigma_{E_{\rm vis}}(g_i) = \sqrt{\frac{1}{N_{\rm events}} \sum_{j=1}^{N_{\rm events}} (E_{{\rm vis},j}(g_i) - 2E_{\rm beam})^2} \tag{4.2}$$

with respect to the g-factors g_i. Here $N_{\rm events}$ denotes the number of selected hadronic events. This procedure ensures the proper energy scale as well as the optimal resolution on the visible energy. The data used are the calibration data at $\sqrt{s} = m_{\rm Z}$, taken prior to each high energy run, where the high cross section ensures sufficient statistics.

If the detector response would be described perfectly in the Monte Carlo simulation, the g-factors obtained from the data could be used in the reconstruction of Monte Carlo events. In practice some differences between data and Monte Carlo unfortunately remain. For instance effects like noise, calibration effects or the exact amount of materials in front of a detector are difficult to model accurately.

To some extent it is possible to improve on the situation by using a different set of g-factors for the Monte Carlo. In the implementation used for this analysis, the average energy deposition per detector region i, E_i^{av}, is determined for the calibration data and an equivalent Monte Carlo sample. The g-factors applied for the Monte Carlo are then those as determined for the data, but scaled according to

$$g_i^{MC} = \frac{E_i^{av,data}}{E_i^{av,MC}} \, g_i^{data}. \tag{4.3}$$

An alternative procedure to derive g-factors, not using the TEC for the cluster energy measurements, is described in Reference [85]. The g-factors for the data are obtained as described above, except that the data used is not the calibration sample taken at $\sqrt{s} = m_Z$, but the high energy data sample. The g-factors for the Monte Carlo are now also obtained by minimizing equation 4.2, except now using a Monte Carlo sample corresponding to the high energy data. A comparison of the energy measurement with the standard and the alternative g-factors will be used to assign a systematic error on cross section and mass measurements due to uncertainties in the energy measurement in Chapters 5 and 6.

4.3.1 Related Analysis Variables

In the selection of $e^+e^- \rightarrow W^+W^- \rightarrow q\bar{q}q\bar{q}$ events, use is made of a number of variables related to the cluster formation and energy reconstruction:

- E_{vis}: the total visible energy, calculated from all clusters after application of g-factors;
- E_{long}: the "longitudinal" energy, calculated from all clusters after application of g-factors, by projection of the cluster energy on the z-axis: $E_{\text{long}} = \sum E_{\text{clus}} \cdot \cos\theta_{\text{clus}}$. E_{long} should be close to zero for a balanced event;
- Cluster multiplicity: the number of reconstructed clusters with an energy of 300 MeV or more, after application of g-factors;
- $\max(E_{\text{BGO}})$: the BGO energy of the cluster with the largest energy deposit in the ECAL. The cluster is assumed to be produced by an electron or photon, and no g-factors are applied;
- Sphericity [86]: let Q_1, Q_2 and Q_3 be the ordered, $Q_1 \leq Q_2 \leq Q_3$, eigenvalues of the momentum tensor s^{ij} defined as

$$s^{ij} = \frac{\sum_a p_a^i p_a^j}{\sum_a p_a^2} \quad i,j = 1,2,3;$$

where the sum runs over all particles labeled "a" in the event, and where p_a^i is the i^{th} component of the momentum vector $\vec{p_a}$. The sphericity S is then defined as

$$S = \frac{3}{2}(Q_1 + Q_2).$$

Values of S are close to zero for pencil-like events, and close to one for spherical events.

4.4 Jet Reconstruction

After the clusters have been formed, the next step of the analysis is to combine them into groups which give a good representation of the underlying event structure, i.e. in the context of this analysis the four primary quarks . This procedure assumes that each cluster represents a particle that can be unambiguously assigned to one of the original quarks. A procedure without this assumption has been suggested [87, 88]. While being a simplification, the approach adopted here gives a more intuitive picture and the assumption made proves to be an adequate approximation of the more complicated physical reality.

The DURHAM algorithm [89] is used for the combination of clusters. Out of the list of the reconstructed particles, the pair (i,j) with the minimal distance y_{ij} is chosen. The DURHAM algorithm defines the distance as

$$y_{ij} = \frac{2\min(E_i^2, E_j^2)(1-\cos\theta_{ij})}{\sum_{k=1}^{N_{\text{clus}}} E_k}, \tag{4.4}$$

where E_i, E_j are the energies of clusters i, j and θ_{ij} is the angle between the clusters i and j. These two, "closest", particles are replaced in the list by a single object obtained by adding their four-momenta. The procedure is then repeated until a predefined number of objects is reached. The resulting objects are called jets, assumed to correspond to the original quarks. It should be noted that adding the four-momenta of two particles that have a non-zero angle between them introduces a mass for the jet, even if the two original particles are massless.

For this analysis, four jets are constructed with this algorithm for each event. The smallest distance between any two of those jets, calculated with Formula 4.4, is denoted as y_{34}. As described in Chapter 5, this quantity provides an important criterion for separating four-jet events from two- and three-jet events.

Other jet algorithms that have been studied are JADE [90], LUCLUS [91], DICLUS [92], angular ordered DURHAM and CAMBRIDGE [93]. The performance expected from Monte Carlo studies for these algorithms is comparable to the one obtained using the DURHAM scheme. As an example of this, the jet-jet invariant mass after a constrained fit in Monte Carlo $e^+e^- \rightarrow W^+W^- \rightarrow q\bar{q}q\bar{q}$ events in shown for two algorithms, LUCLUS and DURHAM, in Figure 4.2. The figure shows that there is no significant difference in the overall performance (a), but that there can be large differences per event for a fraction of all events (b): for some events the jet clustering is unstable, an infinitesimal difference in input can lead to totally different jets. For an overview of these jet algorithms see also Reference [94].

4.4.1 Related Analysis Variables

In the selection of $e^+e^- \rightarrow W^+W^- \rightarrow q\bar{q}q\bar{q}$ events, use is made of a number of variables related to the jet reconstruction:

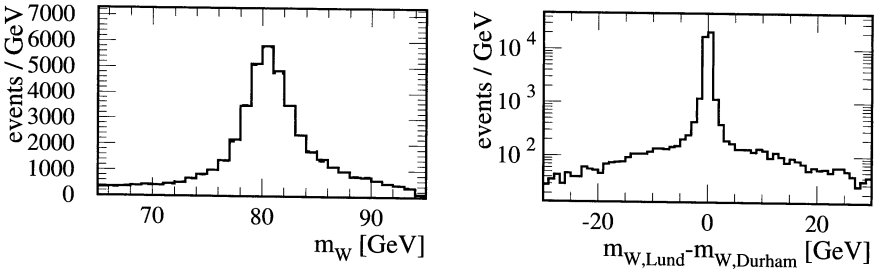

Figure 4.2: *Left: jet-jet invariant mass after a constrained fit in Monte Carlo* $e^+e^- \to W^+W^- \to q\bar{q}q\bar{q}$ *events for the DURHAM algorithm (full histogram) and the LUCLUS algorithm (dashed histogram, almost identical to the full histogram). Right: event-by-event difference between the two algorithms.*

- $\max(E_{\mathrm{ASRC}}/E_{\mathrm{jet}})$: the maximum fraction of jet energy taken by a single cluster in all reconstructed jets. This should be relatively small for a true hadronic jet, and is typically large for a jet formed by an isolated particle;
- $\log(y_{34})$: the logarithm of the value of y in the DURHAM jet finder at which the event changes from a 4-jet to a 3-jet topology;
- $\min(E_{\mathrm{jet}})$, $\max(E_{\mathrm{jet}})$: minimum and maximum of the energies of the reconstructed jets;
- $\min(\theta_{\mathrm{jet-jet}})$: smallest angle between any two of the reconstructed jets;
- $m_{\mathrm{hemisphere}}$: average mass of the jets if the event is forced into a 2-jet topology.

4.5 Constrained Fitting

In genuine $e^+e^- \to W^+W^- \to q\bar{q}q\bar{q}$ events typically a very small fraction of energy is carried away by undetected initial state radiation photons, while most of it is distributed in the multi-hadron system resulting from the fragmentation of the four quarks. Given an ideal detector, the four-momenta of the reconstructed jets should in good approximation sum up to the total four-momentum of the initial electron-positron system. This is not realized in practice due to the finite resolution of the detector. However, due to the known four-momentum conservation, constraints can be put on the sum of the measured jet energies and momenta. By exploiting these constraints one can improve the measurement of the reconstructed jet

parameters. This is done by varying the measured jet energies and angles in such a way that the four constraints:

$$\sum_{i=1}^{4} E_i = \sqrt{s} \tag{4.5}$$

$$\sum_{i=1}^{4} \vec{p}_i = \vec{0} \tag{4.6}$$

are satisfied by the new, fitted, jet parameters. As there are more jet parameters that can be varied than equations to satisfy, many sets of parameters can fulfill the constraints. The solution minimizing:

$$\chi^2 = \sum_{i=1}^{4} \frac{(E_i - E_{i,0})^2}{\sigma_E^2(E_i,\theta_i)} + \frac{(\theta_i - \theta_{i,0})^2}{\sigma_\theta^2(E_i,\theta_i)} + \frac{(\phi_i - \phi_{i,0})^2}{\sigma_\phi^2(E_i,\theta_i)} \tag{4.7}$$

is chosen, where $E_{i,0}, \theta_{i,0}$ and $\phi_{i,0}$ denote the measured parameters of jet i and E_i, θ_i, ϕ_i are the fitted parameters of jet i. The measurements are assumed to be uncorrelated, and to have Gaussian errors. The jet velocities $\beta = \frac{|\vec{p}|}{E}$ are kept constant at their measured values during the minimization. This reduces the number of free parameters in the fit without compromising the resolution on the fitted parameters.

An important element of the χ^2 calculation are the estimates of the jet measurement errors. The resolutions depend on jet energy E and polar angle θ and are parametrized as:

$$\begin{aligned}
\sigma_E &= \sqrt{E}\sqrt{a_E + \tfrac{b_E}{E}} \quad \left(1 + \tfrac{c_E}{\min(\theta,\pi-\theta)} + d_E|\theta - \tfrac{\pi}{2}|^2\right) \\
\sigma_\theta &= \tfrac{1}{\sqrt{E}}\sqrt{a_\theta + \tfrac{b_\theta}{E}} \quad \left(1 + \tfrac{c_\theta}{\min(\theta,\pi-\theta)} + d_\theta|\theta - \tfrac{\pi}{2}|^2\right) \\
\sigma_\phi &= \tfrac{1}{\sqrt{E}}\tfrac{1}{\sin\theta}\sqrt{a_\phi + \tfrac{b_\phi}{E}} \quad \left(1 + \tfrac{c_\phi}{\min(\theta,\pi-\theta)} + d_\phi|\theta - \tfrac{\pi}{2}|^2\right),
\end{aligned}$$

where the parameters a_x, b_x, c_x, and d_x are determined from studies of $e^+e^- \rightarrow W^+W^- \rightarrow q\bar{q}q\bar{q}$ Monte Carlo events [95].

Technically the constrained fit is performed by a numerical minimization of the χ^2 defined in equation 4.7, using the gradient descent method implemented in the MINUIT [96] software package. A penalty contribution:

$$\Delta\chi^2{}_{4C} = \frac{(\sum_{i=1}^4 E_i - \sqrt{s})^2}{\sigma_1^2} + \frac{(\sum_{i=1}^4 p_i^x)^2 + (\sum_{i=1}^4 p_i^y)^2}{\sigma_2^2} + \frac{(\sum_{i=1}^4 p_i^z)^2}{\sigma_3^2}, \tag{4.8}$$

with values of $\sigma_{1,2,3}$ of the order of 100 MeV, is added to the χ^2 to impose the constraints. This value is chosen to combine a fast convergence of the fit with the fulfillment of the constraints well within the experimental resolutions. The fit described above is referred to as a four-constraints, 4C, fit.

If the assumptions implicit in the definition of the χ^2 and the constraints are correct, the resulting $\chi^2{}_{4C}$ should have a χ^2 distribution with four degrees of freedom. The constrained

fit probability $P_{\chi^2_{4C};4}$, defined as the probability of drawing a value higher than the observed χ^2, should then be uniformly distributed in the [0,1] interval. As shown in Figure 4.3c and d, the resulting distribution for $e^+e^- \rightarrow W^+W^- \rightarrow q\bar{q}q\bar{q}$ events is indeed reasonably flat apart from the peak of events with very small probability. The peak is mostly due to non-Gaussian tails in the jet parameter resolutions.

The effect of the constrained fit on the jet energy estimates is illustrated in Figure 4.3a using W^+W^- Monte Carlo events. The resolution can be seen to be improved by a factor of $\sim$2.6 by the fit. In Figure 4.3b a similar plot is shown for the average reconstructed W mass. For this quantity the resolution is improved by a factor 4.

The experimental statistical error on a reconstructed W mass is of the order of 10 GeV. This is much larger than the intrinsic width of a W boson, which is of the order of $\Gamma_W \approx$ 2 GeV. Therefore it is reasonable to assume that both W bosons in the event have identical mass and apply this as an additional constraint in the constrained fit. The fifth constraint improves the resolution on the reconstructed average W mass by about 5%, contradicting the findings reported in [97].

In order to calculate two W masses, the four jets have to be combined into two jet pairs, each assumed to correspond to a W boson. There are three ways to perform this combination, and it is not possible to determine, on an event-by-event basis, which combination is the correct one. A five-constraints, 5C, fit is therefore applied to each of the three combinations. Technically the fifth constraint is implemented by adding a penalty contribution:

$$\Delta\chi^2_{5C,i} = \Delta\chi^2_{4C} + \frac{(m_{W1} - m_{W2})^2}{\sigma_4^2}, \tag{4.9}$$

where σ_4 is of the order of Γ_W. The $\chi^2$of the fit should be distributed according to the χ^2distribution with five degrees of freedom and can again be converted into a probability $P_{\chi^2_{5C};5}$. If the assumptions made for the 4C fit, as well as for the equal mass constraint, are correct, $P_{\chi^2_{5C};5}$ should have a flat distribution in [0,1]. The probability $P_{\chi^2_{5C};5}$ for the dijet combination with the highest probability is shown in Figure 6.1 in Chapter 6.

4.5.1 Related Analysis Variables

The selection of $e^+e^- \rightarrow W^+W^- \rightarrow q\bar{q}q\bar{q}$ events and the W mass analysis make use of the following event variables related to the constrained fit:

- $P_{\chi^2_{5C};5}$ and all fitted jet quantities. If not mentioned otherwise, jet parameters are 4C-fitted.

- For the cross section determination, use is made of the two W masses m_{W_1} and m_{W_2}, as determined after a 4C constrained fit. Three pairings of jets into W's are possible, chosen is the combination with the smallest mass difference between the two W's after first rejecting the combination with the smallest sum of masses. From Monte

Carlo events at $\sqrt{s} = 189$ GeV we estimate this choice to be correct for approximately 72% of the events. W_1 is defined as the W with the most energetic jet.

- For the W mass analysis, the masses resulting from a 5C fit are used, ordered in probability $P_{\chi^2_{5C};5}$.

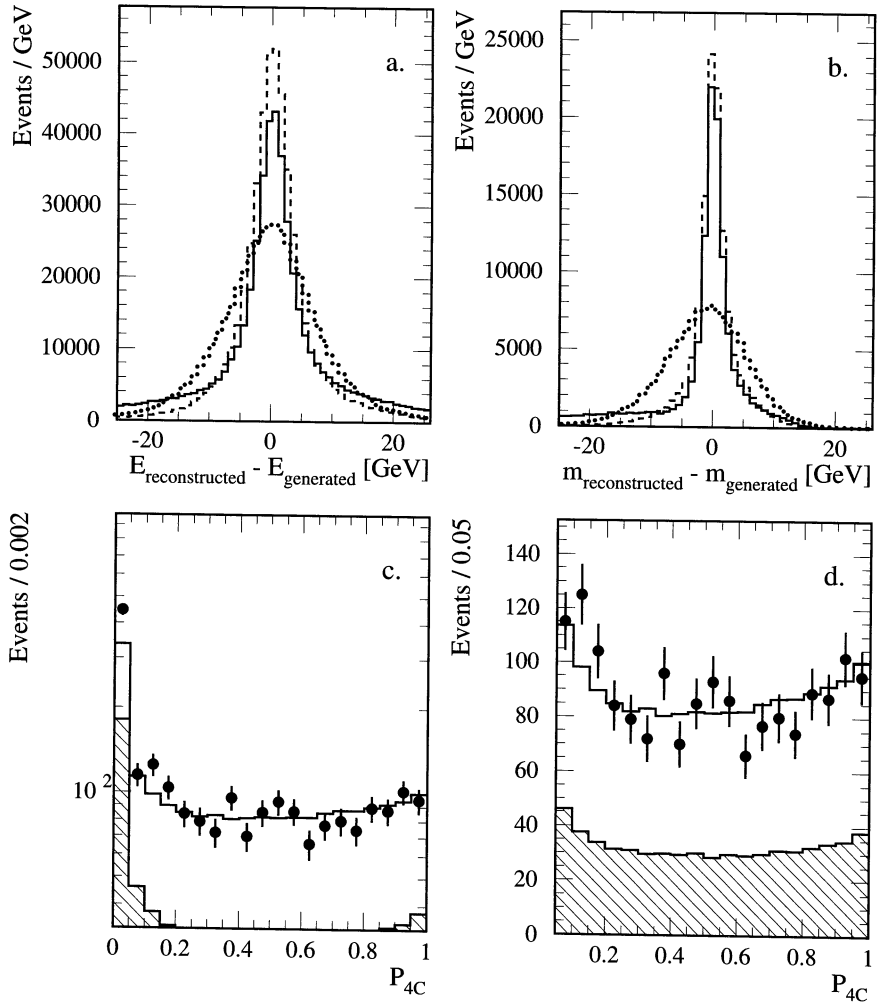

Figure 4.3: *a: Difference between reconstructed and generated jet energies in Monte Carlo* $e^+e^- \rightarrow W^+W^- \rightarrow q\bar{q}q\bar{q}$ *events before the constrained fit (dotted histogram), after a 4C constrained fit (full histogram), and after a 5C constrained fit (dashed histogram). b: The same for the average reconstructed and generated W masses. c and d: Distribution of the probability of the* χ^2 *of the 4C constrained fit,* $P_{\chi^2_{4C};4}$ *for* $e^+e^- \rightarrow W^+W^- \rightarrow q\bar{q}q\bar{q}$ *events after preselection, with a logarithmic vertical scale for all events in c, and with a linear vertical scale for* $P_{4C} > 0.05$ *in d. Dots are data, open histogram is WW signal, dashed histogram is background.*

Chapter 5

Event Selection and Cross Section Results

At LEP2 many processes generate final states that are observed with the L3 detector. In Figure 5.1 the calculated Standard Model cross sections of some of these processes are shown as a function of $\sqrt{s}$, the total energy in the center-of-mass system. Clearly it is important to select W^+W^- events with a high efficiency while at the same time rejecting most of the events coming from other final states, which are background for W-physics purposes. As the W^+W^- event signatures are dependent on the decay modes of both W bosons the event selection is different for the following cases:

- both W bosons decay to a charged lepton and a neutrino or anti-neutrino (leptonic decay mode);
- one W boson decays to a quark and an anti-quark, the other to a charged lepton and a neutrino or anti-neutrino (semi-leptonic decay mode);
- both W bosons decay to a quark and an anti-quark (hadronic decay mode).

For the event selection the emphasis of this thesis is on the latter, the fully hadronic, decay mode. The analysis of the data taken at $\sqrt{s} = 189$ GeV is presented in detail, for the data taken earlier the results are given.

5.1 Introduction

For the case where both W bosons decay to a quark–anti-quark pair, the experimental signature of the event is the observation of four hadronic jets, in general well separated. As discussed in Chapter 4, the jets can be combined to form two jet pairs with each a dijet mass approximately equal to the W boson mass. The main backgrounds are the processes $e^+e^- \rightarrow q\bar{q}$, $e^+e^- \rightarrow ZZ$, and the W^+W^- events in which one of the W's decays to a lepton and an anti-neutrino.

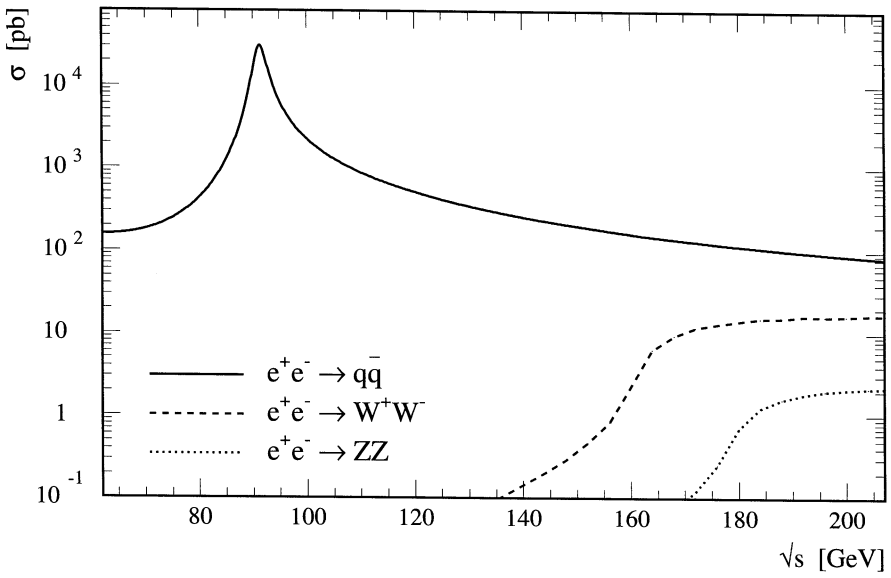

Figure 5.1: *The Standard Model predictions for the* W^+W^- , $q\bar{q}$ *and ZZ cross sections as a function of the center of mass energy* $\sqrt{s}$.

The process $e^+e^- \rightarrow q\bar{q}$ can be split into a "high energy" and a "radiative return" class. In the latter case an initial state radiation photon is emitted with an energy such that the Z in the intermediate state is on or near its mass shell, therefore enhancing the production cross section considerably. An $e^+e^- \rightarrow q\bar{q}$ event from either class can be mistaken for a four jet event as gluon radiation, initial state radiation and/or misreconstruction can form or fake the third and fourth jet. As can be seen in Figure 5.1, and taking into the account the fully hadronic W^+W^- branching fraction given in Chapter 2, the cross section for $e^+e^- \rightarrow q\bar{q}$ is significantly larger than the cross section for $e^+e^- \rightarrow W^+W^- \rightarrow q\bar{q}q\bar{q}$. At the W production threshold it is in fact larger by two orders of magnitude. A powerful way of rejecting this background is therefore important.

For the process $e^+e^- \rightarrow ZZ$ the situation is different. The signature for ZZ events where both Z's decay to hadrons is similar to the W^+W^- signature, making it very difficult to efficiently reject this background without cutting too much of the signal away. Fortunately the cross section for this process is small compared to the signal cross section, and although the ZZ cross section rises with $\sqrt{s}$ the $q\bar{q}$ background will remain dominant.

The background from non-four jet W^+W^- events arises mostly from events where one of the W bosons decays into $\tau\nu_\tau$ and the other one into a quark–anti-quark pair. In these

cases two genuine jets exist from one W, and the lepton can be interpreted as a third. A hard gluon radiated from one of the quarks or misreconstruction can then fake a fourth jet. The accepted background due to these events is small, but as the cross section is proportional to the signal cross section the fraction of accepted events with respect to the signal will remain roughly constant with $\sqrt{s}$.

Other possible background sources can be distinguished from the signal rather well and are rejected almost completely. The largest remaining background contribution arises from so called two photon events, where the initial state electron and positron both radiate a virtual photon. These photons subsequently collide and form hadrons which can be detected. Usually the final state electron and positron have a low angle with respect to the beam pipe, and the total invariant mass of the final state hadrons is of the order of a few GeV. These events therefore have a signature rather different from the signal, but as the cross section of this process is several orders of magnitude larger than the signal cross section, a few events could eventually pass the selection criteria.

The event selection is focused on the rejection of the dominant background source, $\mathrm{q\bar{q}}$ events. For optimal performance the selection is done in two steps. First, a loose selection is applied to obtain a set of promising four jet candidates. In this phase the events clearly incompatible with a hadronic four jet structure are rejected, while almost all the signal is preserved. Next, a neural network trained to separate $\mathrm{q\bar{q}}$ events and $\mathrm{W^+W^-}$ events is used for the final selection.

5.2 Selection

To obtain a sample of good $\mathrm{W^+W^-}$ candidates a selection is performed using the variables described in Chapter 4. In Figure 5.2 the $\sqrt{s} = 189$ GeV data and corresponding Monte Carlo expectations are plotted for the important quantities used in the selection. The following cuts are applied:

- $E_{\mathrm{vis}}/\sqrt{s} > 0.7$. The visible energy of the signal events is expected to be around $\sqrt{s}$. This cut suppresses events from background sources where energy is lost, such as two photon or "radiative return" events, as well as detector noise.

- Cluster multiplicity > 30. Many background processes have a multiplicity much lower than expected for the signal, as the fragmentation of four quarks produces many particles scattered through phase space. Almost all signal events pass this criterion, whereas background from processes like $\mathrm{e^+e^-} \rightarrow \mathrm{e^+e^-}$ is practically completely removed. As can be seen in Figure 5.2c the multiplicity in the Monte Carlo is shifted with respect to the multiplicity in the data. This problem is related to the behavior of electromagnetic clusters with relatively low energy, which is not well simulated. Possible systematic

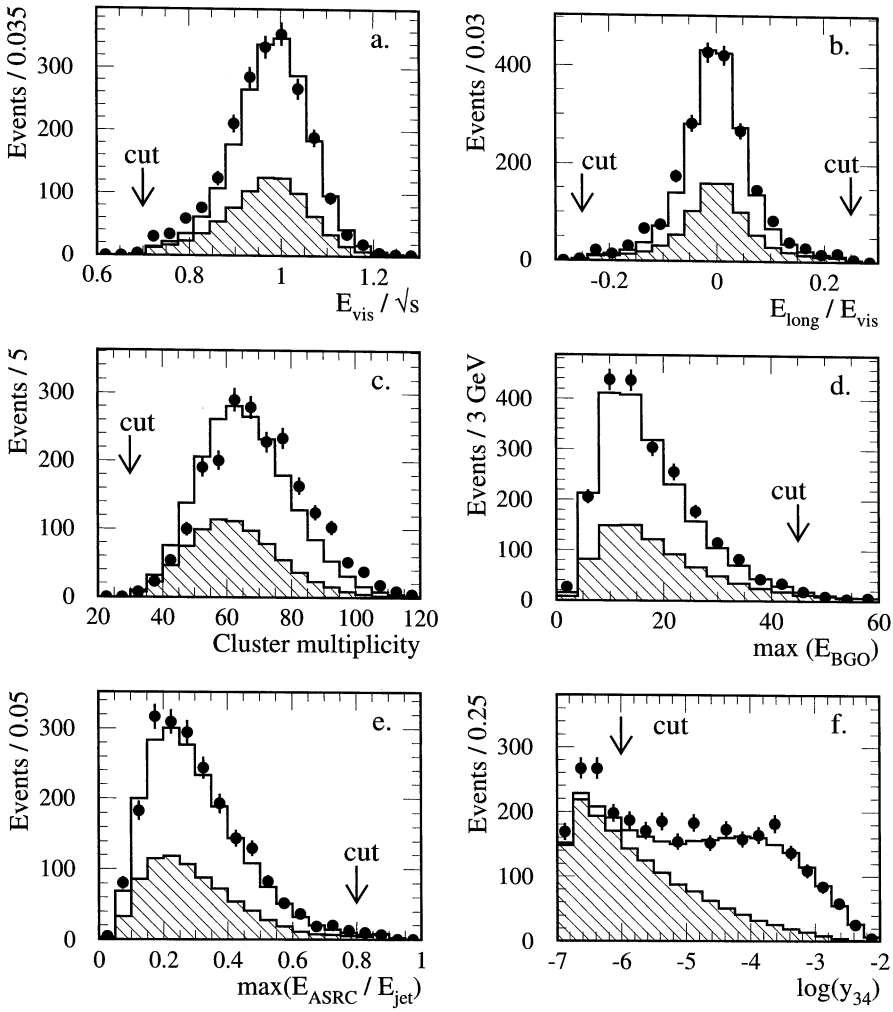

Figure 5.2: *The data collected in 1998 and corresponding Monte Carlo expectations for variables used in the preselection. All cuts except the one on the variable shown have been applied. The dots denote the data, the open histogram represents the total Monte Carlo expectation and the hatched histogram the sum of the background Monte Carlo expectations. Shown is respectively the visible energy scaled to* $\sqrt{s}$ *(a), the longitudinal energy (b), the cluster multiplicity (c), the maximum energy deposition of a cluster in the BGO part of the ECAL (d), the maximum energy fraction of a jet contained in a single cluster (e) and the logarithm of the jet resolution parameter* y_{34} *(f).*

errors due to this shift are expected to be small as this cut is effective mainly for background sources with a typical number of clusters much smaller than the cut value, whereas the typical multiplicity for the signal is much larger.

- $|E_{\text{long}}|/E_{\text{vis}} < 0.25$. Requiring a low value for the longitudinal energy imbalance selects balanced events. As most signal events are balanced events without missing energy this cut rejects almost no signal. The signal events that are rejected are mostly events where a jet is missing in the beam pipe. Background events are much more likely to miss energy in the forward or backward direction. For instance, events with a radiative return to the Z^0 often have a high energy photon lost in the beam pipe, while two photon events usually have an electron and/or positron with a low angle.

- $y_{34} > 0.001$. As explained in Chapter 4, this criterion selects events with a four jet like topology.

- $\max(E_{\text{BGO}}) < 45$ GeV. For a small fraction of the "radiative return" events the radiated photon is emitted with an angle to the beam pipe sufficiently large to be measured with the L3 detector. In the reconstruction of such an event, the photon, typically with a high energy, can be interpreted as an additional jet. To prevent this, events where a single cluster has a sizable energy deposition in the BGO part of the electromagnetic calorimeter are rejected.

- $\max(E_{\text{ASRC}}/E_{\text{jet}}) < 0.8$. If more than 80% of the energy of any jet is contained in a single cluster the event is rejected. Usually this type of jets are formed by a lower energy initial state radiation photon that passed the cut on the maximum BGO energy.

- $\max|p_\mu| < 20$ GeV, where p_μ is the momentum of a muon in the event. This cut mainly rejects W^+W^- events where one of the W's decays to a muon and a muon (anti-)neutrino, or events where one of the W's decays to a tau and a tau neutrino and the tau decays to a muon and two neutrinos.

- Noise rejection. Occasionally correlated noise in the hadronic calorimeter may be serious enough to fake a four jet event. As this HCAL noise is uncorrelated with other detector elements these events can be rejected by requiring at least ten good tracks (ATRK's) in the TEC. For events with exactly zero good tracks it is assumed the TEC is switched off and the noise rejection criterion is replaced by the requirement that the total energy deposition in the BGO barrel exceeds 20 GeV.

The efficiency of the preselection for the signal and various background sources is given in Table 5.1. For the background the accepted cross section that is expected from the Standard Model is also given.

	efficiency (%)	Accepted cross section (pb)
$W^+W^- \rightarrow q\bar{q}q\bar{q}$	92.3	
$W^+W^- \not\rightarrow q\bar{q}q\bar{q}$	2.0	0.18
$q\bar{q}$ background	4.2	4.13
ZZ background	40.4	0.39
two photon background	9×10^{-4}	0.04

Table 5.1: *Preselection efficiency and accepted background cross section for signal and background Monte Carlo for* $\sqrt{s} = 189$ GeV.

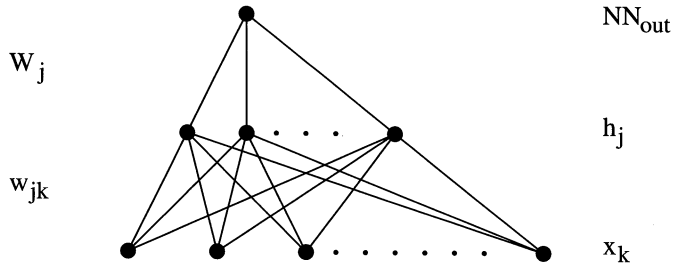

Figure 5.3: *Schematic layout of a three layer, feed forward neural network with one output node. The values of the input nodes are denoted by* x_k*, the values of the nodes in the hidden layer by* h_j *while the final value for the output node is* nn_{out}*. The weights of the connections between the input and hidden layers are denoted by* w_{jk} *and those of the connections between the hidden layer and the output node by* W_j*.*

5.3 Neural Network

As can be seen in Figure 5.2, there is no single variable which provides satisfactory separation between signal and background. As also many of the variables which can be used are correlated, it seems natural to exploit these correlations by using a multidimensional discriminator function $d = d(\vec{x}; \vec{p})$. Here $\vec{x}$ denotes a vector of input variables and $\vec{p}$ a vector of parameters which can be optimized to obtain good separation. In this analysis a function like this has been constructed using a neural network.

A simple neural network, similar to the one used, can be visualized by the architecture shown in Figure 5.3. Here the lowest layer of nodes represents the input parameters chosen to separate the signal from the background. For each input parameter k a value x_k between zero and one is calculated. These values are then used to calculate function values h_j for the nodes in the middle, hidden, layer. The neural net output nn_{out} is subsequently calculated

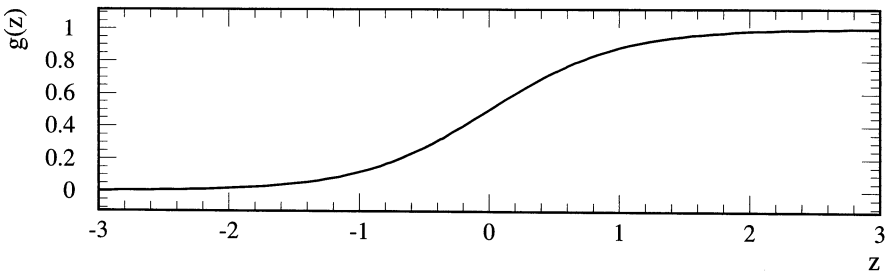

Figure 5.4: *Neural net activation function* $g(z) = [1 + \exp(-2z)]^{-1}$. *The characteristic sigmoid shape is visible, the function* $g(z)$ *is only sensitive to the value of* z *for small values of* $|z|$.

from the nodes in the hidden layer. This type of neural net is called a three layer, feed forward neural network with a single output node.

To calculate the function value of a node from the values x_k of the layer below a single parameter z is first calculated using the formula $z = \sum_k w_k x_k + \theta$. The value of the node is then obtained using the "neural activation function" $g(z) = [1 + \exp(-2z)]^{-1}$. This function has a characteristic sigmoid shape, as shown in Figure 5.4, and is responsible for the non-linear response of the network. In these formulas w_k denotes the weights with which the input values are combined, while θ shifts the resulting sum to keep the average value of z in the region where the activation function is sensitive. For a neural network of this type with N_{in} input nodes and N_h hidden nodes the behavior of the total network can be summarized in a single formula:

$$nn_{out} = g\left[\sum_{j=1}^{N_h} W_j g\left(\sum_{k=1}^{N_{in}} w_{jk} x_k + \theta_j\right) + \Theta\right]. \tag{5.1}$$

Here the weights and offsets between the input and hidden layer are denoted by w_{jk} and θ_j, and those between hidden and output layer are W_j and Θ.

The crucial point when using a neural network is to obtain good values for the free parameters in formula 5.1, the weights and offsets. This is done using a sample of simulated events called the training sample. For these events it is known whether they were generated as signal or as background, so that an error measure can be defined as $\sum_i (nn_{out,i} - t_i)^2$. Here the sum is taken over the entire training sample (both signal and background), and the target values t_i are one for signal events and zero for background events. By minimizing this error measure with respect to the weights and offsets proper values can be obtained. There are many algorithms available for this minimization. To obtain the parameters for the

neural network used in this thesis a so called back-propagation algorithm has been used, as implemented in the JETNET package [98].

The Neural Net Input Variables

For this analysis a neural network with three layers has been chosen. The input variables that were chosen are listed below, and a plot with data and Monte Carlo expectations for the variables that were not yet shown can be found in Figure 5.5. Note that for the calculation of x_k the input variables have, where necessary, been rescaled to fall in the range $[0, 1]$.

- Sphericity. As described in Chapter 4, this event shape variable characterizes how spherical the event is. The background, mainly two jet events, can clearly be seen to peak at low values, while the signal events, with at least four jets, are more spherical.

- $m_{\mathrm{W}1} - m_{\mathrm{W}2}$, the difference of the two W masses as calculated after a four-constraints fit, as explained in Chapter 4. Note that the most energetic jet is by definition included in the first W, which explains why the distribution is not symmetric around zero. The asymmetry is larger for the background, as the energy of the most energetic jet is usually higher for the background (see Figure 5.5d).

- $\min(E_{\mathrm{jet}})$. The main background essentially has a two-jet topology, but has been reconstructed assuming that there are four jets. This often results in two jets reflecting the original two jets, which have most of the energy, and two lower energy jets due to misreconstruction or a hard fragmentation. The energy of the least energetic jet is therefore in general lower for the background than for the signal. The energies are those calculated after a four-constraints fit.

- $\max(E_{\mathrm{jet}})$. For similar reasons as for the least energetic jet, the energy of the most energetic jet is a variable with a good separating power between signal and background and is thus used as an input variable for the neural net.

- $\min(\theta_{\mathrm{jet-jet}})$. The fourth jet in a background event will often be a gluon jet. As an emitted gluon typically has a low angle with respect to the original quark the minimum angle between two jets in the event will generally be smaller for background events.

- $m_{\mathrm{hemisphere}}$. In this case, the event is reconstructed under the assumption that it is a two-jet event and consequently the clusters are grouped into two jets. If the assumption is correct the event should have two narrow, low mass jets, while for a signal event the four jet structure of the event will result in two broad, high mass jets. The average of the two jet masses is therefore a good discriminating variable. This average mass can be interpreted as the average hemisphere mass.

- $\log(y_{34})$. As can be seen in Figure 5.2, the jet resolution parameter y_{34} provides a good separation between signal and background.

Most input variables exploit the difference between the true four jet topology of the signal and the underlying two jet structure of most background. The only exception to this is the mass difference of the two assumed W bosons. For this reason it is understandable that the neural network will not be able to distinguish ZZ events from W^+W^- events if both Z^0's decay to quarks: the event has a true four jet structure, and both reconstructed bosons have, within the experimental resolution, the same mass. As in any case, up to $\sqrt{s} = 189$ GeV, the $q\bar{q}$ background is dominant, no attempt has been made to improve on this situation.

Note that the sum of the reconstructed masses has not been used as a neural net input variable. Although this would have added some separating power between W^+W^- events and ZZ events as well as two jet background the resulting gain is relatively small. At the same time the selection would have become explicitly dependent on the W mass. This could lead to an undesired systematic error for the cross section measurement as well as complications when the W mass will be fitted using the selected events.

5.3.1 Training the Neural Network

As mentioned above, the neural net used for the final event selection is a three layer neural network as described by equation 5.1, where the desired output is one for signal events and zero for background events. As the training is focused on the dominant two jet background, the training sample consists of a mixture of background $e^+e^- \rightarrow q\bar{q}$ and signal $e^+e^- \rightarrow W^+W^- \rightarrow q\bar{q}q\bar{q}$ Monte Carlo events. A total of 3×10^6 $q\bar{q}$ and 1.3×10^5 signal events are available. Only half of these events have been used in the training of the neural network. This is necessary to be able to test the so called *generalization performance* of the neural net: the ability to distinguish signal and background on an independent sample, i.e. a sample that has not been used in he training. The importance of this generalization performance can be understood by looking at the large number of free parameters in formula 5.1: a neural network with seven input nodes and ten nodes in the hidden layer has a total of 91 free parameters to be determined. Especially with a small training sample, or a training sample containing only a small number of events that are difficult to classify, the risk exists that the network focuses on accidental features of the training patterns. As this so called overlearning could lead to an overly optimistic estimate of the performance, it is important to determine efficiencies and purities from an independent sample.

The training is performed in an iterative procedure in which the total training sample is used many times by the package performing the minimization, in this case JETNET. The number of cycles through the training sample is called the number of epochs. During the training the performance of the neural net can be monitored. Here the performance is characterized by $\sqrt{\epsilon\pi}$, the square root of the final selection efficiency ϵ for signal events times

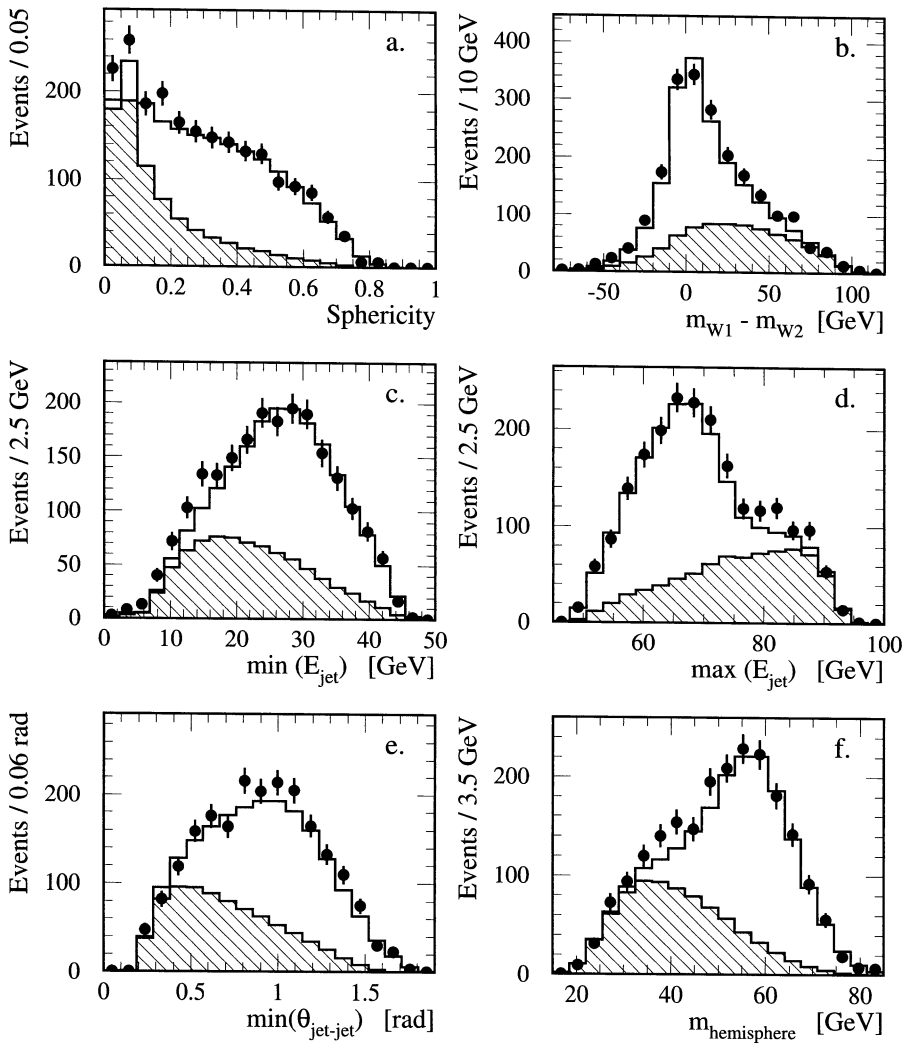

Figure 5.5: *The data collected at* $\sqrt{s} = 189$ GeV *and corresponding Monte Carlo expectations for variables used as input for the neural network. All cuts have been applied. The dots denote the data, the open histogram represents the total Monte Carlo expectation and the hatched histogram the sum of the background Monte Carlo expectations. Shown are respectively the sphericity (a), mass difference between the two reconstructed* W *masses (b), energy of the least energetic jet (c), energy of the most energetic jet (d), minimum angle between two jets (e) and the average mass of the two jets if the event is forced into two jets (f).*

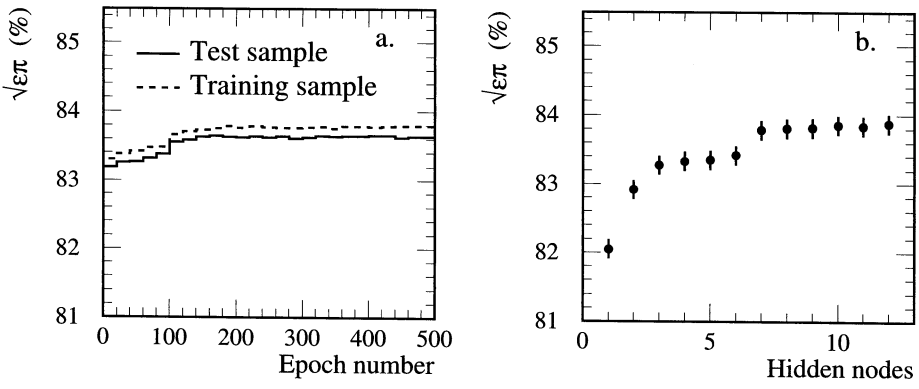

Figure 5.6: *Neural net performance as a function of the number of epochs the network has been trained (a) and as a function of the number of hidden nodes (b). The error bars on the right picture are due to finite Monte Carlo statistics, and are correlated as the same Monte Carlo samples have been used to determine the performance for each number of hidden nodes.*

the fraction of all selected events that are signal events, the purity π. As this number is, in good approximation, inversely proportional to the expected statistical error of a cross section measurement, it is a convenient way to express the performance in a single number. An example of the performance of the neural network used for this analysis as a function of the epoch number is shown in Figure 5.6a. The performance of the training and of the testing sample are both shown. At first, the performance of both samples improves with the epoch number: the network is being trained. Then the performance can be seen to stabilize when the optimal configuration has been found. Also, it is clear that the training sample is large enough to prevent overlearning: the performance of the training and testing sample is, within the statistical precision, identical.

In Figure 5.6b the final performance, after sufficient training, is plotted as a function of the number of hidden nodes. As it is clear that adding more than seven hidden nodes is no longer useful, the number of hidden nodes for the net used in the analysis has been fixed at seven.

5.4 Results and Cross Section Determination

The most straightforward way to determine the signal cross section would be to cut on the neural net output nn_{out}. However, this way not all available information is exploited: events

with a neural net output close to one have a much higher purity than events that just pass the cut, and should therefore get more weight in the determination of the W^+W^- cross section to obtain a better statistical sensitivity. The method chosen is to perform a fit to the full neural net output spectrum, i.e. to determine for which value of the signal cross section the predicted neural net output spectrum agrees best with the data. The exact procedure followed is described in [99, 100] and summarized below.

5.4.1 Fitting Method

First the shape of the neural net output is determined for the signal and various backgrounds. For this purpose, the neural net output spectrum is divided in N_b bins, giving d_i data events per bin i. For the signal and background Monte Carlos sample the number of events per bin is a_{ji} for Monte Carlo sample j. As the total luminosity L and the selection efficiency ϵ_j are known, the expected number of events n_i in each bin can be calculated using

$$n_i = \sum_{j=1}^{N_{\mathrm{MC}}} \mathrm{L}\epsilon_j\sigma_j\frac{a_{ji}}{s_j}, \tag{5.2}$$

where the sum extends over the number of Monte Carlo samples N_{MC}, and σ_j is the cross section of the corresponding process j. Here s_j is the sum of the events in Monte Carlo sample j, i.e. $s_j = \sum_{i=1}^{N_b} a_{ji}$. The probability $P(d_i)$ to measure d_i events when n_i events are expected is given by Poisson statistics:

$$P(d_i) = e^{-n_i}\frac{n_i^{d_i}}{d_i!}. \tag{5.3}$$

Using equation 5.3 and omitting the constant factorials, the log likelihood $\mathcal{L}$ can be written as

$$\log\mathcal{L} = \sum_{i=1}^{N_b}(d_i\log n_i - n_i). \tag{5.4}$$

As the n_i are a linear sum of the cross sections σ_j of the various Monte Carlo processes one wants to measure, the cross sections can be obtained by maximizing the likelihood of equation 5.4 with respect to the σ_j, thus performing a standard binned log likelihood fit. The errors on the cross sections can as usual be found by looking at the contour $|\mathcal{L}(\sigma_i) - \mathcal{L}_{max}| = 0.5$, where $\mathcal{L}_{max}$ is the value of the likelihood evaluated at the point where it is maximal. This explains why the logarithm of $d_i!$ can be left out of equation 5.4, as this term does not depend on the cross sections one wants to measure it will not influence the shape of the likelihood curve.

As the maximization cannot be performed analytically, a numerical procedure has to be followed. Often the MINUIT package [96] is used, giving fast and reliable estimates for the cross sections that are to be determined and their errors.

However, a drawback of the use of likelihood 5.4 is that it implicitly assumes that the Monte Carlo samples used are of infinite size, as otherwise the statistical fluctuations on the ratio a_{ji}/s_j need to be taken into account. Since the size of the Monte Carlo samples actually used are too small to justify this assumption, the method has to be modified. This can be achieved by observing that the numbers a_{ji} are nothing else but stochastic variables, depending on the expected number of Monte Carlo events in a particular bin. It is this, unknown, number of expected events A_{ji} that should be used in formula 5.2:

$$N_i = \sum_j \mathrm{L}\epsilon_j\sigma_j\frac{A_{ji}}{S_j}, \tag{5.5}$$

with $S_j = \sum_{i=1}^{N_b} A_{ji}$. If $A_{ji} << S_j$ it can be assumed safely that the a_{ji} are generated from a Poisson distribution with mean A_{ji}. The improved log likelihood, again leaving out the constant factorials, can then be written as

$$\log\mathcal{L} = \sum_{i=1}^{N_b}(d_i\log N_i - N_i) + \sum_{i=1}^{N_b}\sum_{j=1}^{N_{\mathrm{MC}}}(a_{ji}\log A_{ji} - A_{ji}). \tag{5.6}$$

This likelihood now depends not only on the cross sections σ_j, but also on the A_{ji}. This means that to obtain values for the cross sections, the likelihood 5.6 has to be maximized with respect to $N_{\mathrm{MC}}\cdot(N_b+1)$ unknowns. This is obviously a more complicated task as the just N_{MC}-dimensional maximization necessary when using the likelihood from formula 5.4. As it turns out, however, the problem can be simplified considerably [99]. When a numerical maximization with respect to the N_{MC} cross sections σ_j is performed, for which one can again use the MINUIT package, the values for A_{ji} that maximize equation 5.6 for a given set of σ_j can quickly be found. This can be seen by taking the derivative of equation 5.6 with respect to the A_{ji} and setting all derivatives to zero, giving $N_{\mathrm{MC}}\cdot N_b$ equations. When substituting

$$x_i = 1 - \frac{d_i}{N_i} \tag{5.7}$$

this gives the equations

$$A_{ji} = \frac{a_{ji}}{1+\mathrm{L}\epsilon_j\sigma_j a_{ji}S_j^{-1}x_i} \qquad \forall i,j. \tag{5.8}$$

This is a considerable simplification as the $N_{\mathrm{MC}}\cdot N_b$ unknowns A_{ji} can be calculated from just N_b unknowns x_i. The x_i can be calculated by combining the equations 5.5, 5.7 and 5.8 to form

$$\frac{d_i}{1-x_i} = \sum_{j=1}^{N_{\mathrm{MC}}}\frac{\mathrm{L}\epsilon_j\sigma_j S_j^{-1}a_{ji}^2}{1+\mathrm{L}\epsilon_j\sigma_j S_j^{-1}a_{ji}x_i} \qquad \forall i. \tag{5.9}$$

As the equations 5.9 are just N_b uncoupled equations which can easily be solved numerically, values for the x_i can be found, which in turn give values for all A_{ji} using equation 5.8.

This method has been implemented in the HBOOK package [100], which is the package used for this analysis.

5.4.2 Results

For this analysis the backgrounds taken into account are, as mentioned before, the $q\bar{q}$ background, the ZZ background, the background from W^+W^- events decaying to different final states and the two photon events. For the last three background sources, the values for the cross sections are not determined from the data but are fixed at their Standard Model expectation values. For the largest, $q\bar{q}$, background, this is not done: it is determined simultaneously with the signal cross section from the neural net output spectrum. This is done as it is known from LEP1 that the number of four jet events predicted by the $q\bar{q}$ Monte Carlo is not in satisfactory agreement with the number observed in the data. By leaving the $q\bar{q}$ cross section free in the analysis, the dependence on the four jet cross section is diminished.

The results of the fits with the statistical errors are given in Table 5.2. For comparison the Standard Model expectation values are listed for the $q\bar{q}$ background.

Energy	**Process**	**Cross Section**	
		Measured	**Standard Model**
$\sqrt{s} = 161$ GeV	$q\bar{q}q\bar{q}$ signal	$0.98^{+0.51}_{-0.40}$ pb	
	$q\bar{q}$ background	142^{+19}_{-18} pb	147 pb
$\sqrt{s} = 172$ GeV	$q\bar{q}q\bar{q}$ signal	$5.48^{+0.92}_{-0.85}$ pb	
	$q\bar{q}$ background	128^{+18}_{-17} pb	121 pb
$\sqrt{s} = 183$ GeV	$q\bar{q}q\bar{q}$ signal	8.35 ± 0.46 pb	
	$q\bar{q}$ background	105 ± 6 pb	107 pb
$\sqrt{s} = 189$ GeV	$q\bar{q}q\bar{q}$ signal	7.40 ± 0.26 pb	
	$q\bar{q}$ background	112 ± 5 pb	98 pb

Table 5.2: *Cross sections obtained by the fit for signal and $q\bar{q}$ background and their statistical error, for the data taken at $\sqrt{s} = 161 - 189$ GeV. For the background the Standard Model expectation value is also given. The statistical error includes the uncertainty due to finite Monte Carlo statistics.*

The neural net output plots for the various energies are shown in Figure 5.7. In this plot the signal and $q\bar{q}$ Monte Carlo have been scaled using the measured cross sections. Event displays of two selected (i.e. high neural network output) events are shown as an example in Figure 5.8.

5.5 Systematic Error Analysis

A common way of evaluating systematic errors is by varying the cuts within limits thought to be "reasonable" and assigning any change in the obtained cross-section to the systematic

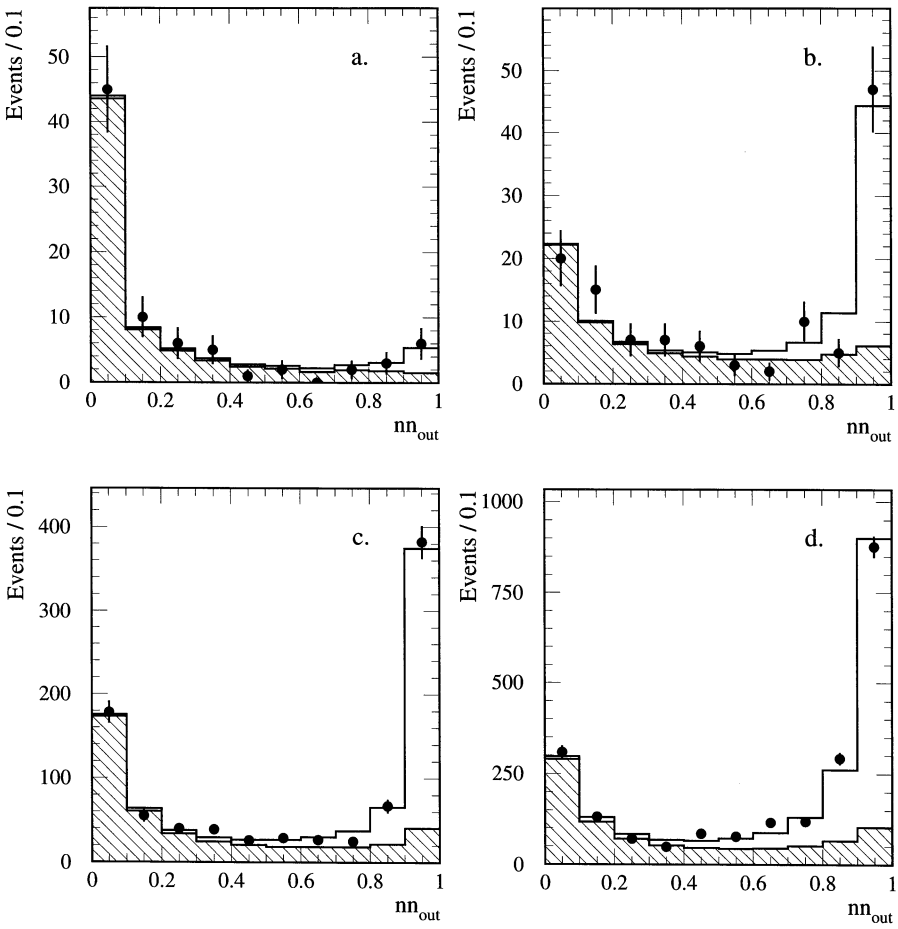

Figure 5.7: *Neural net output nn_{out} for the data collected at $\sqrt{s} = 161$ GeV (a), $\sqrt{s} = 172$ GeV (b), $\sqrt{s} = 183$ GeV (c) and $\sqrt{s} = 189$ GeV (d) . All cuts have been applied. The dots denote the data, the open histogram represents the total Monte Carlo expectation and the hatched histogram represents the sum of the background Monte Carlo expectations. The signal and $q\bar{q}$ Monte Carlo are scaled according to the cross sections derived from the fit to the measured neural net output spectrum.*

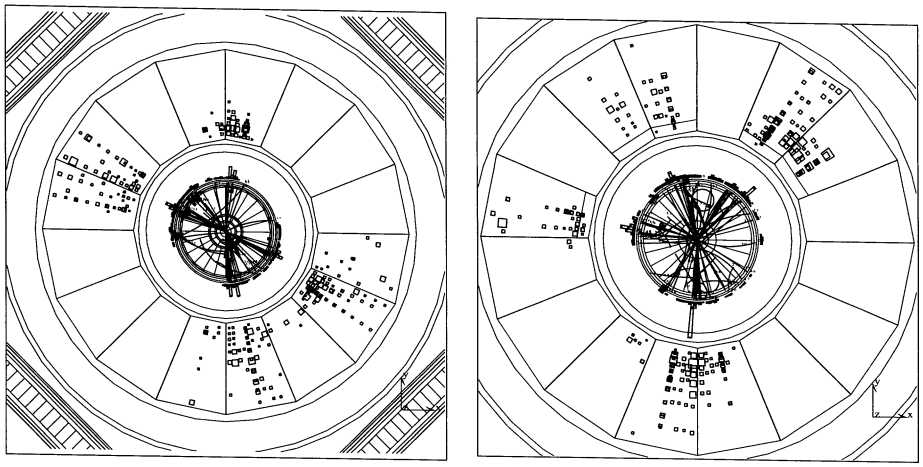

Figure 5.8: *Event displays of two selected four-jet events at* $\sqrt{s} = 189$ GeV, *as an example of two typical events. Both events have a high value of the neural network output and are thus likely to be WW events.*

error. This approach is ill-suited for an analysis where a single cause for a possible systematic error (like detector miscalibration or Monte Carlo imperfection) can affect several variables used in the analysis. In that case, varying these variables individually does not lead to a meaningful estimate of the systematic error. Also, using this method the accuracy with which the systematic error can be determined is dependent on the amount of data available. Especially in case of limited data statistics such a systematic error estimate would be unreliable.

The approach adopted here is to investigate possible uncertainties in the Monte Carlo modeling. For each possible effect, a new Monte Carlo sample is obtained with modeling parameters varied within the uncertainty. The analysis is redone using this Monte Carlo sample instead of the original sample, and a possible difference in the end result is used as an estimate of the systematic error due to this effect. This procedure ensures that the error is evaluated correctly even if an effect influences several analysis variables, and is independent of the data statistics. Below the possible effects that have been studied are listed. The total systematic error is obtained by summing up the individual error estimates in quadrature.

5.5.1 Modeling of the Detector Response

Systematic errors due to possibly incorrect modeling of the detector are described here. For this, the existing Monte Carlo samples have been re-reconstructed using different assump-

tions about the detector response, as described below.

HCAL Energy Calibration

The distribution of the energy deposited in the HCAL is shown for data and the Monte Carlo expectations in Figure 5.9a. The average energy deposit agrees between data and Monte Carlo up to $1.6 \pm 0.6\%$ on the selected event sample. During the re-reconstruction of all Monte Carlo samples used, all HCAL energies were changed by 2% to determine a possible error on the W^+W^- cros-section. The result of the fit changed by 0.7%, which was taken as the systematic error due to the HCAL energy scale.

ECAL Energy Calibration

The total energy deposition in the electromagnetic calorimeters is shown in Figure 5.9b. The difference between the average energy deposit in the data and the Monte Carlo expectation is 0.0 ± 0.5 %. To estimate a possible systematic error due to miscalibration of the ECAL, the Monte Carlo samples were re-reconstructed after changing all BGO energies by 1% and SPACAL energies by 5%. The resulting change in the measured W^+W^- cross-section was found to be 0.3%.

Jet Angular Resolution

To study the effect of possible mismatch between jet angular resolutions in data and Monte Carlo, the measured jet directions in the Monte Carlo have been changed by 0.5° in a random direction. As this is approximately equal to the angular resolution, this change is considered to be conservative. The systematic error assigned due to this effect is 0.1%. The jet angular resolutions have been studied on two-jet events selected from data and Monte Carlo by comparing the acolinearity and acoplanarity distributions.

Cluster Simulation

The multiplicity distribution, as shown in Figure 5.2c, has traditionally been a difficult variable to model in the Monte Carlo simulation. The multiplicity has therefore not been used as an input variable for the neural network. Also, the selection cut on the total number of clusters is made at an especially low value. The events just passing the cut will then be mostly obvious background events that can be recognized by the neural network, thus limiting the sensitivity to the multiplicity distribution.

The mean of the Monte Carlo and data multiplicity distributions agree within the statistical precision when counting the multiplicity of clusters with at least 300 MeV. For clusters with more than 100 MeV, however, the difference is about four clusters. As this reflects imperfect Monte Carlo simulation, the systematic error has been evaluated by shifting the

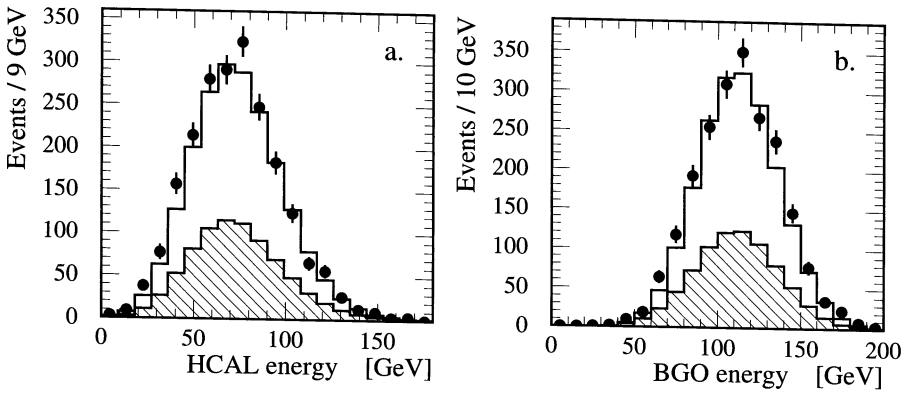

Figure 5.9: *Total energy deposit in the hadronic calorimeters (a) and in the electromagnetic calorimeters (b). The dots denote the data, the open histogram represents the total Monte Carlo expectation and the hatched histogram represents the sum of the background Monte Carlo expectations.*

Monte Carlo multiplicity distribution by a conservative amount of three clusters. After this the analysis has been redone. The change in the measured cross section is found to be negligible.

g-factors

As described in Section 4.3, the g-factors compensate for part of the discrepancies between the data and the Monte Carlo. However, there is no unique way of doing this, and some differences will remain. To determine the influence of this the Monte Carlo and data have been reconstructed using a set of g-factors determined in a different way, as explained in Section 4.3 [85], instead of using the g-factors used for the rest of this analysis. The resulting W^+W^- cross section differs by 1.2%. The effects of incorrect detector modeling in the Monte Carlo, which have already been estimated above, will again contribute to this shift. For this reason, only half of the shift has been assigned as a systematic error.

5.5.2 Luminosity Determination

The luminosity used in the analysis has been measured using Bhabha events, as described in Section 3.2. The experimental systematic uncertainties originate from the event selection criteria, 0.10% and from the limited knowledge of the detector geometry, 0.05%. The limited Monte Carlo statistics results in an uncertainty of 0.07%, yielding a total experimental

systematic uncertainty of 0.13%. In addition, a theoretical uncertainty of 0.12% is assigned, originating from the uncertainty in the calculations of the Bhabha cross section[101]. The total error on the luminosity results in 0.18%[102]. As an uncertainty on the luminosity translates directly to an identical uncertainty on the measured cross section, a 0.2% systematic error has been assigned.

5.5.3 Modeling of the W^+W^- Signal

Apart from imperfections in the modeling of the detector response, systematic errors can also arise from an imperfect simulation of the W^+W^- signal in the Monte Carlo. Below the main uncertainties from this source are described.

W Mass and Width

Ideally, one would like to measure the W^+W^- cross section without making any assumptions about the W mass and width. Unfortunately, one needs to choose values for the W mass and width in order to be able to produce the necessary W^+W^- Monte Carlo events. In order to evaluate the dependence of the measured cross section on these parameters, several signal Monte Carlo samples have been generated. For each sample a different value for the W mass and/or width has been used. In Figure 5.10 the cross sections measured using these samples are compared to the one obtained using the standard Monte Carlo, where a W mass and width of 80.5 GeV and 2.11 GeV have been used, respectively. As can be seen, there is no significant dependence on either the W mass or width. Conservatively, a 0.3% systematic error has been assigned, as a smaller effect could not have been observed due to finite Monte Carlo statistics.

Four-fermion versus CC03 Monte Carlo

The KORALW Monte Carlo events used in this analysis were generated with only the CC03 diagrams switched on, whereas actually many more diagrams contribute to the $q\bar{q}q\bar{q}$ final state at LEP2, as explained in Section 2.2. Some of these final states can only be generated by ZZ-like (NC) diagrams; in this analysis these have been treated as background since we are only interested in the CC03 WW cross section. Nevertheless, the CC03 diagrams are in principle not enough to describe non-ZZ $q\bar{q}q\bar{q}$ final states; in addition there is interference between the CC and NC diagrams for those final states that can be created by both types of diagrams, like $u\bar{d}u\bar{d}$. Fortunately, these effects are small for events without an electron or positron in the final state. In this thesis, the four-fermion effects are estimated by repeating the analysis by reweighting each $q\bar{q}q\bar{q}$ Monte Carlo event with a weight w_i calculated as:

$$w_i = \frac{\mathcal{M}^2_{i,4f-\mathrm{ZZ}}}{\mathcal{M}^2_{i,\mathrm{CC03}}}, \tag{5.10}$$

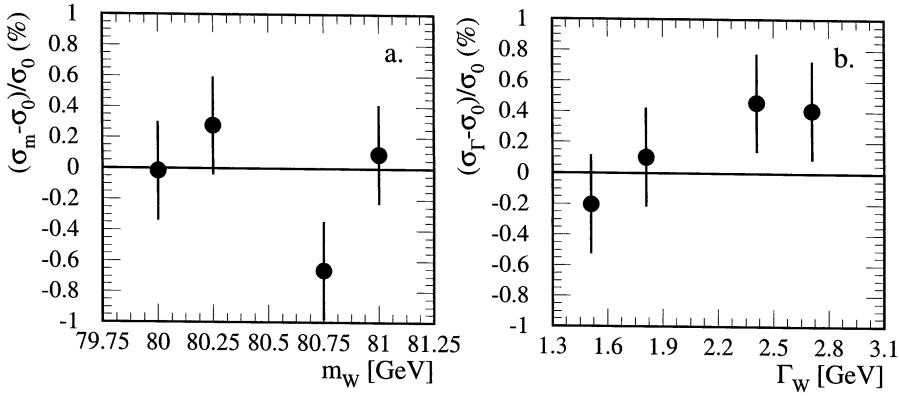

Figure 5.10: *Shift in measured cross sections when Monte Carlo samples generated with different values for the* W *mass (a) and width (b) are used in the analysis. The errors are due to finite Monte Carlo statistics. When the* W *mass has been varied, the* W *width has been fixed at the Standard Model value. For the variation of the* W *width, a mass of 80.5* GeV *has been used.*

where $\mathcal{M}_{i,4f-ZZ}$ is the matrix element for event i taking into account all four-fermion diagrams except the ZZ-production diagrams, and $\mathcal{M}_{i,CC03}$ is the matrix element for event i taking into account the CC03 diagrams only. The resulting difference in cross section of 0.4% is taken as a systematic error.

ISR/FSR Simulation in W^+W^- Events

The uncertainties related to the simulation of ISR and FSR in W^+W^- events are estimated with the YFSWW3 Monte Carlo [34]. The difference in resulting $W^+W^- \rightarrow q\bar{q}q\bar{q}$ cross section between YFSWW3 and KORALW is $+0.03 \pm 0.4\%$. Since the actual theoretical uncertainty on the ISR/FSR simulation is larger than simply the YFSWW3-KORALW difference, a systematic uncertainty of 0.4% will be assigned. Removing ISR and FSR photons from the event and repeating the analysis gives consistent results.

Fragmentation

The uncertainties on the cross section measurement due to fragmentation are estimated by exchanging the standard baseline Monte Carlo using JETSET for baseline Monte Carlo's using ARIADNE or HERWIG, or by variation of the JETSET parameters around their tuned values. The tuning of these programs is described in Section 3.3.1.

With ARIADNE, a change in cross section of 0.1% is observed. When HERWIG is used, the change is 3.1%. As described in Section 3.3.1, however, HERWIG does a significantly worse job in describing the Z data, even after tuning.

As an alternative to comparing different models, within the JETSET model the tuned parameters $\Lambda_{\rm LLA}$, b and $\sigma_{\rm q}$ were varied within their errors resulting from their tuning [46]. This was done for all three parameters with a fast detector simulation [103], and for Λ, which gave the largest effect, with full Monte Carlo simulation as well. The three JETSET parameters were varied by ± 2 and ± 3 standard deviations; one standard deviation equals 34 MeV for Λ, 34 MeV for $\sigma_{\rm q}$, and 0.12 GeV^{-2} for b. Changes in cross section of 0.17%, 0.04% and 0.16% respectively were observed for each one standard deviation change of JETSET parameter. The parameter Λ was also varied in a full simulation Monte Carlo sample, resulting in a 0.4% change in cross section per standard deviation change of Λ.

The results above indicate fairly small effects, with the exception of HERWIG. Taking into account HERWIG's deficiencies (see Section 3.3.1) we do not quote the full effects observed with this generator as a systematic uncertainty. Instead, we assign a systematic error on the $\rm W^+W^- \rightarrow q\bar{q}q\bar{q}$ cross section due to fragmentation uncertainties of 0.1 pb, which translates to 1.3%. This is significantly larger than the variations seen with ARIADNE or JETSET; and covers 40% of the variation seen with HERWIG.

Bose-Einstein Correlations

Correlations between identical bosons, so called Bose-Einstein correlations, affect the fragmentation of the $\rm W^+W^-$ decay products. As has been described in section 2.5.3, several ways have been suggested to incorporate these correlations in the fragmentation model. Unfortunately it is up to now not possible to determine, using the data, whether any of these models describes the final state topology with satisfactory precision. For the standard Monte Carlo events, the LUBOEI variants $\rm BE_{32}$ and $\rm BE_0$ as implemented in the PYTHIA 6.1 package have been used [104]. In this routine, particles (to be more precise: bosons in the final state, such as pions) are reshuffled such as to reproduce phenomenologically the two-particle enhancement at low Q for like-sign particles. Both models have two free parameters corresponding to the correlation strength and the source radius; these parameters have been tuned by L3 to be: PARJ(92) $= 1.5$ and PARJ(93) $= 0.33$ GeV for $\rm BE_0$, and PARJ(92) $= 1.68$ and PARJ(93) $= 0.38$ GeV for $\rm BE_{32}$ [81].

In the Monte Carlo used for the quoted result, only correlations between final state bosons originating from the same W have been allowed. Alternatively, one can use the same model but allow correlations between all bosons, regardless of their original W parent. In this case, the measured cross section changes by -0.25%, both for $\rm BE_{32}$ and $\rm BE_0$.

To study an extreme situation, one can also use JETSET without taking into account any BE correlations at all. In this case, the fragmentation model has been changed significantly, and JETSET parameters have been retuned [80]. With this model, a change of +0.15% in the

cross section is observed.

Bose-Einstein correlations in WW events have been studied by L3 in a dedicated study with data taken at $\sqrt{s} = 189$ GeV [49], as well as at higher energies [105, 50]. The conclusions from these studies are that correlations are observed within the same W with a strength compatible with those observed in light-quark Z decays, but that correlations between different W's are not observed in the data, and that their implementation in BE_{32} and BE_0 is excluded, by more than 4 standard deviations. In fact, similar studies of all four experiments are now consistent and observe no signs of correlations between different W's [105].

At first look, the absence of inter-W Bose-Einstein correlations seems surprising. However, models of Bose-Einstein correlations have been constructed in the framework of the Lund model [51, 52]. In these models, Bose-Einstein correlations follow as a coherent effect related to the symmetrization of particle production from the Lund string. In fact these models reproduce Bose-Einstein correlations results measured in LEP1 data, but intrinsically predict no Bose-Einstein correlations between different W's, as these decay into different strings, unless color reconnection takes place. In addition there could be incoherent Bose-Einstein correlations, corresponding to the original Hanbury-Brown-Twiss (HBT) effect [106], but these typically have large length scales, corresponding to small R, and thus only small effects on inter-W correlations at LEP2. Further theoretical discussion can be found in Reference [50]. Other models of Bose-Einstein correlations, based on global event reweighting techniques, all predict that inter-W correlations give only very small observable effects, in agreement with our data [53, 54].

Given the results of the experimental studies of BEC in WW events, a systematic error of 0.1% is assigned on the $W^+W^- \rightarrow q\bar{q}q\bar{q}$ cross section due to Bose-Einstein correlations.

Color Reconnection

As has been described in Section 2.5.4, it is unclear how a possible color rearrangement during the fragmentation of the four-quark system should be described. In the Monte Carlo used to obtain the cross section it is assumed that no such color reconnections takes place. To investigate the dependence of the analysis on this assumption, several models with different treatment of color reconnection have been studied, and Monte Carlo events have been generated for each model. In Table 5.3, the changes in the measured cross section is shown. A longer description of each model can be found in Section 2.5.4. Due to an error in the color reconnection model of HERWIG 5.9, this model is not used. Where it has been used, effects were consistent with zero.

The $W^+W^- \rightarrow q\bar{q}q\bar{q}$ data has also been used to directly search for effects of color reconnection [60]. The most sensitive way to study color reconnection has been found to compare the energy and particle flow between jets from the same W, and between jets from different W's. These studies show a good sensitivity to the predictions of the SK I model, and the $W^+W^- \rightarrow q\bar{q}q\bar{q}$ data excludes very large reconnection probability but is not inconsistent

Model	Cross section shift (%)
PYTHIA SK I	0.2
PYTHIA SK II	0.3
PYTHIA SK II'	0.4
ARIADNE 1	-0.16
ARIADNE 2	0.09

Table 5.3: *Shift in measured cross section when using Monte Carlo samples generated using different assumptions regarding color reconnection. All models are briefly described in Section 2.5.4.*

with the 30% of reconnected events predicted by the authors of the SK models, nor with zero. Similar conclusions are reached when studying the charged particle multiplicity in $q\bar{q}q\bar{q}$ and $q\bar{q}\ell\nu$ events.

The largest of the observed shifts, 0.4%, is assigned as a systematic error on the $W^+W^- \rightarrow q\bar{q}q\bar{q}$ cross section due to color reconnection uncertainties.

5.5.4 Modeling of the Backgrounds

In this section the systematic errors arising from a possible misdescription of the backgrounds are discussed.

Four-jet Description in $q\bar{q}$

For the dominating background, $e^+e^- \rightarrow q\bar{q}$, the total cross section known from the Standard Model has not been used in the determination of the signal cross section. Instead, the background cross section has been fitted to the neural network output distribution. This is done as the measured number of multi-jet events in the $q\bar{q}$ data is not described satisfactorily by the Monte Carlo model [46]. Although the vulnerability to this problem is diminished by leaving the *cross section* of preselected $e^+e^- \rightarrow q\bar{q}$ events free, it is still quite possible for the *shape* of the neural net output spectrum to be influenced. In order to investigate this, a relatively high statistics data sample at $\sqrt{s} = m_Z$ has been studied. As a function of y_{34}, the ratio of measured and expected events has been determined. For events with a high value for y_{34}, indicating a multi-jet topology, an excess in the data is found. Assuming this effect is similar at higher energy, the background Monte Carlo has been reweighted using the ratio described above. As events with a higher y_{34} typically have a higher neural net output, the output shape obtained via reweighting has a larger number of events in the signal region. The ratio of the two spectra is shown in Figure 5.11. As expected, the ratio increases with increasing neural net output. Using the reweighted distribution yields a shift of -1.6% on the cross section.

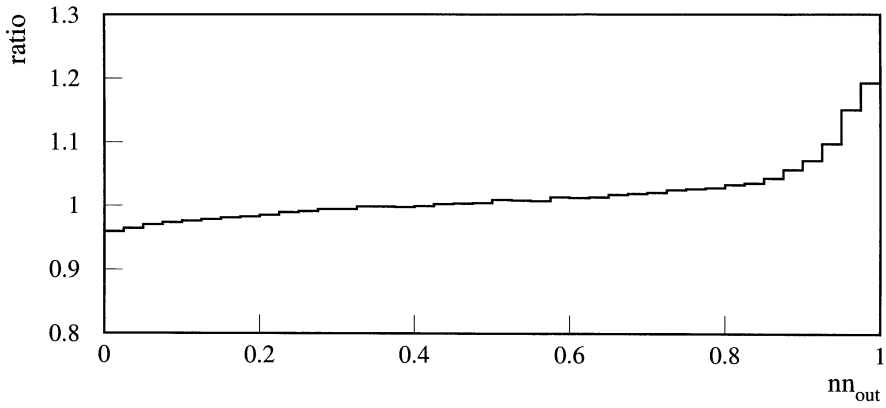

Figure 5.11: *The ratio of the reweighted neural net output spectrum and the one used to obtain the central cross section value. The normalization is such that the average weight of a* $q\bar{q}$ *Monte Carlo event is one.*

This shift has been applied to the result, half of the shift is assigned as systematic error due to uncertainties in the QCD four-jet simulation.

ISR Simulation in $q\bar{q}$

The Monte Carlo generator used for the production of the $q\bar{q}$ background is PYTHIA [41]. This multi-purpose generator does not describe the hard part of the initial state spectrum up to the desired precision, as it generates too many photons with high transverse momentum. This can be seen in Figure 5.12, where the energy of the most energetic bump has been shown. The events selected for this plot are required to pass all cuts described in Section 5.2 except the ones designed specifically to reject high energy photons measured in the detector. The peak of detected high energy photons is clearly visible, in both data and Monte Carlo. The Monte Carlo predictions are overestimating the data by approximately 20%. It is expected that this is not a serious problem, as those events are easy to reject. This hypothesis has been checked by reweighting all $q\bar{q}$ Monte Carlo such that events with an ISR photon with an angle to both initial leptons of at least ten degrees and more than ten GeV of energy get a 20% lower weight. In this case, the fitted W^+W^- cross section changes by 0.2%. This shift has been applied to the result, half of the shift is assigned as systematic error due to uncertainties in the ISR simulation of the background.

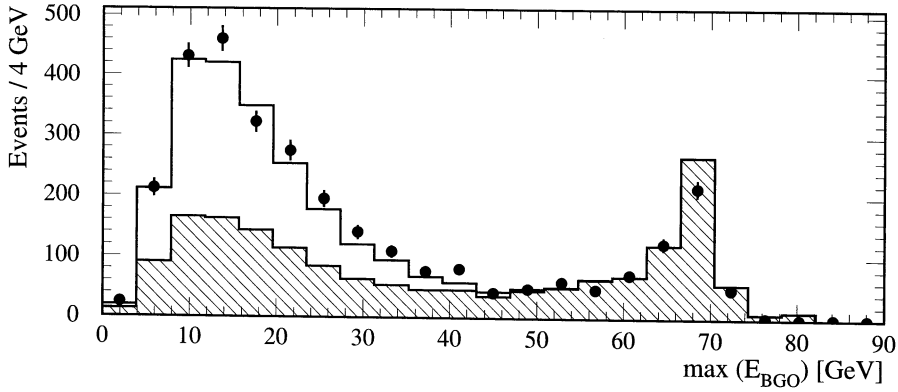

Figure 5.12: *Maximum energy deposition in the BGO part of the ECAL. Cuts have been applied to select high energy, balanced, high multiplicity events but no effort has been made to reject events where a high energy photon has been detected.*

ZZ Background Scale

In the cross section determination, the background from ZZ events is taken into account by fixing the expected number of events from this source to the Standard Model expectation value, which can be can be calculated with a 2% precision, and has been measured with about 20% precision [107, 108]. To obtain a systematic error estimate, the ZZ background estimate has been varied by the theoretical precision, giving a 0.1% uncertainty.

WW Non-four-quark Background Scale

For the background from W^+W^- events decaying to other final states than $q\bar{q}q\bar{q}$, the Standard Model cross section for these processes have been used in the fit. In this case the cross sections have been varied by $\pm 50\%$, giving a 0.2% error on the measured signal cross section. As such a large variation of the background cross section results in a change in the measured signal cross section that is small compared to the other systematic errors and the statistical error, it is in the remainder of this analysis assumed that the cross section for $e^+e^- \rightarrow W^+W^- \rightarrow q\bar{q}q\bar{q}$ decaying to four jets is measured independent of the cross sections for other W^+W^- decay chains.

Error source	Systematic error (%)
HCAL Energy Scale	0.7
ECAL Energy Scale	0.3
Jet Angular Resolution	0.1
Cluster Simulation	0.1
g-Factors	0.6
Luminosity Measurement	0.2
Fragmentation	1.3
WMass/Width Dependence	0.3
Misdescription of ISR/FSR in Signal	0.4
4-Fermion vs CC03 Effects	0.4
Color Reconnection	0.4
Bose-Einstein Correlations	0.1
y_{34} Reweighting of $q\bar{q}$ Monte Carlo	0.8
Misdescription of ISR in $q\bar{q}$ Monte Carlo	0.1
ZZ Cross Section	0.1
W^+W^- Background Cross Section	0.2
Total	**2.0**

Table 5.4: *Summary of the contributions to the systematic error on the cross section measurement at* $\sqrt{s} = 189$ GeV.

5.5.5 Systematic Error Summary

The systematic error estimates from all sources considered have been summarized in Table 5.4, and add up to a total systematic error of 2.0%. The measured cross section for the process $e^+e^- \rightarrow W^+W^- \rightarrow q\bar{q}q\bar{q}$ at $\sqrt{s} = 189$ GeV then becomes $7.40 \pm 0.26\,(\text{stat}) \pm 0.15\,(\text{syst})$ pb.

The results of the $W^+W^- \rightarrow q\bar{q}q\bar{q}$ cross section measurements between $\sqrt{s} = 161$ and $\sqrt{s} = 189$ GeV, as presented in this thesis, are plotted graphically in Figure 5.13. Systematic errors on the $W^+W^- \rightarrow q\bar{q}q\bar{q}$ cross section at 161, 172 and 183 GeV were estimated in the same way as for the 189 GeV sample. Due to the fact that these samples are smaller, many systematic errors can be determined with less precision, and are conservatively assigned larger values: 5% at 161 GeV, 3.1% at 172 GeV, and 2.8% at 183 GeV. Figure 5.13 also shows the Standard Model prediction, the theoretical expectation if the WWZ vertex would not exist, and the theoretical prediction if only the neutrino exchange diagram existed. These

latter two predictions disagree with the data, whereas the Standard Model prediction agrees well with the data.

5.6 W Mass from WW Cross Section

Around threshold, $\sqrt{s} \approx 2m_{\mathrm{W}}$, the WW production cross section is sensitive to the W mass. Therefore, the measured WW production cross section can be transformed into a measurement of the W mass. In 1996, L3 has taken data corresponding to an integrated luminosity of 11 pb^{-1} at a center-of-mass energy $\sqrt{s} = 161.34 \pm 0.06$ GeV. In this section, the W mass will be derived from the WW production cross section measured in that data sample.

The GENTLE [109] program has been used to calculate the dependence of the CC03 WW production cross section on the W mass at this value of $\sqrt{s}$. The cross section for WW $\rightarrow \mathrm{q\bar{q}q\bar{q}}$ is derived from this calculation by multiplication with the Standard Model branching fraction Br(WW $\rightarrow \mathrm{q\bar{q}q\bar{q}}$) = 45.6 %. The result is graphically shown in Figure 5.14. The uncertainty of this calculation is estimated to be 2% [40].

As shown in Table 5.2, the CC03 cross section for WW $\rightarrow \mathrm{q\bar{q}q\bar{q}}$ at $\sqrt{s} = 161$ GeV was measured to be $\sigma_{\mathrm{WW}\rightarrow\mathrm{q\bar{q}q\bar{q}}} = 0.98^{+0.51}_{-0.40}$ pb. For this sample, the systematic error on the measured cross section was estimated to be 5%, evaluated as explained earlier in this chapter, and dominated by the uncertainty in the description of the Monte Carlo of the neural network input parameters. Using the GENTLE calculation and the measured cross section for WW $\rightarrow \mathrm{q\bar{q}q\bar{q}}$, the W boson mass is measured to be:

$$m_{\mathrm{W}} = 81.33^{+1.17}_{-0.72} \pm 0.03 \ \ \mathrm{GeV} \tag{5.11}$$

where the first error includes statistical and systematic errors from the cross section measurement as well as the uncertainty on the GENTLE calculation, and the second error arises from the uncertainty on the LEP beam energy.

At $\sqrt{s} = 161$ GeV, the WW production cross section was also measured in the other decay modes $\mathrm{q\bar{q}}\ell\nu$ and $\ell\nu\ell\nu$ ($\ell = \mathrm{e}, \mu, \tau$). Combining all these measurements, the total WW production cross section was measured to be $\sigma_{\mathrm{WW}} = 2.89^{+0.83}_{-0.72}$ pb, combining statistical and systematic errors. From this measurement, and the GENTLE calculation for the dependence of the total cross section on m_{W}, the W mass is derived to be

$$m_{\mathrm{W}} = 80.80^{+0.48}_{-0.42} \pm 0.03 \ \ \mathrm{GeV} \tag{5.12}$$

At center-of-mass energies well above threshold, the dependence of the WW production cross section on the W mass is significantly reduced. This is shown graphically in Figure 5.15. As can be seen from the Figure, it is not useful to derive a W mass from the WW cross sections at these higher center-of-mass energies. Instead, in the next chapter the W mass will be derived directly from kinematical information in selected WW events.

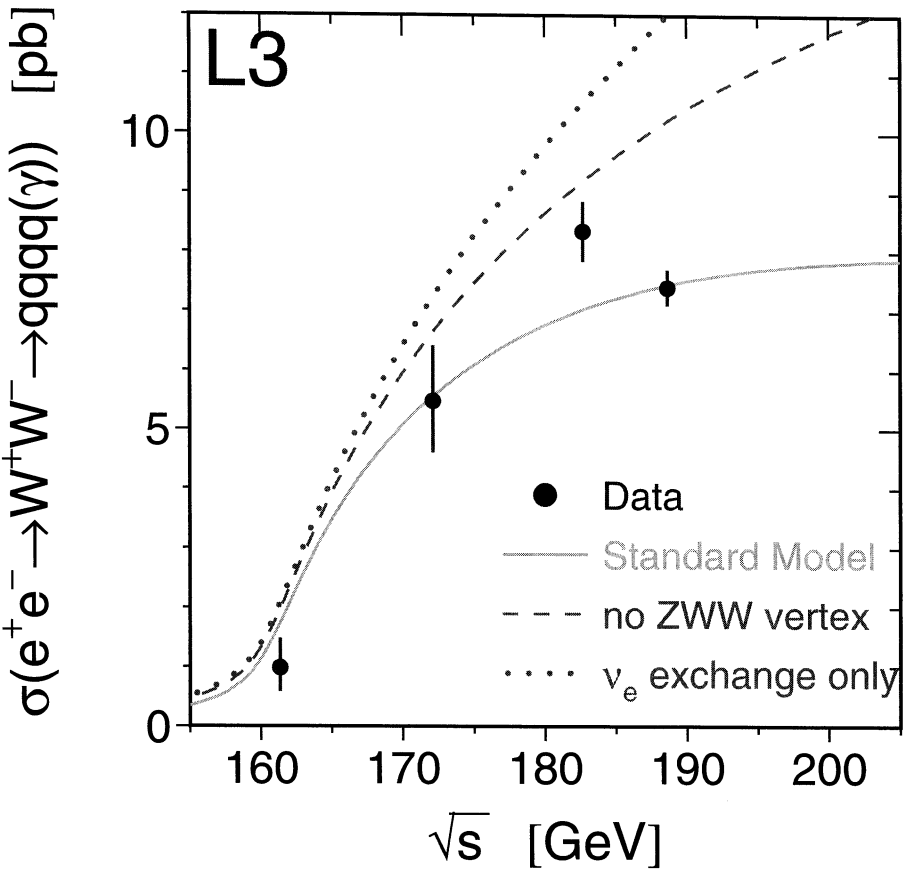

Figure 5.13: *Results of the* $W^+W^- \to q\bar{q}q\bar{q}$ *cross section measurements as presented in this thesis, for* $\sqrt{s} = 161, 172, 183$ *and* 189 GeV. *Errors shown include statistical and systematic errors. Also shown are the Standard Model prediction, the theoretical expectation if the WWZ vertex would not exist, and the theoretical prediction if only the neutrino exchange diagram existed.*

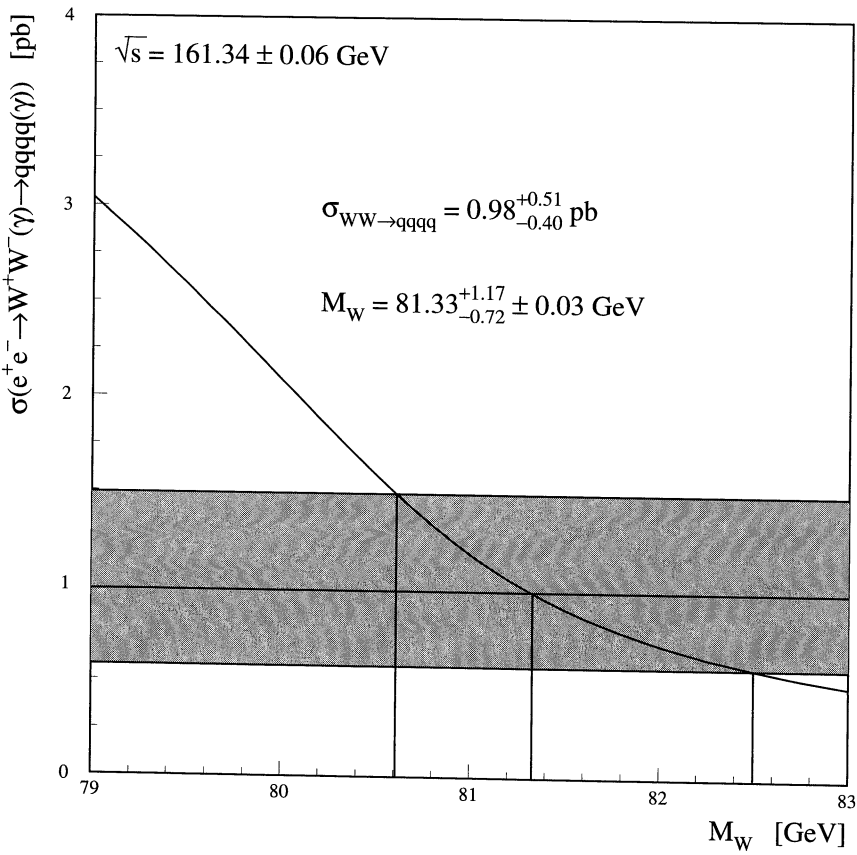

Figure 5.14: *Dependence of the CC03 cross section for WW → $q\bar{q}q\bar{q}$ on the W mass (m_W) at $\sqrt{s} = 161.34$ GeV, as calculated with GENTLE. Our measurement of this cross section, including its combined statistical and systematic error, is shown as a band. The error of 0.03 GeV on m_W is due to uncertainties in the LEP beam energy.*

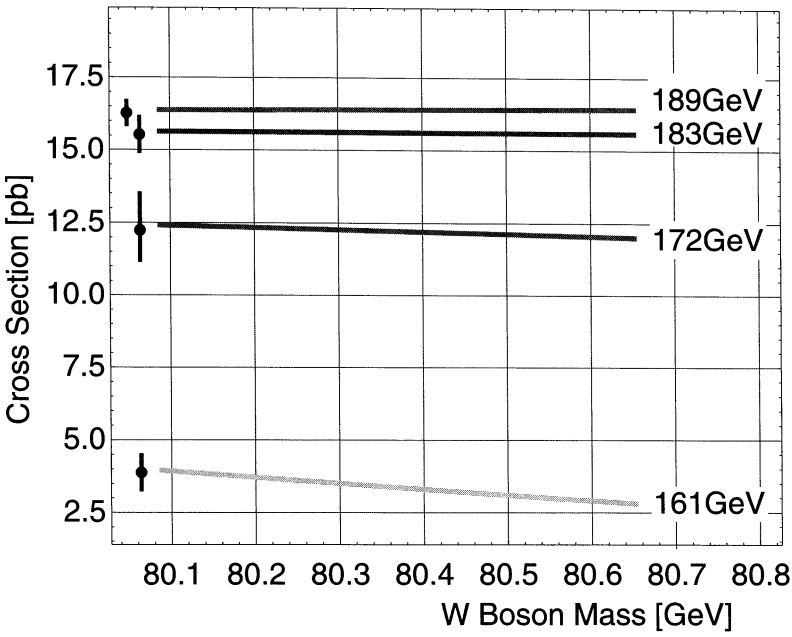

Figure 5.15: *Dependence of the total CC03 cross section for WW production on the W boson mass at various values of $\sqrt{s}$. On the left side, an indication is given for the experimental accuracy reached at each $\sqrt{s}$, with the centers of the error bars at arbitrary position.*

Chapter 6

Direct W Mass Measurement

In this chapter, we will use the selected WW events to measure the W mass, m_{W}. The WW production cross section σ_{WW} is sensitive to the W mass at center-of-mass energies close to threshold, $\sqrt{s} \approx 2m_{\mathrm{W}}$, and this sensitivity has been used to measure the W mass in the 1996 data at $\sqrt{s} = 161.3$ GeV, covered in Section 5.6. At higher center-of-mass energies, most information on m_{W} is present in the event kinematics.

To study the event kinematics we make use of the event selection as described in the previous chapter, but we add the following two cuts:

1. The neural net output value $\mathrm{nn}_{\mathrm{out}}$ should be larger than 0.6, see Figure 5.7. The overall signal efficiency for this cut, including the preselection cuts, is 85.4%, the remaining background is 1.6 pb.

2. The probability of the χ^2 of the best combination in the five-constraints kinematic fit, $\mathrm{P}_{5\mathrm{C}}$, should exceed 0.01.

The distribution of $\mathrm{P}_{5\mathrm{C}}$ is shown in Figure 6.1 for the events selected with $\mathrm{nn}_{\mathrm{out}} > 0.6$.

A cut on $\mathrm{P}_{5\mathrm{C}}$ is applied since the first bin is likely to contain misreconstructed events and has a high background. The misreconstruction can consist of effects like a jet in the beam pipe, particles clustered to the wrong jet, one or more high energy ISR photons, etc. The data shows an excess at low values of $\mathrm{P}_{5\mathrm{C}}$ in comparison to the Monte Carlo expectation; the effects of this will be discussed in the section on systematic errors.

6.1 Fit Method

The W mass is determined in a maximum likelihood fit. Ideally, the likelihood is constructed as

$$\mathcal{L}(m_{\mathrm{W}}) = \prod_{i=1}^{N_{\mathrm{ev}}} \mathcal{L}_i(m_{\mathrm{W}}; \vec{v}_i^{\,\mathrm{measured}}), \tag{6.1}$$

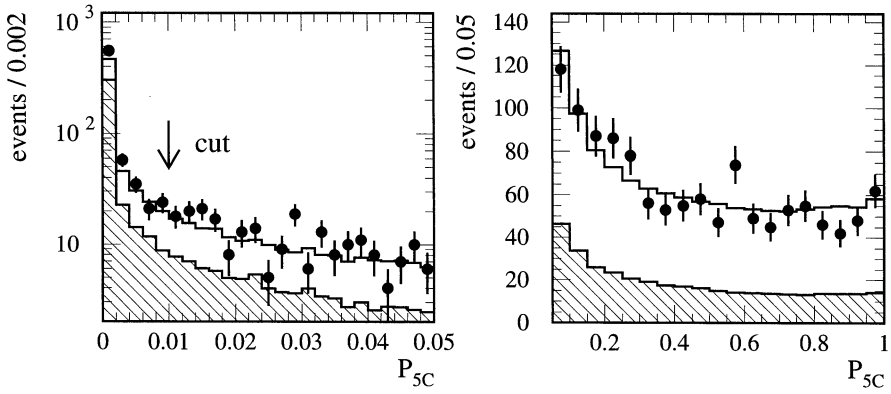

Figure 6.1: *Distribution of the probability of the χ^2 of the best combination in the five-constraints kinematic fit, P_{5C}, for events selected with $nn_{out} > 0.6$. Left: 0.–0.05 range; right: 0.05–1.0 range. Dots are data, open histograms are the WW signal Monte Carlo, and dashed histograms represent the background.*

where $\vec{v}_i^{\,\text{measured}}$ is the set of measured quantities that are sensitive to the W mass for event i, and the product runs over all selected events N_{ev}. An obvious choice for $\vec{v}^{\,\text{measured}}$ would be the 4-momenta of the four reconstructed jets, possibly supplemented with variables indicative of the quality of reconstruction of this particular event. An example of such a variable could be y_{45}; if it is high the event is compatible with a 5-jet hypothesis and there is a larger potential for misreconstruction.

The approach described above requires analytical knowledge of $\mathcal{L}_i$, which is in general not available. A possible solution consists of the use of an approximation to this event likelihood $\mathcal{L}_i$. Although an approximation is not fully correct, much information available in the event can be used. A drawback is the fact that the result will in general be biased and does not give a reliable error estimate. In addition, the bias may depend on assumptions made in the approximation for $\mathcal{L}_i$, e.g. the bias may depend on an implicit assumption for m_W. Careful Monte Carlo studies could however be used to obtain a bias-corrected estimate of m_W^{measured} and a rescaled error estimate.

Our approach is to obtain a reliable estimate for $\mathcal{L}_i$, so that a true maximum likelihood fit can be performed, directly giving a bias-free estimate for m_W and a proper error estimate. The vector $\vec{v}_i^{\,\text{measured}}$ is chosen to be the W mass obtained from event i using a five-constraints kinematic fit (see Section 4.5), denoted as m_i^{5C}. Taking into account signal and background

we then obtain

$$\mathcal{L}_i(m_{\mathrm{W}}; m_i^{5\mathrm{C}}) = \left\{ \frac{d\sigma'_{\mathrm{WW}}}{dm^{5\mathrm{C}}}(m_{\mathrm{W}}; m_i^{5\mathrm{C}}) + \frac{d\sigma'_{\mathrm{bg}}}{dm^{5\mathrm{C}}}(m_i^{5\mathrm{C}}) \right\} / \left\{ \sigma_{\mathrm{WW}}^{\mathrm{measured}} + \sigma_{\mathrm{bg}}^{\mathrm{measured}} \right\}. \quad (6.2)$$

The primes in the differential cross sections in this equation indicate that the standard model cross sections $\frac{d\sigma}{dm^{5\mathrm{C}}}$ are rescaled to the total measured cross section $\sigma_{\mathrm{WW}}^{\mathrm{measured}}$:

$$\frac{d\sigma'_{\mathrm{WW}}}{dm^{5\mathrm{C}}}(m_{\mathrm{W}}; m_i^{5\mathrm{C}}) = \frac{\sigma_{\mathrm{WW}}^{\mathrm{measured}}}{\sigma_{\mathrm{WW}}^{\mathrm{SM}}(m_{\mathrm{W}})} \frac{d\sigma_{\mathrm{WW}}^{\mathrm{SM}}(m_{\mathrm{W}}; m_i^{5\mathrm{C}})}{dm^{5\mathrm{C}}}, \quad (6.3)$$

$$\frac{d\sigma'_{\mathrm{bg}}}{dm^{5\mathrm{C}}}(m_i^{5\mathrm{C}}) = \frac{\sigma_{\mathrm{bg}}^{\mathrm{measured}}}{\sigma_{\mathrm{bg}}^{\mathrm{SM}}} \frac{d\sigma_{\mathrm{bg}}^{\mathrm{SM}}(m_i^{5\mathrm{C}})}{dm^{5\mathrm{C}}}. \quad (6.4)$$

This procedure guarantees proper normalization of $\mathcal{L}_i$. In this way, no cross section information is used in the mass fit.

The differential cross sections $d\sigma_{\mathrm{WW}}^{\mathrm{SM}}/dm^{5\mathrm{C}}$ and $d\sigma_{\mathrm{bg}}^{\mathrm{SM}}/dm^{5\mathrm{C}}$ are obtained with a Monte Carlo numerical evaluation [110]. A set of N_{MC} Monte Carlo events are generated with an, in principle, arbitrary W mass $m_{\mathrm{W}}^{\mathrm{ref}}$. In order to generalize results to different W masses, an event weight $w_j(m_{\mathrm{W}})$ is calculated for each Monte Carlo event j as follows:

$$w_j(m_{\mathrm{W}}; m_{\mathrm{W}}^{\mathrm{ref}}) = \frac{\frac{d\sigma_{\mathrm{WW}}}{d\vec{\Omega}_j}(m_{\mathrm{W}})}{\frac{d\sigma_{\mathrm{WW}}}{d\vec{\Omega}_j}(m_{\mathrm{W}}^{\mathrm{ref}})} = \frac{|\mathcal{M}(m_{\mathrm{W}}; \vec{\Omega}_j)|^2}{|\mathcal{M}(m_{\mathrm{W}}^{\mathrm{ref}}; \vec{\Omega}_j)|^2}, \quad (6.5)$$

where $\vec{\Omega}_j$ denotes the 4-momenta of the four fermions in Monte Carlo event j, and $\sqrt{s}$.

Using the weighted Monte Carlo events set, and assuming that sufficient Monte Carlo statistics is available, the total cross section is given by:

$$\sigma(m_{\mathrm{W}}) = \sigma(m_{\mathrm{W}}^{\mathrm{ref}}) \frac{1}{N_{\mathrm{MC}}} \sum_{j=1}^{N_{\mathrm{MC}}} w_j(m_{\mathrm{W}}). \quad (6.6)$$

In a similar way, the differential cross section can be estimated by considering the weighted number of events in an interval of size Δ centered around $m_i^{5\mathrm{C}}$:

$$\frac{d\sigma}{dm^{5\mathrm{C}}}(m_{\mathrm{W}}; m_i^{5\mathrm{C}}) = \frac{1}{\Delta} \sigma(m_{\mathrm{W}}) \frac{\sum_{j \in \Delta} w_j(m_{\mathrm{W}})}{\sum_{j=1}^{N_{\mathrm{MC}}} w_j(m_{\mathrm{W}})}. \quad (6.7)$$

The method can trivially be extended to independent data sets (e.g. data from different years) by multiplication of the likelihoods.

6.2 Jet Pairing

In a WW $\rightarrow$ four-jet event, there are three different ways in which jets can be paired into two W bosons. For the measurement of the WW cross section a 4C kinematic fit was performed,

and the best pairing was chosen as described in Section 4.5.1. This method has a high probability of finding the right combination, but biases the mass distribution for signal and background. Although the fit result using reweighting will still be bias-free and give a correct estimate of the error, the resulting statistical sensitivity will not be optimal.

Instead, for every event three 5C kinematic fits are performed, and the resulting masses are ordered according to the probability of the χ^2 of the fits, P^i_{5C}. In Figure 6.2, the mass distributions are shown for the best fits, m^1_{5C} with the highest P_{5C}, the second best fits m^2_{5C}, and for the worst fit, m^3_{5C}. In all three distributions, only events passing the cut on P_{5C} are included. It is clear that there is mass information in the best pairing, but also in the second best pairing; these are the events in which the pairing with the second best χ^2 is closest to the true pairing. On the other hand, there is very little mass information in the worst pairing, which nearly always corresponds to a pairing of jets from different W's. In addition, in the third pairing most events do not pass the cut on P_{5C}.

Since for any given event m^1_{5C} and m^2_{5C} correspond to different pairings of jets, and only the correct pairing contains information on the W mass, m^1_{5C} and m^2_{5C} are in good approximation independent. This was checked with Monte Carlo samples, and a correlation $\rho = 0.1 \pm 1.4\%$ was found between the mass fitted using the first and the second sample. In the mass fit, we thus use the first and second pairing as independent data sets, multiplying the likelihoods.

6.3 Monte Carlo Statistics

The reweighting method only works correctly if sufficient Monte Carlo statistics is available [111]. In our method, the likelihood is evaluated numerically by counting Monte Carlo events in a box around the data events, and the likelihood thus has a statistical error that needs to be taken into account, and which would not be there if the likelihood were calculated analytically. In principle, this means that the fit method is not a proper likelihood fit, and therefore not necessarily bias-free. The effect is in particular important since, when reweighting is performed, the effective Monte Carlo statistics N_{MC} is proportional to $(\sum w_i)^2 / \sum w_i^2$, which depends on m_{W}.

In the fit of the WW cross section explained in Section 5.4, the Monte Carlo statistics was taken into account by letting the observed number of Monte Carlo events in a bin be a stochastic variable depending on the expected number of Monte Carlo events in that bin, and a corresponding term was added to the likelihood in equation 5.6. The dependence of the effective Monte Carlo statistics on the fit result m_{W} prohibits the use of a similar procedure here; this turns out to be a fundamental limitation of this method [112]. The influence of finite Monte Carlo statistics on the final result needs to be checked carefully, which will be done in the next section.

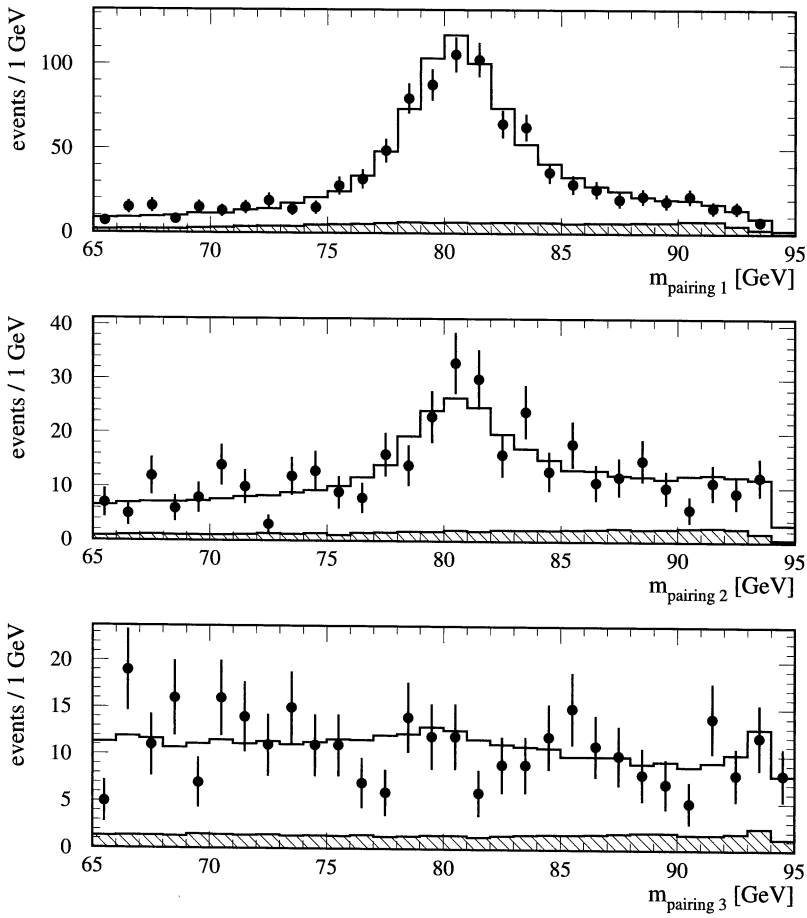

Figure 6.2: *Mass distributions for the pairing with the best χ^2, the second best χ^2, and the worst χ^2. For the two top plots, $P(\chi^2) > 0.01$, the events in the bottom plot are the same events as those in the middle plot as only very few events have $P(\chi^2) > 0.01$ for the third pairing.*

6.4 Implementation and Technical Checks

For the results given here, the fit method as explained in section 6.1 was used. Only events with $70 \leq m^i_{5C} \leq 100$ GeV were used in the fit; events outside this window have no mass information and are dominated by background.

The influence of the box size Δ in equation 6.7 on the fit results was studied. In Figure 6.3, the statistical error of the fit result is plotted as a function of Δ. Based on this plot, Δ was fixed to a value of 0.5 GeV, at the right side of the plateau. For very low values of Δ, Monte Carlo statistics in each box is insufficient and the apparent decrease of the error is artificial and in fact incorrect. At high values of Δ, the box size is too large to accommodate changes in the likelihood within the box, and statistical sensitivity is lost.

The linearity and bias of the fit were checked with Monte Carlo samples generated at various values of m_{W} between 80.0 and 81.0 GeV. Results of fitted minus generated mass are shown in Figure 6.4 for fits with box size 0.5 GeV, 0.1 GeV and 0.01 GeV. It can be seen that the fits with box size 0.5 and 0.1 GeV are linear and unbiased for all input masses, whereas the fit with very small box size 0.01 GeV is not linear, and biased for input masses away from the mass used in the sample being reweighted. This is due to too small Monte Carlo statistics in the boxes.

The accuracy of the error on the mass coming out of the fit was checked by performing the fit repeatedly on samples of Monte Carlo events, each corresponding to an integrated luminosity equal to the data. Results are shown in Figure 6.5. It can be seen that the width of the distribution of W mass fit results corresponds well to the errors coming out of the fits. The expected statistical error on the extracted W mass from samples of this size is 125 MeV.

6.5 Results and Systematic Error Analysis

Applying the fit to the $\mathrm{q\bar{q}q\bar{q}}$ data at $\sqrt{s} = 189$ GeV, the following result is obtained:

$$m_{\mathrm{W}} = 80.471 \pm 0.133 \ \text{GeV}, \tag{6.8}$$

where the error is statistical only. The error is slightly larger than expected from Monte Carlo studies (Figure 6.5); the probability to get an error of 133 MeV or larger is 10%.

Possible systematic influences on the result are studied in a way similar as done for the cross section measurement. For each effect, a Monte Carlo sample is made with a modeling of that effect different from the standard sample, and that new sample is then used as the baseline sample for the fit. The difference with the standard result is taken as an estimate of the systematic error for that effect. This method gives the "observed" systematic error on the selected data sample, in contrast to conventional methods in which a changed Monte Carlo sample is used as "fake data", which gives the "expected" systematic error. There is no statistical component to the systematic error due to the use of data in the test; this data is identical to the data in the standard fit.

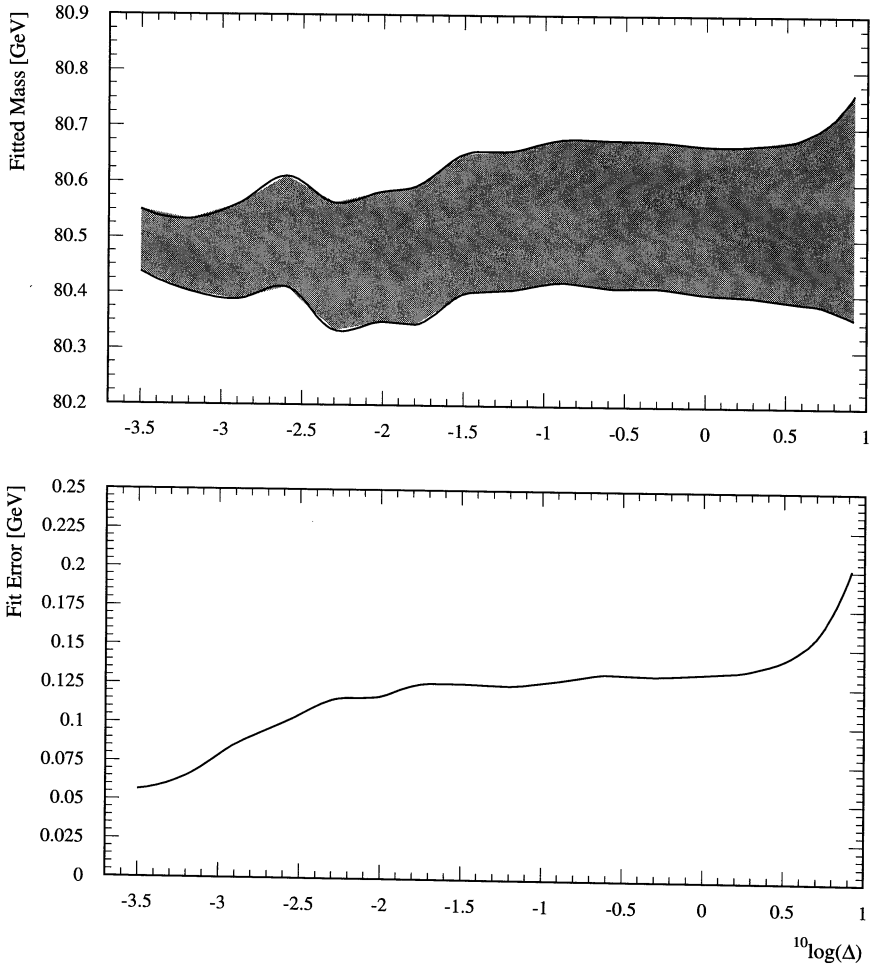

Figure 6.3: *Top: mass fit result on data as a function of the box size* Δ. *Bottom: fit error on data as a function of* Δ.

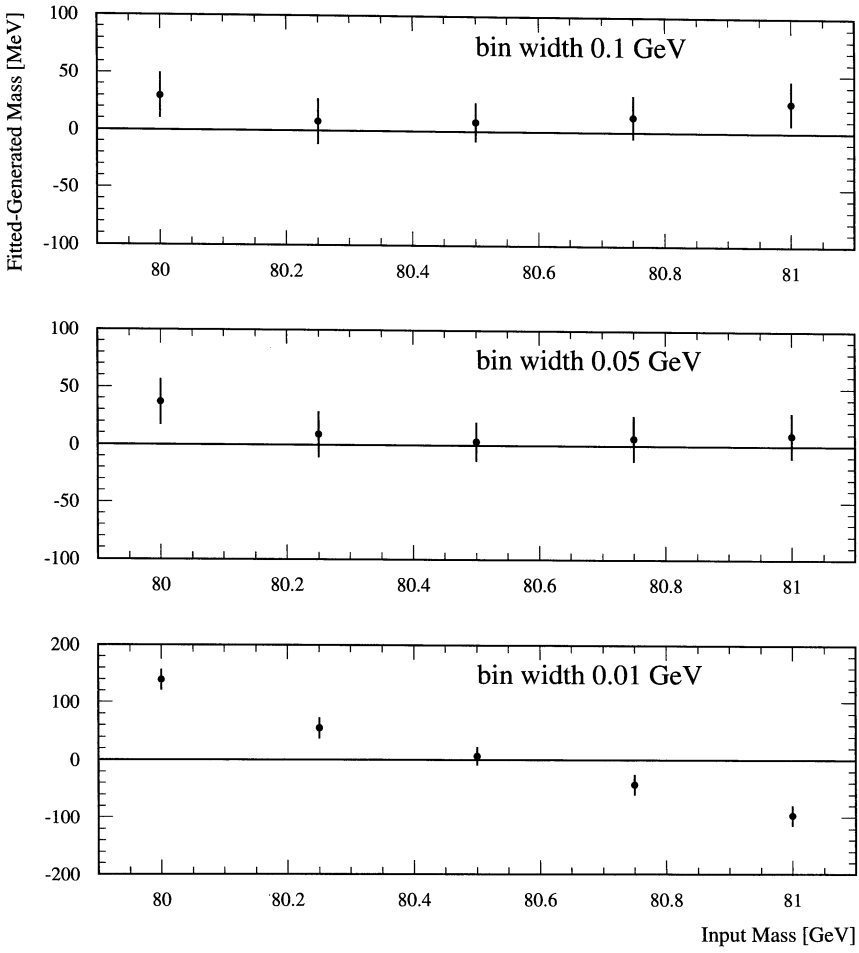

Figure 6.4: *Values of fitted minus generated mass for various input masses between* 80.0 *and* 81.0 GeV, *for fits with box size* 0.5 GeV *(top),* 0.1 GeV *(center), and* 0.01 GeV *(bottom).*

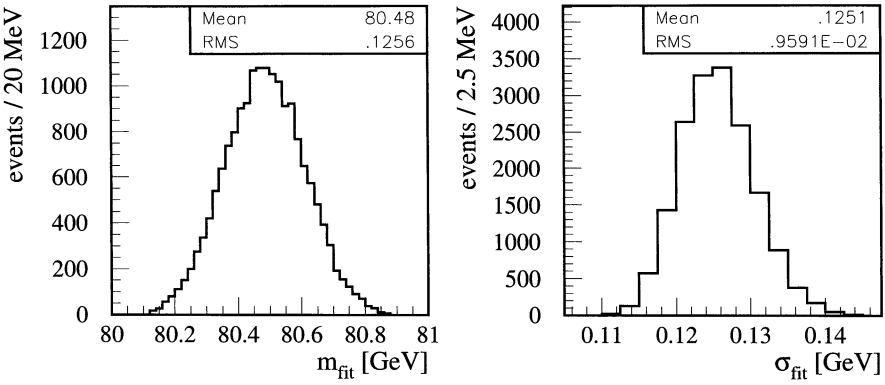

Figure 6.5: *Left: distribution of W mass fit results originating from fits to many Monte Carlo samples of size equal to the data. The assumed W mass in the Monte Carlo was* 80.5 GeV. *Right: distribution of the mass errors coming out of the fits.*

An intrinsic problem for all Monte Carlo-based methods of systematic error studies is the limited Monte Carlo statistics. For the samples used in these studies, the statistical uncertainties on the systematic errors are typically between 10 and 30 MeV, despite the generation of more than 10^6 Monte Carlo events.

6.5.1 Detector Response Uncertainties

A list of systematic errors assigned on m_W due to uncertainties in detector response is given in Table 6.1. A description follows below, but as most effects have already been discussed in the chapter on the cross section measurement more details are given there.

ECAL Energy Calibration

The BGO is calibrated with the RFQ and Xenon calibration systems before and after data taking and between fills, and with Bhabha events ($e^+e^- \rightarrow e^+e^-$) during data taking; the energy scale of the BGO for electromagnetically showering particles is known to 0.3%. For hadronic particles, the energy scale is less well known, and for the evaluation of the systematic error was scaled by $\pm 1\%$. Subsequently, the W mass analysis was repeated, and a shift of 19 MeV was found, which was assigned as a systematic error.

Source	Error on m_{W} [MeV]
ECAL Energy Calibration	19
HCAL Energy Calibration	2
Jet Angular Resolution	17
Cluster Simulation	13
g-factors	6
Cut on $P(\chi^2_{5C})$	4
Total	30

Table 6.1: *Assigned systematic error on m_{W}, in* MeV, *due to uncertainties in detector response.*

HCAL Energy Calibration

The analysis was redone with the HCAL energy scaled by $\pm 2\%$ to take into account uncertainties in the HCAL energy calibration. The resulting W mass shift of 2 MeV was taken as a systematic error.

Jet Angular Resolution

In order to take into account uncertainties in the angular resolution of jets, their position was smeared by 0.5 degrees, and the analysis was repeated. The W mass was found to be shifted by 17 MeV.

Cluster Simulation

The simulation of low energy clusters in the Monte Carlo is known to be problematic. In order to estimate the effect on the W mass, the distribution was shifted by 3 clusters and the analysis was repeated. This led to a shift of 13 MeV on the W mass, which was taken as a systematic error.

g-factors

In order to estimate the uncertainty in the g-factors, the analysis was repeated using in the Monte Carlo simulation the g-factors determined in the data, rather than those determined by Monte Carlo. Since these two sets of g-factors are known to be different, for understood reasons, half of the effect of 12 MeV is quoted as a systematic error.

Source	Error on m_W [MeV]
Background	
WW $\not\to$ $q\bar{q}q\bar{q}$ Background Scale	–
$q\bar{q}$ Background Scale	–
ZZ Background Scale	1
Four-Jet Description in $q\bar{q}$	4
ISR Description in $q\bar{q}$	3
Signal	
Four-Fermion vs CC03 Reweighting	4
ISR	10
FSR	3
Total	12

Table 6.2: *Assigned systematic error on m_W, in* MeV, *due to uncertainties in the modeling of signal and background in the Monte Carlo.*

Cut on $P(\chi^2_{5C})$

Since the amount of data and Monte Carlo events failing the cut on the probability of the 5C kinematic fit, $P(\chi^2_{5C})$, is not entirely equal, the analysis was redone without this cut. The effect on the resulting W mass is only 4 MeV.

Overall, the uncertainties in the modeling of the detector response lead to a systematic error on the W mass of 30 MeV.

6.5.2 Signal and Background Modeling

A list of systematic errors assigned on m_W due to uncertainties in the modeling of background and signal in the Monte Carlo is given in Table 6.2.

WW Non-four-quark Background Scale

The decay of W-pairs to final states other than $q\bar{q}q\bar{q}$ forms a background to the $q\bar{q}q\bar{q}$ final state. The W mass analysis was repeated scaling this background by an extreme value of $\pm 50\%$, and no effect was observed.

$q\bar{q}$ Background Scale

As explained in Chapter 5, the scale of the $q\bar{q}$ background, or rather its four-jet component, is determined from data with 5% accuracy. In the W mass analysis presented here, it was scaled by $\pm 5\%$, and no effect on the W mass was observed.

ZZ Background Scale

The second most important background to the $W^+W^- \rightarrow q\bar{q}q\bar{q}$ signal are ZZ events. The cross section for this background can be calculated to an accuracy of 2%, and has been measured to be in agreement with the prediction with an accuracy of 20%. In this analysis, the ZZ background was scaled by $\pm 5\%$ and the W mass analysis was repeated. A W mass shift of only 1 MeV was observed.

Four-Jet Description in $q\bar{q}$

As explained in Chapter 5, the incomplete description by the PYTHIA Monte Carlo of four-jet events in the QCD background can be taken into account by reweighting events, such that the y_{34} distribution is corrected. This procedure was also applied in the mass analysis; the shift of 7 MeV that was found was applied to the measured mass, and half of the shift is quoted as a systematic error.

ISR Description in $q\bar{q}$

As explained in Chapter 5, PYTHIA does not describe the ISR photon spectrum well. Like in the cross section analysis, this is taken into account by reweighting Monte Carlo events with a high p_T ISR photon such that the reweighted Monte Carlo and data agree in the ISR spectrum. The W mass analysis was repeated, the shift of 6 MeV that was found was applied to the W mass and half of the shift is quoted as a systematic error.

Four-Fermion versus CC03 Reweighting

The analysis was repeated by performing the mass reweighting with the full four-fermion matrix element rather than a Breit-Wigner, and the resulting difference of 4 MeV is quoted as a systematic error.

ISR Description in the Signal

As explained in Chapter 2, a theoretical uncertainty remains in the description of ISR in the WW signal: the full $\mathcal{O}(\alpha)$ corrections for off-shell WW production are not known. Instead, Monte Carlo programs like RacoonWW [33] and YFSWW3 [34] implement these corrections in the double pole approximation. Repeating the analysis with a YFSWW3 sample as

Monte Carlo reference sample, rather than KORALW, leads to a difference in fitted W mass of -8 ± 18 MeV. Since the DPA results are not yet the final word, and are estimated to lead to uncertainties of 10 MeV on the W mass [40], we take here 10 MeV as a systematic error.

FSR Description in the Signal

The comparison between YFSWW3 and KORALW described above does not automatically include uncertainties in the description of final state radiation in the Monte Carlo if there are quarks involved. In this case JETSET takes care of the FSR as gluon radiation is also a possibility. This uncertainty is therefore tested by removing all events with significant FSR from the Monte Carlo sample and repeating the analysis. Since this is of course unrealistic, one third of the effect of 9 MeV is taken as a systematic error.

Overall, the uncertainties in the modeling of signal and background in the Monte Carlo lead to a systematic error on the W mass of 12 MeV.

6.5.3 Fragmentation

The uncertainties on the m_{W} measurement due to fragmentation are estimated by exchanging the standard baseline Monte Carlo using JETSET for baseline Monte Carlo's using ARIADNE or HERWIG, or by variation of the JETSET parameters around their tuned values. The tuning of these programs is described in Section 3.3.1.

With ARIADNE, a shift in m_{W} of $+2 \pm 21$ MeV is observed. With HERWIG, using the JETSET particle decay tables, a shift of -7 ± 20 MeV is seen. When HERWIG is also used for the description of the background, the observed shift is $+8$ MeV, but the statistical error increases to 31 MeV.

As an alternative to comparing different models, within the JETSET model the tuned parameters Λ_{LLA}, b and σ_{q} were varied within their errors resulting from their tuning [46]. This was done for all three parameters with a fast detector simulation [103], and for Λ, which gave the largest effect, with full Monte Carlo simulation as well. The mass analysis performed on the output of the fast simulation is not completely identical to the one described here, but is very similar, and also based on Monte Carlo event reweighting. Where tested, fast simulation analysis and full analysis give consistent results [103]. It should be noted that in this fast detector simulation analysis, the baseline Monte Carlo sample was kept unchanged, but the data sample of which the mass is extracted was exchanged for Monte Carlo samples with fragmentation parameters varied.

The results on the mass shift obtained with the fast simulation are given in Table 6.3. The three JETSET parameters were varied by ± 2 and ± 3 standard deviations; one standard deviation equals 34 MeV for Λ, 34 MeV for σ_{q}, and 0.12 GeV^{-2} for b. The parameter Λ was also varied by ± 3 standard deviations in a full simulation Monte Carlo sample, with

	W mass shift (MeV)		
	Change Λ	Change σ_q	Change b
-3σ	$+43 \pm 12$	-14 ± 15	-49 ± 15
-2σ	$+36 \pm 12$	-12 ± 15	-23 ± 15
$+2\sigma$	-15 ± 13	-6 ± 15	$+6 \pm 15$
$+3\sigma$	-49 ± 13	$+10 \pm 15$	$+13 \pm 15$

Table 6.3: *Shifts in W mass, in* MeV, *for* $\pm 2\sigma$ *and* $\pm 3\sigma$ *changes in* Λ, σ_q *and* b.

the following results for the mass shift: $\Delta m = -28 \pm 14$ MeV for $\Lambda + 3\sigma$, and $\Delta m = +79 \pm 15$ MeV for $\Lambda - 3\sigma$. These shifts are consistent with the fast simulation result.

As mentioned in Section 3.3.1, the parameters were recently retuned for PYTHIA 6.1, which incorporates JETSET, with a larger sample of Z data events [82]. Although no Monte Carlo event samples were available yet at the time of writing of this thesis, it is interesting to look at the new tuning results. The new tuned parameters differ from the old parameters by 0.3 to 1.3 (old) standard deviations, and have errors that are 2.0 to 2.5 times smaller. Thus, it seems reasonable to take a ± 1 (old) standard deviation variation as an estimate for an error due to fragmentation parameter variation, which gives 18 MeV for Λ, 3 MeV for σ_q, and 9 MeV for b.

Considering the results of the comparisons between JETSET, ARIADNE and HERWIG, and the variation of the JETSET parameters, an error on m_W due to uncertainties in the fragmentation and hadronization of 20 MeV is assigned. With the new version 6.1 of HERWIG, and new parameter tunings in progress, one may expect this uncertainty to decrease in the final W mass analysis.

6.5.4 Final State Interactions

Final state interactions, subdivided in Bose-Einstein correlations and color reconnection, are studied with a number of Monte Carlo models.

Bose-Einstein Correlations

For the study of the effects of Bose-Einstein correlations on the W mass analysis, the LUBOEI routine as implemented in PYTHIA 6.1 is used, as discussed in Section 2.5.3. In this routine, particles (bosons) are reshuffled such as to reproduce phenomenologically the two-particle enhancement at low Q for like-sign particles. In order to restore energy-momentum conservation, a reshuffling involving all particles, including the unlike-sign particles, has to be done, and this can be done in various ways. In these studies reported here, the variants labeled BE_0 and BE_{32} were used. It may be noted that, although neither are theoretically

Model	Shift in m_{W} [MeV]
BE_0 all	$+71 \pm 16$
BE_{32} all	$+51 \pm 14$
BE_{32} intra-W	-4 ± 18

Table 6.4: *Observed shift in the measured m_{W}, in* MeV, *with respect to a baseline Monte Carlo without Bose-Einstein correlations, for various models. "All" stands for correlations applied between all particles, and "intra-W" stands for correlations applied to particles from the same W only.*

satisfactory, BE_0 should be considered particularly unrealistic. Both models have two free parameters corresponding to the correlation strength and the source radius; these parameters have been tuned by L3 to data, as discussed in Section 5.5.3.

The Bose-Einstein correlation effects are studied with a fast detector simulation routine as well as with a full simulation analysis. It should be noted that in the fast detector simulation analysis, the baseline Monte Carlo sample was kept unchanged, but the data sample of which the mass is extracted was exchanged for a Monte Carlo sample with Bose-Einstein correlations switched on. In the full analysis, however, the data sample is kept unchanged but the baseline Monte Carlo is exchanged; this gives shifts with opposite signs.

With the fast detector simulation, the following shifts were observed for BE_0 and BE_{32} with parameters as given above: BE_0: $\Delta m = -76 \pm 14$ MeV, BE_{32}: $\Delta m = -56 \pm 12$ MeV, BE_{32} intra-W Bose-Einstein correlations only: $\Delta m = -6 \pm 12$ MeV. For the full simulation analysis, shifts in measured m_{W} with respect to a Monte Carlo without Bose-Einstein correlations are reported in Table 6.4. As expected, intra-W Bose-Einstein correlations give no mass shift, whereas inter-W Bose-Einstein correlations give significant shifts for BE_0 as well as BE_{32}.

With the fast simulation, the dependence of the mass shift on the parameters $\lambda =$ PARJ(92) and $R =$ PARJ(93) have been investigated for the BE_{32} model. The results are shown in Fig 6.6. In this study, the remaining JETSET parameters were not retuned when the Bose-Einstein correlations parameters were changed, in contrast to the results given earlier in this section.

Bose-Einstein correlations in WW events have been studied by L3 in a dedicated study with data taken at $\sqrt{s} = 189$ GeV [49], as well as at higher energies [105, 50]. The conclusions from these studies are that correlations are observed within the same W with a strength compatible with those observed in light-quark Z decays, but that correlations between different W's are not observed in the data, and that their implementation in BE_{32} is excluded, by more than 4 standard deviations. In fact, similar studies of all four experiments are now consistent and observe no signs of correlations between different W's [105].

For a further discussion of the implications of these results, see Section 5.5.3. Models

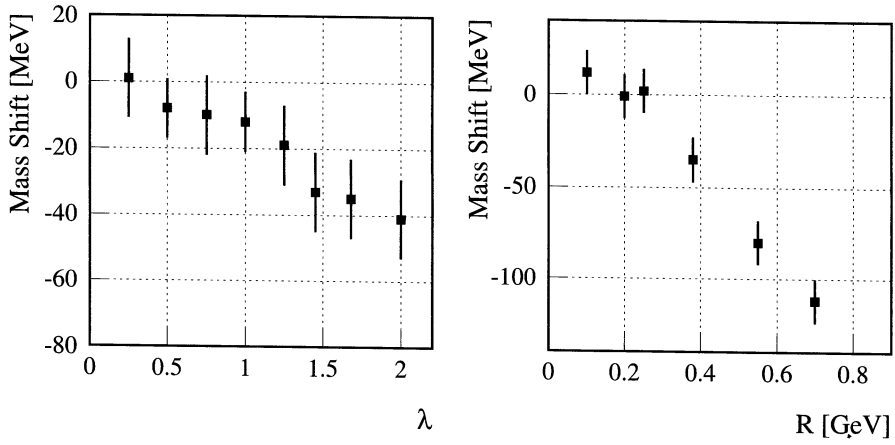

Figure 6.6: *Left: Shift in W mass as a function of* $\lambda =$ PARJ(92) *for the* BE_{32} *model. Right: shift in W mass as a function of* $R =$ PARJ(93) *in the* BE_{32} *model.*

of Bose-Einstein correlations based on the Lund string model intrinsically predict no Bose-Einstein correlations between different W's [51, 52]. Incoherent Bose-Einstein correlations from the HBT effect [106] only give small mass shifts from inter-W correlations [50]. Further models, based on global event reweighting, give resulting mass shifts of typically less than 10 MeV [53, 54].

Given the results discussed above, we assign a systematic uncertainty on m_{W} due to Bose-Einstein correlations, of no more than 10 MeV.

Color Reconnection

For the study of the effects of color reconnection, several models implemented in PYTHIA 6.1 [56, 57] and ARIADNE [58, 59] are used. The effect of these models on the W mass was studied with a fast detector simulation analysis as well as a full analysis of fully simulated events. Again, it should be noted that in the fast detector simulation analysis, the baseline Monte Carlo sample was kept unchanged, but the data sample of which the mass is extracted was exchanged for a Monte Carlo sample with color reconnection switched on. In the full analysis, however, the data sample is kept unchanged but the baseline Monte Carlo is exchanged; this gives shifts with opposite signs.

The SK I model as implemented in PYTHIA 6.1 has 1 free parameter κ, as explained in Section 2.5.4. This parameter effectively determines the fraction of events that are color reconnected. This dependence of the fraction of reconnected events on κ is $\sqrt{s}$ dependent;

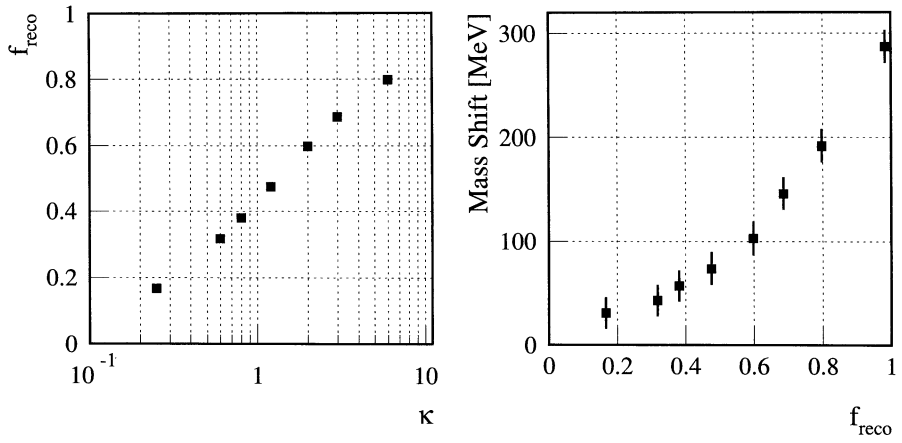

Figure 6.7: *Left: fraction of reconnected events, f_{reco}, in the SK I model, at $\sqrt{s} = 189$ GeV, without application of event selection, as a function of the free parameter κ. Right: shift in W mass as a function of the fraction of reconnected events, f_{reco}, at $\sqrt{s} = 189$ GeV, determined with a fast detector simulation analysis.*

Fig 6.7(left) shows this dependence at $\sqrt{s} = 189$ GeV. The W mass shift as a function of the fraction of reconnected events was studied with a fast detector simulation analysis, and the results are shown in Fig 6.7(right), and in Table 6.5.

The SK I model was studied in the full analysis with a Monte Carlo sample with $\kappa = 0.6$, as recommended by the authors of the SK I model [56, 57]. The result is shown in Table 6.6. The mass shifts in the SK I model as a function of κ have been studied by all four LEP experiments, and are identical for all four [113].

The full analysis results with the SK II and SK II' models are also given in Table 6.6. The fast simulation analysis gives for SK II (31.6% reconnected events): $\Delta m = -9 \pm 12$ MeV, and for SK II' (28.4% reconnected events): $\Delta m = +8 \pm 13$ MeV. The fast and full analysis results are consistent.

The ARIADNE color reconnection models have been discussed in Section 2.5.4. AR 1 allows no color reconnection between different W's, and thus should not lead to a mass shift, up to higher orders effects of changing the shape of jets. AR 3 is theoretically not attractive, as it allows reconnection also for hard gluons. The full analysis results on the W mass shifts are given in Table 6.6. As expected, AR 1 gives the smallest shift, and AR 3 the largest one. It should be noted that no retuning of the ARIADNE parameters has been performed for the individual models, although in principle that should be done since all models give an effect even in Z data. All four LEP experiments have used the ARIADNE models to estimate

κ	f_{reco} (%)	Δm (MeV)
0.25	16.7	$+31 \pm 15$
0.6	31.8	$+43 \pm 15$
0.8	38.0	$+57 \pm 15$
1.2	47.5	$+74 \pm 16$
2.0	59.8	$+103 \pm 16$
3.0	68.6	$+146 \pm 16$
6.0	79.8	$+192 \pm 16$
1000.	98.4	$+287 \pm 16$

Table 6.5: *Shifts in W mass, Δm, as a function of the free parameter κ in the SK I model at* 189 GeV, *determined with a fast detector simulation analysis. Also given is the fraction of reconnected events, f_{reco}, for each value of κ.*

Model	Shift in m_{W} [MeV]
PYTHIA SK I	-54 ± 17
PYTHIA SK II	-31 ± 18
PYTHIA SK II'	$+11 \pm 16$
ARIADNE 1	-33 ± 23
ARIADNE 2	-132 ± 24
ARIADNE 3	-203 ± 23

Table 6.6: *Observed shift in the measured m_{W}, in* MeV, *with respect to a baseline Monte Carlo without color reconnection, for various models, as determined with the full analysis at $\sqrt{s} = 189$* GeV.

mass shifts. Thereby OPAL and L3 have found significantly larger shifts than ALEPH and DELPHI; this is not understood.

Since all ARIADNE models give effects in Z data, the Z data could be used to test the ARIADNE models. This has up to now only been done by OPAL, with the result that the effects of AR 2 and AR 3 seem to be quite similar, and that both are in significant disagreement with the Z data [114].

Due to an error in the color reconnection model of HERWIG 5.9, this model is not used. Where it has been used, effects were consistent with zero.

The $\mathrm{W^+W^-}\rightarrow \mathrm{q\bar{q}q\bar{q}}$ data has also been used to directly search for effects of color reconnection [60]. The most sensitive way to study color reconnection has been found to compare the energy and particle flow between jets from the same W, and between jets from different W's. These studies show a good sensitivity to the predictions of the SK I model, and the $\mathrm{W^+W^-}\rightarrow \mathrm{q\bar{q}q\bar{q}}$ data excludes very large reconnection probability but is not inconsistent with the 30% of reconnected events predicted by the authors of the SK models, nor with zero. Similar conclusions are reached when studying the charged particle multiplicity in $\mathrm{q\bar{q}q\bar{q}}$ and $\mathrm{q\bar{q}}\ell\nu$ events. Finally, the W mass extracted from the LEP2 data, all four experiments combined, shows that the mass in $\mathrm{q\bar{q}q\bar{q}}$ and $\mathrm{q\bar{q}}\ell\bar{\nu}$ events differ by 9 ± 44 MeV, which is consistent with zero, and excludes very large amounts of color reconnection.

We conclude that the AR 2 and AR 3 models as currently implemented do not describe LEP1 data, and that the AR 3 model is in addition theoretically strongly disfavored. The SK models and AR 1 are, however, all still compatible with LEP2 data. The data excludes large amounts of reconnection, but neither no reconnection nor a moderate amount of reconnection, corresponding to 30% of reconnected events in the SK I model, can be excluded. Therefore, a systematic error on the W mass in the hadronic channel of 54 MeV is assigned due to color reconnection.

Combining the uncertainties of Bose-Einstein correlations and Color Reconnection, we arrive at a total FSI uncertainty on the W mass of 55 MeV.

6.5.5 LEP Energy Uncertainty

As discussed in subsection 3.1.1, the exact energy of the LEP beam has an uncertainty of 20 MeV at $\sqrt{s} = 189$ GeV. This uncertainty enters the W mass analysis through the fact that energy conservation is demanded in the constrained fit applied to the reconstructed events. This constraint leads to the relation:

$$\frac{\Delta m_{\mathrm{W}}}{m_{\mathrm{W}}} = \frac{\Delta E_b}{E_b}, \tag{6.9}$$

where E_b is the LEP beam energy and ΔE_b its uncertainty, and where Δm_{W} is the corresponding uncertainty on the W mass. This uncertainty thus equals 17 MeV for the 189 GeV data sample.

One may wonder if accuracy could be gained by not demanding energy conservation in the constrained fit. As explained in section 4.5, however, this leads to a dramatic worsening of event-by-event mass resolution, as well as increased dependence on uncertainties in the detector energy calibration.

6.5.6 Summary

Overall, at 189 GeV, the systematic errors assigned on the W mass measurement in the $q\bar{q}q\bar{q}$ channel are as follows: 12 MeV due to uncertainty in the Monte Carlo modeling, 30 MeV due to uncertainties in detector response, 20 MeV due to uncertainties in the Monte Carlo description of fragmentation, 55 MeV due to uncertainties in final state interconnection effects, and 17 MeV due to LEP. Therefore, the final result obtained at 189 GeV is:

$$m_W = 80.471 \pm 0.133\,(\text{stat}) \pm 0.038\,(\text{syst}) \pm 0.055\,(\text{FSI}) \pm 0.017\,(\text{LEP})\ \text{GeV}. \quad (6.10)$$

6.6 Combination

The direct measurement of the W mass in the $q\bar{q}q\bar{q}$ channel was also performed with the data taken at $\sqrt{s} = 172$ and 183 GeV, with the following result [115]:

$$m_W = 80.75 \pm 0.18\,(\text{stat}) \pm 0.07\,(\text{syst}) \pm 0.09\,(\text{FSI}) \pm 0.03\,(\text{LEP})\ \text{GeV}. \quad (6.11)$$

In that result, the systematic errors assigned for fragmentation and FSI uncertainties are larger than those found in this thesis. For the FSI error this is largely due to a large error assigned to Bose-Einstein correlation uncertainties, which are now considered to be small. The larger error due to fragmentation is due to a large JETSET-HERWIG difference; this difference has been discussed in Section 6.5.3 and we consider 20 MeV to be a more accurate assessment.

In order to combine that result with the result found at $\sqrt{s} = 189$ GeV, we take the systematic error due to final state interconnections (FSI) to be 55 MeV, fully correlated between the two data sets. A similar procedure is followed for the fragmentation uncertainty of 20 MeV and the ISR uncertainty of 10 MeV. The LEP beam energy error is only partially correlated between years: 75% between 189 and 183 GeV, and 82% between 183 and 172 GeV. We assume here a correlation between the 189 GeV beam energy error and the error on the earlier result of 75%.

Combining all $q\bar{q}q\bar{q}$ data from 172 to 189 GeV, we obtain:

$$m_W = 80.571 \pm 0.107\,(\text{stat}) \pm 0.034\,(\text{syst}) \pm 0.055\,(\text{FSI}) \pm 0.017\,(\text{LEP})\ \text{GeV}. \quad (6.12)$$

Chapter 7

Discussion

In the previous chapters of this thesis two analyses have been presented: a measurement of the cross section of the process $e^+e^- \rightarrow WW \rightarrow q\bar{q}q\bar{q}$ between $\sqrt{s} = 161$ GeV and 189 GeV, and a measurement of the W boson mass in that final state. In this chapter, the implications of these results in the framework of the Standard Model as well as for signs of new physics beyond the Standard Model will be discussed.

7.1 Cross Section

The results for the measurement of the $e^+e^- \rightarrow WW \rightarrow q\bar{q}q\bar{q}$ cross section between $\sqrt{s} =$ 161 GeV and 189 GeV have been shown in Table 5.2, with a discussion of systematic errors in Section 5.5. Graphically, these results are shown in Figure 5.13.

The results can be interpreted in a number of ways. The cross section depends on the W mass; this has been discussed in Section 5.6. Significant sensitivity exists only at the threshold. The cross section depends on the details of the couplings between the gauge bosons, and can be used to extract non-SM (anomalous) triple gauge-boson couplings. L3 has also measured the cross sections for $e^+e^- \rightarrow WW$ in other, semileptonic and pure leptonic, final states. Together with the hadronic final state these can be used to extract the branching fractions of the W into various final states, as well as information on the CKM matrix. The measurements can be used to constrain decays of the W into particles that cannot be observed (invisible decays), as can happen in various models of physics beyond the Standard Model. Finally, the results will be interpreted in the framework of a model involving large extra dimensions.

7.1.1 Anomalous Couplings

At LEP1, the couplings between the vector bosons and fermions have been measured accurately and turn out to be in good agreement with the Standard Model predictions, which

may be taken as evidence for the gauge boson nature of the W and the Z. Nevertheless, the particular predictions of the Standard Model as a $SU(2) \times U(1)$ gauge theory for the non-Abelian self-couplings of the W, the Z and the photon are much better measured at LEP2. In particular the triple gauge boson couplings WWγ and WWZ can be constrained via the measurement of WW production; LEP2 is not very sensitive to quartic gauge couplings and they will not be discussed here.

It is convenient to write out the most general allowed WWV (V $\equiv \gamma$ or Z) vertex in the form of a purely phenomenological effective Lagrangian [116, 117]:

$$\begin{aligned} i\mathcal{L}_{eff}^{WWV} &= g_{WWV}\Big[g_1^V V^\mu \left(W^-_{\mu\nu}W^{+\nu} - W^+_{\mu\nu}W^{-\nu}\right) \\ &+ \kappa_V W^+_\mu W^-_\nu V^{\mu\nu} + \frac{\lambda_V}{m_W^2} V^{\mu\nu} W^{+\rho}_\nu W^-_{\rho\mu} \\ &+ ig_5^V \varepsilon_{\mu\nu\rho\sigma}\left((\partial^\rho W^{-\mu})W^{+\nu} - W^{-\mu}(\partial^\rho W^{+\nu})\right) V^\sigma \\ &+ ig_4^V W^+_\mu W^-_\nu \left(\partial^\mu V^\nu + \partial^\nu V^\mu\right) - \frac{\tilde{\kappa}_V}{2} W^-_\mu W^+_\nu \varepsilon^{\mu\nu\rho\sigma} V_{\rho\sigma} \\ &- \frac{\tilde{\lambda}_V}{2m_W^2} W^-_{\rho\mu} W^{+\mu}_\nu \varepsilon^{\nu\rho\alpha\beta} V_{\alpha\beta}\Big] \end{aligned}$$

which gives the most general Lorentz invariant WWV vertex, for effectively massless fermions. The overall normalization is $g_{WW\gamma} = e$ and $g_{WWZ} = e\cot\theta_W$, with θ_W the weak mixing angle. In the expression for the effective Lagrangian, $W_{\mu\nu} = \partial_\mu W_\nu - \partial_\nu W_\mu$, and $V_{\mu\nu} = \partial_\mu V_\nu - \partial_\nu V_\mu$. The effective Lagrangian has a total of 14 arbitrary parameters, or couplings. Electromagnetic gauge invariance requires $g_1^\gamma(q^2 = 0) = 1$ and $g_5^\gamma(q^2 = 0) = 0$. The couplings g_4^V, $\tilde{\kappa}_V$ and $\tilde{\lambda}_V$ violate CP. If they are non-zero they are at least expected to be much smaller than the CP conserving couplings [117], and they will not be considered here. The coupling g_5^V conserves CP, but violates C and P individually, and will also not be considered. Six couplings remain; in the Standard Model, at tree level, $g_1^\gamma = g_1^Z = \kappa_\gamma = \kappa_Z = 1$, and $\lambda_\gamma = \lambda_Z = 0$.

For the WWγ vertex, these couplings correspond to the lowest order terms of a multipole expansion of the W-photon interactions: the charge of the W boson Q_W, its magnetic dipole moment μ_W, and its electric quadrupole moment q_W:

$$Q_W = eg_1^\gamma \ , \ \mu_W = \frac{e}{2m_W}(g_1^\gamma + \kappa_\gamma + \lambda_\gamma) \ , \ q_W = -\frac{e}{m_W^2}(\kappa_\gamma - \lambda_\gamma). \tag{7.1}$$

Thus, we will take $g_1^\gamma = 1$ and not consider it further. For g_1^Z and the κ's it is convenient to define deviations from the Standard Model values as $\Delta g_1^Z = g_1^Z - 1$ and $\Delta\kappa_V = \kappa_V - 1$.

Deviations from the Minimal Standard Model couplings are predicted in extensions of the Standard Model, for example in models with an extra Z′ boson, as well as in supersymmetric models.

Further study of the anomalous couplings learns that the following constraints can be used with only small loss of generality:

$$\Delta\kappa_\gamma = \cot^2\theta_W(\Delta\kappa_Z - \Delta g_1^Z) \ , \ \lambda_\gamma = \lambda_Z, \tag{7.2}$$

where θ_W is the weak mixing angle. These constraints protect the well-measured LEP1 observables against too large effects from anomalous WWZ and WWγ couplings [117].

The anomalous couplings enter as modifications to the couplings in the WWZ and WWγ vertex. This has the following consequences:

1. The total WW cross section depends quadratically on the anomalous couplings. Suppose that all couplings but one have their Standard Model value, but that coupling X deviates from it. Then:

   $$\sigma_{WW} = \sigma_{WW}^{SM} + aX + bX^2, \tag{7.3}$$

   where a and b are calculable factors, and $b > 0$ [118]. For large $|X|$, the cross section will be significantly larger than the Standard Model value. In the Standard Model, the non-Abelian self couplings of the gauge bosons provide the delicate gauge cancellations that are needed to prevent the cross section from growing beyond the unitarity bounds. Anomalous couplings destroy part of these gauge cancellations. This can be seen in Figure 5.13, where, apart from the Standard Model prediction, also the theoretical predictions for the case of no WWZ coupling, and the case of ν exchange only, are plotted. For small $|X| \neq 0$, the cross section can also be somewhat below the SM value. However, the SM value always turns out to be close to the lowest allowed value.

2. The angular distribution of the W production, as well as the W polarization, are modified. The change in W polarization will affect the W decay angles. All in all, five angles describe the final state, and an analysis of the five-fold differential cross section gives information on the anomalous couplings. This goes beyond the scope of this thesis, more information can be found in [117].

For the couplings Δg_1^Z, λ_γ and $\Delta\kappa_\gamma$, the coefficients a and b of equation 7.3 have been calculated with EXCALIBUR [78], under the constraints of Equation 7.2. Examples of the fully hadronic WW cross section at $\sqrt{s} = 189$ GeV are shown in the top row of Figure 7.1. At 172 GeV and 183 GeV the curves look similar, generally the dependence of the cross section on the anomalous coupling is largest at highest $\sqrt{s}$.

Taking our measurements of the WW cross section, we are able to determine likelihood curves for each of the anomalous couplings, and from these likelihoods we calculate probability density functions. These are shown in Figure 7.1 for the data at 189 GeV (middle row), and all data combined (bottom row). At 189 GeV, our measurement agrees very well with the theoretical prediction for zero anomalous couplings, which is reflected in the probability density curves. Whenever a measured cross section is higher than the minimum of the theory

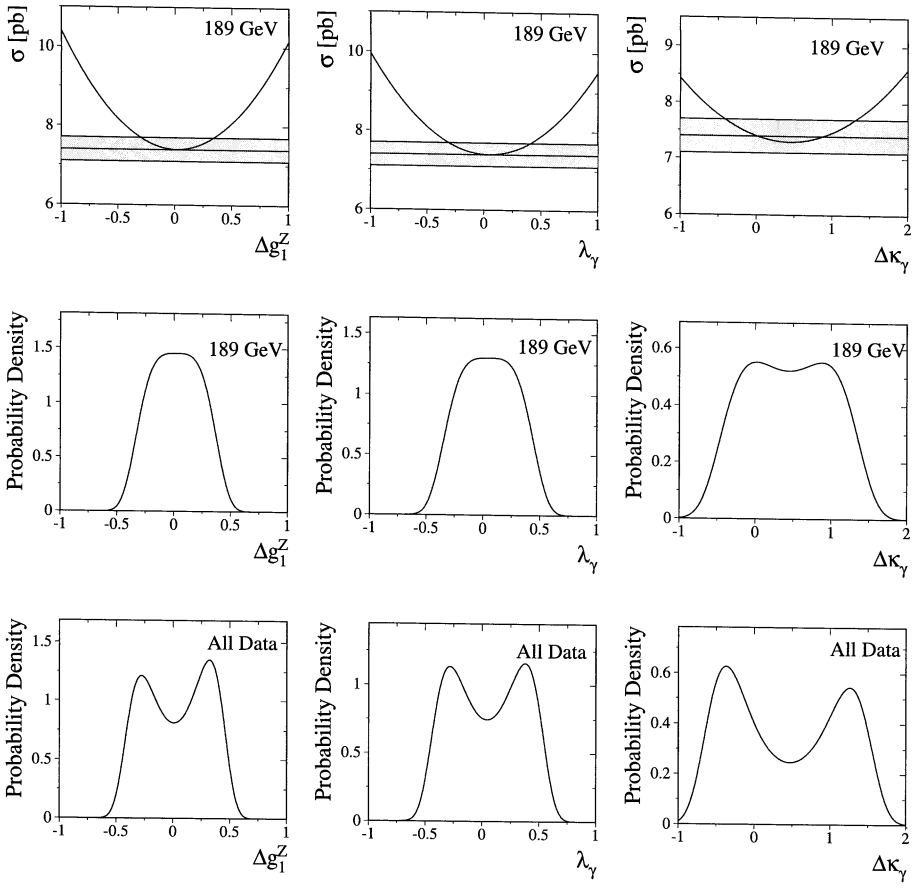

Figure 7.1: *Top row: fully hadronic WW cross section as a function of anomalous coupling at* $\sqrt{s} = 189$ GeV*; the shaded band represents the measurement. Middle row: Probability densities as a function of anomalous coupling at* 189 GeV*. Bottom row: idem, for the combination of all data.*

curve, a two-fold ambiguity arises due to the fact that the measured cross section is obtained for two different values of the couplings. At 183 GeV our measurement is 2.4 standard deviations higher than the Standard Model value, and this reflects in a double peak structure in the probability density curves for the combined data.

We will assume the 183 GeV result to be a statistical fluctuation, and use the probability density curves to derive limits on the anomalous couplings. This can be done by integration of the probability density functions and finding the 68% and 95% CL intervals. These intervals can be defined in a number of ways; in this thesis they are chosen such that the probability for the coupling to fall outside the interval is distributed symmetrically on the higher and lower side. We note from the probability density curves that zero anomalous couplings are consistent with the data. The results are:

$$-0.29 < \Delta g_1^Z < 0.36 \text{ at } 68\% \text{ CL } , -0.45 < \Delta g_1^Z < 0.50 \text{ at } 95\% \text{ CL}, \tag{7.4}$$

$$-0.31 < \lambda_\gamma < 0.42 \text{ at } 68\% \text{ CL } , -0.47 < \lambda_\gamma < 0.56 \text{ at } 95\% \text{ CL}, \tag{7.5}$$

$$-0.4 < \Delta\kappa_\gamma < 1.3 \text{ at } 68\% \text{ CL } , -0.7 < \Delta\kappa_\gamma < 1.6 \text{ at } 95\% \text{ CL}. \tag{7.6}$$

7.1.2 W Branching Fractions and the CKM Matrix

Apart from decaying in a quark-antiquark pair, a W boson can decay into a charged lepton (electron, muon or tau) and a neutrino. The presence of these decay modes gives rise to various final states other than the $q\bar{q}q\bar{q}$ mode already discussed: $q\bar{q}\ell\nu$ and $\ell\nu\ell\nu$, where any ℓ can be any of $\{e, \mu, \tau\}$. L3 has measured the cross sections for these final states at $\sqrt{s} = 161$ GeV [119], 172 GeV [120], 183 GeV [121], and 189 GeV [122].

The selection of $q\bar{q}\ell\nu$ events requires an identified high energy lepton, two hadronic jets with high particle multiplicity, and missing momentum due to one or more neutrinos. The lepton is typically isolated from the jets. The invariant mass of the two jets, as well as the lepton-missing momentum system, should be compatible with the W mass. Events are selected with an efficiency varying between 50% ($q\bar{q}\tau\nu$) and 80% ($q\bar{q}e\nu$ and $q\bar{q}\mu\nu$). Backgrounds are predominantly from fermion pair production, purities vary between 87% and 95%.

The event selection for $\ell\nu\ell\nu$ events requires two high energy acoplanar leptons with large missing energy due to the neutrinos. Selection efficiencies vary between 30% ($\tau\nu\tau\nu$) and 70% ($e\nu e\nu$), and purities between 65% and 97%; backgrounds are fermion pair production, two-photon collisions, and cosmics. Event displays of a selected $q\bar{q}e\nu$ candidate event and a selected $\mu\nu\tau\nu$ candidate event are shown in Figure 7.2 as examples of typically selected events with at least one leptonic W decay.

The measured cross sections for the various final states are summarized in Table 7.1.

For a W boson decaying into a final state $f\bar{f}'$, the branching fraction $B(W \to f\bar{f}')$ is defined as

$$B(W \to f\bar{f}') = \frac{\Gamma(W \to f\bar{f}')}{\Gamma_W^{\text{total}}}, \tag{7.7}$$

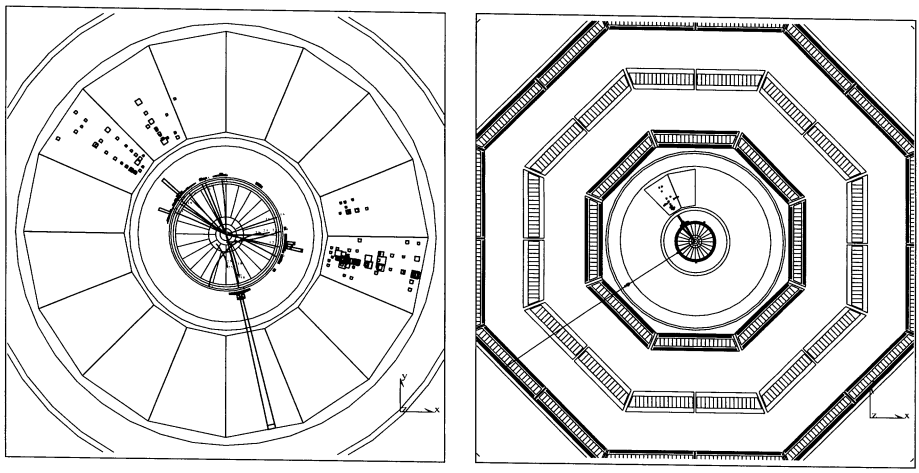

Figure 7.2: *Event displays of a selected* $q\bar{q}e\nu$ *candidate event (left), and a selected* $\mu\nu\tau\nu$ *candidate event (right), shown as examples of typically selected events with at least one leptonic W decay.*

with $\Gamma(W \to f\bar{f}')$ given by Equation 2.11, and Γ_W^{total} given by Equation 2.13.

The measured cross sections can be used to determine various W branching fractions. Since the measured cross sections for the various leptons in the final state are consistent with each other, we will assume lepton universality, as predicted by the Standard Model. This implies that the branching fractions $B(W \to \ell\nu)$ are identical for electrons, muons and taus. Thus, for each $\sqrt{s}$ we can write:

$$\sigma_{\ell\nu\ell\nu} = \sigma_{\text{total}} \times B(W \to \ell\nu)^2 \tag{7.8}$$

$$\sigma_{q\bar{q}\ell\nu} = 2\sigma_{\text{total}} \times B(W \to \ell\nu) \times B(W \to q\bar{q}) \tag{7.9}$$

$$\sigma_{q\bar{q}q\bar{q}} = \sigma_{\text{total}} \times B(W \to q\bar{q})^2, \tag{7.10}$$

where σ_{total} depends on $\sqrt{s}$, but the branching fractions do not.

Using the measurements in Table 7.1, the branching fractions $B(W \to q\bar{q})$ and $B(W \to \ell\nu)$ are determined in a combined fit, constraining the sum of the two branching fractions to one. The results are:

$$B(W \to q\bar{q}) = (68.20 \pm 0.68 \pm 0.33)\% \quad B(W \to \ell\nu) = (10.60 \pm 0.23 \pm 0.11)\%. \tag{7.11}$$

These results can be compared to the Standard Model predictions of 67.51% and 10.83%, respectively, which follow from Equations 2.11 and 2.13.

Process	$\sigma(CC03)$ [pb]			
	$\sqrt{s} = 161$ GeV	$\sqrt{s} = 172$ GeV	$\sqrt{s} = 183$ GeV	$\sqrt{s} = 189$ GeV
$\ell\nu\ell\nu$	$0.39^{+0.43}_{-0.27} \pm 0.02$	$1.93^{+0.74}_{-0.60} \pm 0.08$	$1.49 \pm 0.25 \pm 0.05$	$1.67 \pm 0.14 \pm 0.04$
$q\bar{q}e\nu$	$0.62^{+0.38}_{-0.27} \pm 0.03$	$2.44^{+0.64}_{-0.55} \pm 0.07$	$2.36 \pm 0.24 \pm 0.04$	$2.39 \pm 0.13 \pm 0.04$
$q\bar{q}\mu\nu$	$0.53^{+0.33}_{-0.24} \pm 0.03$	$1.06^{+0.44}_{-0.36} \pm 0.03$	$2.29 \pm 0.24 \pm 0.04$	$2.27 \pm 0.14 \pm 0.04$
$q\bar{q}\tau\nu$	$0.22^{+0.55}_{-0.38} \pm 0.04$	$1.60^{+0.81}_{-0.67} \pm 0.08$	$1.86 \pm 0.32 \pm 0.06$	$2.64 \pm 0.21 \pm 0.08$
$q\bar{q}q\bar{q}$	$0.98^{+0.51}_{-0.40} \pm 0.05$	$5.48^{+0.92}_{-0.85} \pm 0.17$	$8.35 \pm 0.46 \pm 0.23$	$7.40 \pm 0.26 \pm 0.15$

Table 7.1: *Cross sections measured by L3 for all WW final states, at* $\sqrt{s} = 161 - 189$ GeV. *The result given for* $\ell\nu\ell\nu$ *is summed over all leptons.*

The relation between the W-decay branching fractions and the six elements V_{ij} of the Cabibbo-Kobayashi-Maskawa quark mixing matrix V_{CKM} not involving the top quark is given by Equation 2.15. Using $\alpha_s(m_W^2) = 0.121 \pm 0.002$, the measurement of the branching fractions implies:

$$\sum_{i=\mathrm{u,c};j=\mathrm{d,s,b}} |V_{ij}|^2 = 2.065 \pm 0.064 \pm 0.032. \tag{7.12}$$

This measurement is a test for the unitarity of the CKM matrix, in which case this number should be 2.

This measurement can be used to constrain the least well known CKM matrix element, V_{cs}, using the measured values for the other five elements [7]. We derive:

$$|V_{\mathrm{cs}}| = 1.008 \pm 0.032 \pm 0.016. \tag{7.13}$$

It is interesting to compare this number to the direct determination of $|V_{\mathrm{cs}}|$ via decay of D mesons into kaons, $|V_{\mathrm{cs}}| = 1.04 \pm 0.16$, which suffers from a large uncertainty in the D form factor in these decays [7].

7.1.3 Invisible W Decays

In the Standard Model, the W decays either hadronically to a quark-antiquark pair, or leptonically to a charged lepton and a neutrino. In certain models of physics beyond the Standard Model, the W boson can decay to "invisible" final states, which by the nature of the final state particles are not observable in the detector. For example, in supersymmetric models the decay

$$\mathrm{W}^+ \to \chi^+\chi^0 \to \ell^+\chi^0\chi^0 \tag{7.14}$$

can occur. The χ^0 could be the lightest supersymmetric particle and would not decay in R-parity conserving supersymmetric models; it would leave the detector unobserved. If the mass difference between the χ^+ and the χ^0 is very small, less than a few GeV, the final state

lepton would have little energy, and might escape detection as well. Invisible W decay should thus be interpreted as W decay into a charged particle with momentum below detectability.

If the W boson decays to an unobservable final state, the total width of the W boson, Γ_W^{total}, is increased:

$$\Gamma_W^{\text{total}} = \Gamma_W^{\text{visible}} + \Gamma_W^{\text{invisible}} \tag{7.15}$$

where $\Gamma_W^{\text{visible}}$ is the W width into observable final states, and $\Gamma_W^{\text{invisible}}$ is the W width into invisible final states. The observable final states are none other than the Standard Model W decay modes. It is assumed in this section that the coupling of the W boson to the fermions in its Standard Model decay modes is known and given by the Standard Model. Therefore, we identify the visible W decay width with the Standard Model decay width:

$$\Gamma_W^{\text{visible}} = \Gamma_W^{\text{SM}}, \tag{7.16}$$

which equals 2.093 ± 0.003 GeV [7], as explained in Section 2.3. In the Standard Model, $\Gamma_W^{\text{invisible}} = 0$, a non-zero invisible width will affect the total W width.

A change in the total W width will affect the total cross section for WW production at LEP, as shown in Figure 7.3. The total cross section for WW production at any $\sqrt{s}$, for W bosons with a finite width, can be written as a convolution of a width-independent cross section and two Breit-Wigners, one for each W. The W width enters the Breit-Wigners, but it does so differently in numerator and denominator. The W width in the numerator is the sum of the partial decay widths for all decay modes under observation, i.e. it is $\Gamma_W^{\text{visible}} = \Gamma_W^{\text{SM}}$. The W width in the denominator is the total width Γ_W^{total} coming from the boson propagator term. The best theoretical estimate for the WW production cross section is given by the double pole approximation, discussed in section 2.4 and 2.5.1. This theoretical estimate is denoted here as $\sigma_{\text{WW}}^{\text{DPA}}$. Then, in presence of a non-zero invisible width, the total WW production cross section can be approximated by:

$$\sigma_{\text{WW}} = \sigma_{\text{WW}}^{\text{DPA}} \times \left(\frac{\Gamma_W^{\text{SM}}}{\Gamma_W^{\text{SM}} + \Gamma_W^{\text{invisible}}} \right)^2 . \tag{7.17}$$

The dominant error on σ_{WW} derived this way is the 0.5% uncertainty on $\sigma_{\text{WW}}^{\text{DPA}}$.

In this thesis, the fully hadronic WW cross sections have been analyzed between $\sqrt{s} =$ 161 and 189 GeV. The measurement at 161 GeV has no impact on the final result, and has not been used here. The other measurements can be transformed into a likelihood as a function of cross section. Using Equation 7.17, a WW cross section can be calculated for each value of the invisible width. Combining Equation 7.17 and the likelihood curves for the cross section, probability density functions can be calculated for each value of the invisible width. This is shown in Figure 7.4 for the data at 189 GeV (left), and combining all data between 172 and 189 GeV (right).

Combining all data, the invisible width $\Gamma_W^{\text{invisible}}$ is measured to be:

$$\Gamma_W^{\text{invisible}} = -39 \pm 34 \text{ MeV}. \tag{7.18}$$

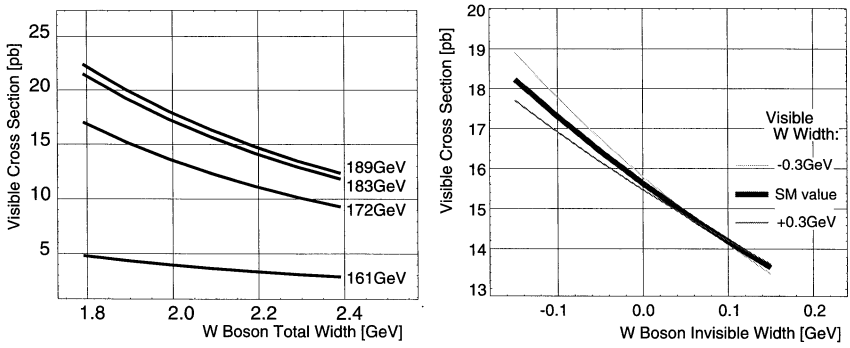

Figure 7.3: *Dependence of the total CC03 cross section for WW production on the W boson total width at various values of $\sqrt{s}$ (left), and on the W boson invisible width at $\sqrt{s} = 183$ GeV (right). In the right plot, also the dependence of the result on a ± 0.1 GeV, ± 0.2 GeV, and ± 0.3 GeV variation of the visible W width is shown.*

The result at 189 GeV alone is $\Gamma_W^{\text{invisible}} = 1 \pm 42$ MeV. The fact that the overall result is negative reflects the fact that the measured value of the WW cross section at $\sqrt{s} = 183$ GeV is higher than the theoretical prediction, whereas the measured cross section at 189 GeV is very close to the theoretical prediction.

Negative values for the invisible width should be regarded as unphysical. A 95% CL upper limit for the invisible width can be obtained by integration of the probability density function $\mathcal{P}(\Gamma)$ for $\Gamma_W^{\text{invisible}} > 0$, and determining the value x so that

$$\frac{\int_0^x \mathcal{P}(\Gamma) d\Gamma}{\int_0^\infty \mathcal{P}(\Gamma) d\Gamma} = 0.95. \tag{7.19}$$

This gives for the data at 189 GeV alone $\Gamma_W^{\text{invisible}} < 92$ MeV at 95% CL, and for all data combined:

$$\Gamma_W^{\text{invisible}} < 52 \text{ MeV at } 95\% \text{ CL}. \tag{7.20}$$

The upper limit is in principle influenced by the theoretical uncertainty on the WW cross section, as given by Equation 7.17. This uncertainty is estimated to be 0.5% of the total WW cross section, or 0.04 pb. Variation of $\sigma_{\text{WW}}^{\text{DPA}}$ by 0.04 pb turns out to have a negligible influence on the final result, which can be understood by the observation that it is an order of magnitude smaller than the systematic uncertainty on the measured cross section. Also the uncertainty on Γ_W^{SM} has a negligible effect on the final result.

The final result $\Gamma_W^{\text{invisible}} < 52$ MeV, at 95% CL, is significantly better than the PDG value [7] of $\Gamma_W^{\text{invisible}} < 139$ MeV, which contains only the ALEPH result up to $\sqrt{s} = 183$ GeV.

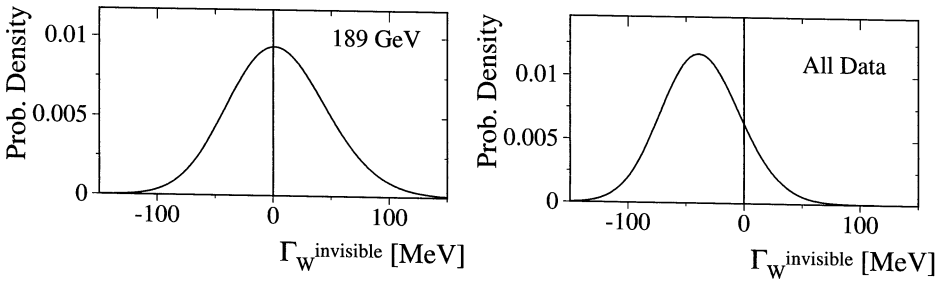

Figure 7.4: *Probability density functions for the invisible width $\Gamma_W^{\text{invisible}}$ following from the measurement of the fully hadronic WW cross section at $\sqrt{s} = 189$ GeV (left), and combining the measurements of the fully hadronic cross sections between $\sqrt{s} = 172$ and 189 GeV (right).*

A further consequence of invisible W decays is the increase of topologies of WW events with a single visible W decay accompanied by an invisible W decay, i.e. single-W events. Such events are also produced in the Standard Model through single-resonant four-fermion production graphs, as explained in Section 2.4. In principle the measurement of the cross section for these events can thus be used to put an upper limit on invisible W decays. However, the kinematics of such events differs from the Standard Model single-W production, and thus acceptance and efficiencies as determined in the standard single-W analysis are not valid for invisible W decays. The analysis of single-W events falls outside the scope of this thesis.

7.1.4 Large Extra Dimensions

The unification of the weak nuclear force and electromagnetism in the Standard Model is experimentally measurable at LEP because the center-of-mass energy of LEP is of the same order of magnitude as the electroweak unification scale of some 100 GeV. Gravity, however, at these energies is a much weaker force, characterized by Newton's constant $G_N \approx 6.7 \times 10^{-11}$ m^3 kg^{-1} s^{-2}. In fact, gravity only becomes of equal strength to the other fundamental forces at very high energy scales, characterized by the Planck mass of $M_{\text{Pl}} = \sqrt{\frac{1}{G_N}} \approx 10^{19}$ GeV, or distances of 10^{-35} m, the Planck length. The incorporation of gravity (i.e. general relativity) with quantum field theory is a major unsolved problem in particle physics. A possible solution is offered by the theory of strings, which may succeed in describing the unification of the forces at the Planck scale. However, the energy associated with the Planck

scale is 15 orders of magnitude larger than what will be attained at the LHC (a $\sqrt{s} = 14$ TeV pp collider under construction at CERN, Geneva), and experimental study seems very far away.

Recently, however, a hypothesis has been put forward that solves the problem of the weakness of gravity, and may make string theory accessible to energy scales that can be achieved in current colliders [15]. Strings exist in 10 dimensions, embedded in a more general theory (M-theory) that has 11 dimensions, 7 more than our familiar world of 1 time and 3 spatial coordinates. In conventional string theories, these additional dimensions are curled up (compactified) to very small sizes of order 10^{-32} m, and are thus not visible to us. There is, however, no particular reason why some of these extra dimensions could not be substantially larger.

Suppose that a number N of these extra dimensions have a size R considerably larger than 10^{-32} m. In string theory, the electroweak gauge fields (photons, W and Z bosons, gluons) are open strings with endpoints bound to 4-dimensional subspaces (branes, or walls), but the quanta of the gravitational field, gravitons, are closed strings that are allowed to roam freely through the other dimensions (the bulk). Gravity would then mainly operate in the bulk, and it would only appear weak to us since we are bound to the 4-dimensional world. The scale of gravity in our 4-dimensional world, the Planck scale M_{Pl}, is related to the effective scale of gravity in the $4 + N$ dimensional world, M_S, by Gauss' law, and it follows that

$$M_{\mathrm{Pl}}^2 \sim R^N M_S^{N+2}. \tag{7.21}$$

This way, the scale of gravity, M_S, might well be of the order of a TeV, rather than M_{Pl}, and the apparent weakness of gravity in our world is only a dimensional illusion. If this scenario is true, a number of extra dimensions with size considerably larger than 10^{-32} m would exist, which are thus denoted large extra dimensions (LED).

The existence of large extra dimensions influences the differential cross section for the $\mathrm{e^+e^-} \rightarrow$ WW process [123]. In addition to the CC03 diagrams, gravitons can mediate the scattering. The graviton effects are described in terms of the scale M_S, which appears as a term $\sim 1/M_S^8$ in the pure graviton exchange process, and as $\sim 1/M_S^4$ in the interference of graviton exchange and Standard Model processes [124]. These terms are multiplied by factors λ^2 and λ, respectively, which incorporate the dependence on the unknown full theory, and are of order unity [124]. In Figure 7.5, the effects of graviton exchange on the W production angle are shown for an example $M_S = 0.65$ TeV for fully hadronic and semileptonic events. The W production angle is determined by reconstructing the W directions from the jets, c.q. the lepton and neutrino. The lepton charge, or the sum of the charge of the particles in the jets, determines the charge of the W.

The measurement of the WW cross section can be used to measure M_S. Since our measurement agrees well the Standard Model prediction, a lower limit is set on M_S. For numerical results, the cases $\lambda = 1$ and $\lambda = -1$ are studied [125]. The inclusion of graviton exchange effects is performed by reweighting Monte Carlo events with a modified version

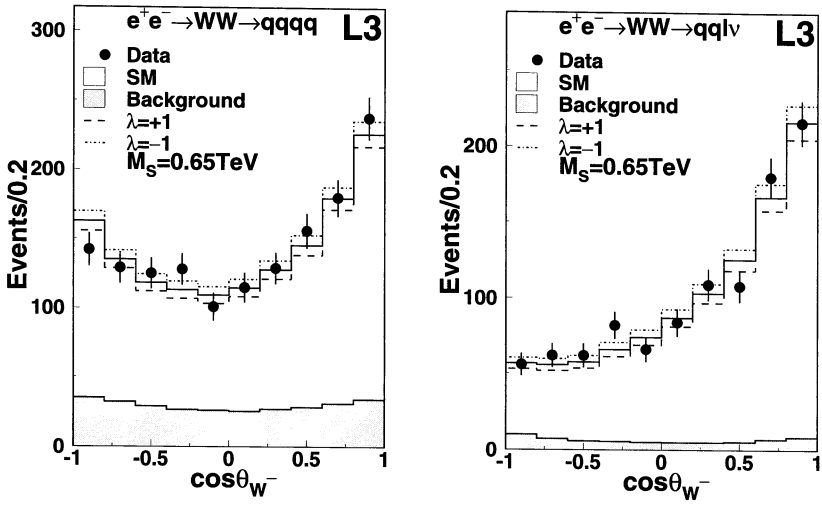

Figure 7.5: *Effects of graviton exchange on the distribution of the W^- production angle $\cos\theta_{W^-}$ for an example $M_S = 0.65$ TeV for fully hadronic WW decays (left) and semileptonic WW decays (right).*

of EXCALIBUR [78] which includes the graviton exchange matrix elements for the WW process [123]. Our measurement of the WW cross section between $\sqrt{s} = 161$ and 189 GeV leads to the following results:

$$\lambda = -1 \; : \; M_S > 0.68 \text{ TeV} \text{ at } 95\% \text{ CL}, \tag{7.22}$$

$$\lambda = +1 \; : \; M_S > 0.79 \text{ TeV} \text{ at } 95\% \text{ CL}. \tag{7.23}$$

Further limits on M_S are obtained from the analysis of ZZ production and $\gamma\gamma$ production, and two-fermion production [125].

7.2 W Mass

In Chapter 6, the analysis of the direct measurement of the W mass in $\mathrm{q\bar{q}q\bar{q}}$ events taken at $\sqrt{s} = 172 - 189$ GeV is described. The following result is obtained:

$$m_{\mathrm{W}} = 80.571 \pm 0.107\,(\text{stat}) \pm 0.034\,(\text{syst}) \pm 0.055\,(\text{FSI}) \pm 0.017\,(\text{LEP}) \text{ GeV}. \tag{7.24}$$

In this section, the consistency of direct W mass measurements and derived, indirect, W mass measurements in the Standard Model will be discussed. Constraints on the Higgs mass in the Minimal Standard Model will be derived. Furthermore some possible improvements on the measurement will be discussed, and some prospects will be given for future W mass measurements.

The W mass is measured at LEP by all four experiments in the $\mathrm{q\bar{q}}\ell\nu$ and $\ell\nu\ell\nu$ channels as well in the $\mathrm{q\bar{q}q\bar{q}}$ channel. The combined result as of March 2002 is [25]:

$$m_{\mathrm{W}}^{\mathrm{LEP2}} = 80.450 \pm 0.039 \text{ GeV}. \tag{7.25}$$

7.2.1 Consistency of W Mass Measurements

The W mass is also measured directly by the CDF and D0 experiments at the Tevatron and much earlier by the UA2 collaboration at CERN. Their combined result is:

$$m_{\mathrm{W}}^{\mathrm{CDF+D0+UA2}} = 80.454 \pm 0.060 \text{ GeV}, \tag{7.26}$$

which agrees well with the LEP measurements. The LEP2 and Tevatron W mass measurements can be averaged with the following result:

$$m_{\mathrm{W}}^{\mathrm{direct}} = 80.451 \pm 0.033 \text{ GeV}. \tag{7.27}$$

Assuming the Standard Model to be valid, one can also derive the W mass from a Standard Model fit to electroweak observables at LEP, SLD, the Tevatron and neutrino scattering experiments. A comparison between the derived, indirect, W mass results and the direct

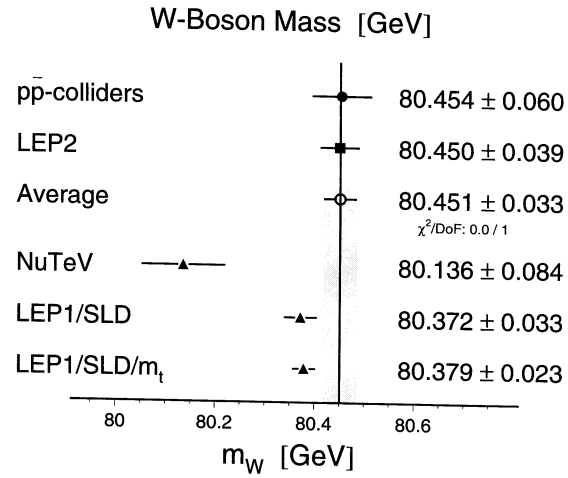

Figure 7.6: *Comparison of direct and indirect W mass measurements. See text for explanation.*

W mass measurements is a test of the consistency of the Standard Model. Also the quality of the Standard Model fit itself is such a test. The fit takes as input a maximum of 19 parameters [24].

Taking as input the Z-pole parameters measured at LEP1 and SLD, the following result is derived:

$$m_{\mathrm{W}}^{\mathrm{LEP1+SLD}} = 80.372 \pm 0.033 \text{ GeV}, \tag{7.28}$$

which is a little lower than, but consistent with, the direct LEP2 and Tevatron measurements. These results are shown graphically in Figure 7.6.

If also the CDF and D0 measurements of the top mass, m_t, are added, the result is:

$$m_{\mathrm{W}}^{\mathrm{LEP1+SLD}+m_t} = 80.379 \pm 0.023 \text{ GeV}, \tag{7.29}$$

consistent with, but more accurate than, the result without the top mass.

The NuTeV experiment has measured neutral to charged current ratios in neutrino-nucleon deep inelastic scattering [126]. From this ratio, the electroweak mixing angle $\sin^2\theta_W$ is derived. Using Equation 2.3, this result can also be expressed as an indirect measurement of the W mass:

$$m_{\mathrm{W}}^{\mathrm{NuTeV}} = 80.136 \pm 0.084 \text{ GeV}. \tag{7.30}$$

This result is 3.5 standard deviations lower than the direct measurements, but also 2.8 standard deviations lower than the indirect results derived from Z-pole observables and the top

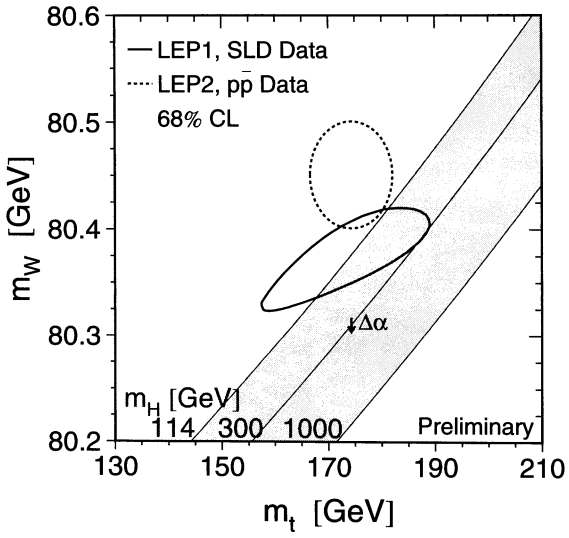

Figure 7.7: *Comparison of direct and indirect W mass and top quark mass measurements. The full ellipse is the result of the Standard Model fit, the dotted ellipse represents the direct measurements. Contours of constant Higgs mass m_{H} are also shown in the plot. The little arrow marked $\Delta\alpha$ represents how these contours move for a change in α, corresponding to its estimated uncertainty.*

mass. The origin of this difference is unknown. The probability of the Standard Model fit including the NuTeV result is only 1.7%.

In Figure 7.7 the direct and indirect W mass results are compared in the $m_{\mathrm{W}} - m_t$ plane [1]. The full ellipse is the result of the Standard Model fit, the dotted ellipse represents the direct measurements. The compatibility of the direct and indirect results beautifully demonstrates the consistency of the Standard Model.

7.2.2 Constraints on the Higgs Mass

Within the Minimal Standard Model, m_{W}, m_t and the Higgs mass m_{H} are correlated, as shown graphically in Figure 7.7. The diagonal curves in the figure are indications of the re-

[1] Also the top mass m_t can be derived from the Standard Model fit; it is also measured directly at CDF and D0.

lationship between m_W and m_t for Higgs masses of 114, 300, and 1000 GeV, fixing the other relevant Standard Model parameters to their measured values. The little arrow marked $\Delta\alpha$ represents how these lines move for a change in α, corresponding to its estimated uncertainty.

Both the direct and indirect W and top mass measurements prefer a relatively light Higgs boson in the Minimal Standard Model. The Standard Model fit described in Section 7.2.1 also fits the Higgs mass m_H. The result of the fit with as input only the Z-pole measurements from LEP1 and SLD and the top mass measurement from CDF and D0 is:

$$m_H^{\text{LEP1+SLD}+m_t} = 100^{+64}_{-41}\ \text{GeV}, \tag{7.31}$$

where the errors represent as usual the 68% CL interval. Note, however, that the errors are far from Gaussian, since the Higgs mass enters logarithmically in the fit.

Using all available data, the result is:

$$m_H^{\text{All Data}} = 85^{+54}_{-34}\ \text{GeV}. \tag{7.32}$$

Leaving the NuTeV result out of the fit results in $m_H^{\text{No NuTeV}} = 81^{+49}_{-32}$ GeV.

The χ^2 curve of the Standard Model fit as a function of the Higgs mass is shown in Figure 7.8. The fit using all available data gives an upper limit on the mass of the Standard Model Higgs boson:

$$m_H < 196\ \text{GeV}\ \ \text{at}\ 95\%\ \text{CL}. \tag{7.33}$$

The shaded band in Figure 7.8 represents the estimated theoretical error due to missing higher order calculations. A further uncertainty arises due to the error on $\Delta\alpha$, as explained in Section 2.1. This error is dominated by the uncertainty on $\Delta\alpha^{(5)}_{\text{had}}$, the contribution of the five light quarks. The full curve shows the fit result with $\Delta\alpha^{(5)}_{\text{had}}$ taken from Reference [19]. The dashed curve is obtained when the more aggressive, theory-driven approach from Reference [127] is used.

7.2.3 Possible Improvements on the Measurement

Some suggestions for improvements on the W mass measurement in the fully hadronic channel are given below:

1. Gluon radiation from any of the four quarks from WW decay can lead to a fifth jet. Such a fifth jet is typically of lower energy than the other jets, and less isolated, but occasionally it is energetic and isolated. Although there is no clear distinction between four-jet events with a broad jet and "true" five-jet events, at some moment it is no longer reasonable to describe the event with only four jets. Nevertheless, in the current analysis the jet clustering algorithm forces the event into four jets. This implies that a fifth jet will be merged with its closest neighboring jet, based on the distance criterion defined in Equation 4.4. Given the fact that the gluon jet is typically close to

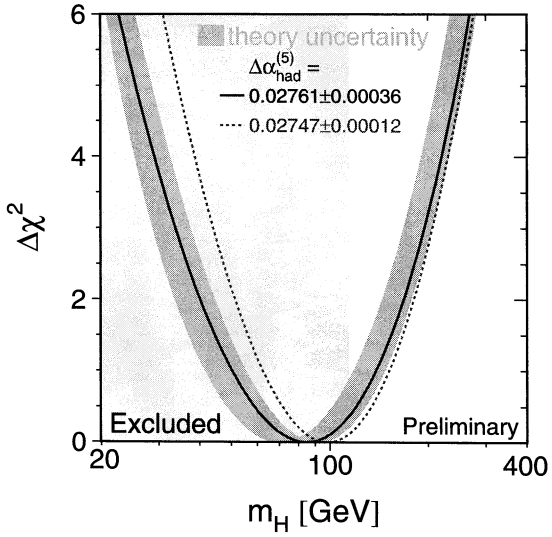

Figure 7.8: χ^2 *of the Standard Model fit as a function of the Higgs mass, taking all available observables as input to the fit. The shaded band represents the lower limit from direct Higgs searches. See text for a discussion of the shaded band and the dashed curve.*

its parent, this will in most cases be correct. However, even with the correct gluon-jet combination, the errors assigned to the jet energy and angles in the kinematic fit are not optimal. If the combination is incorrect, the event is obviously misreconstructed. These problems can be circumvented by treating such events explicitly as 5-jet events. With five jets instead of four, there are ten ways to pair the jets into W's, rather than just three. Improvements in the event reconstruction will be achieved not so much in the best pairing of the ten, but rather in the second and third best. In the mass fit 5-jet events and 4-jet events should be fit separately, for example in bins of y_{45}. First tests have yielded improvements in the order of 5%, without optimization of the analysis.

2. The statistical power of the W-mass measurements can be enhanced by using more of the available information on an event-by-event basis. An excellent example are the 5-jet events described above: it is known that, even after treating the events as proper 5-jet events, the mass resolution gets worse as y_{45} increases. In the mass analysis presented here this kind of information has not been used.

The "ideogram" method [113], which has been used by the Delphi collaboration, allows for a flexible and straightforward combination of available information. The method is therefore well suited for WW analysis and yields a high statistical power.

There is in principle no reason why the reweighting method could not be extended to a multi dimensional likelihood fit, using all available information. In fact, this would even be highly attractive as it is by construction an (asymptotically) efficient method. In practice care has to be taken with the available amount of Monte Carlo statistics. Therefore the maximum number of dimensions that can be used with a reasonable number of bins is probably limited to two or three.

3. With increasing statistics, the W mass measurement, especially in the fully hadronic channel, becomes more and more systematics limited. The systematic errors on the W mass measured in this analysis are discussed in Section 6.5. An error of 30 MeV is assigned to uncertainties in detector response; these uncertainties can still be lowered by further studies on data: in 1999 and 2000 data has been taken corresponding to twice the luminosity used in this analysis. Uncertainties in Bose-Einstein correlations between the decay products of different W's have been experimentally shown to be small [105, 50]. However, uncertainties due to color reconnection, 54 MeV in this thesis, are still large. Color reconnection is being studied experimentally by measuring the energy flow between jets [60], and these studies may well lead to lower uncertainties. Furthermore, the use of cone algorithms in jet reconstruction, as well as disregarding low-momentum particles in the jet finding, could possibly lead to significantly smaller uncertainties due to color reconnection, but only in exchange for an increased statistical error. Uncertainties in fragmentation and hadronization are estimated in this thesis to lead to a systematic error of 20 MeV on the W mass. Further improvements in HERWIG, and better parameter tuning of the generators, are likely to reduce this error significantly.

4. For systematic error studies, the Delphi collaboration has made use of the technique of Mixed Lorentz-Boosted Z events (MLBZ technique) [113], reporting significant improvements in the determination of systematic uncertainties. In this technique, two Z events selected from data taken at $\sqrt{s} \approx m_{\mathrm{Z}}$ are superimposed into one pseudo-event, after boosting the two Z's in opposite directions with a boost corresponding to the boost of a W boson in a WW event. Thus, such a mixed event serves as a quasi-WW event. Advantages of this method are that mixed events are real data, not Monte Carlo, that single Z events can be used many times and thus lead to very good statistics, and that the properties of the original Z event are very well defined (invariant mass m_{Z}, events produced at rest).

   There are, however, differences between WW events and MLBZ events. The different fragmentation scale is not a problem. WW events have a different flavor composition

than Z events, and such effects must be studied and taken into account. The W width differs from the Z width, the W angular distribution differs from the Z angular distribution, ISR is different. After boosting the Z events, jets point to detector regions where they were not actually detected. Clusters change in the boost and in the event mixing, in particular close clusters or tracks, and non-linear jet energy responses are not taken into account.

The problems above are all manageable. However, a serious limitation of the method stems from the fact that detector effects are in general not Lorentz invariant. This can be illustrated by the following example of an effect that is drastically different in the boosted, W-like, frame than in the laboratory, Z, frame. Take a Z-event with two back-to-back jets of 45 GeV. A measurement error of a full degree in the jet-jet angle in this frame will, after the Lorentz boost to a W-like frame where the two jets have an energy of 60 GeV each, correspond to an error of only 0.005°. This means that the effect of this particular measurement error is underestimated by a factor of 200. Turning the argument around, we can also note that an angular mismeasurement of one degree influences the measured W-mass in the W-like frame by a factor of 140 more than in the Z rest frame. Note that it may seem unlikely that a detector effect will affect the jet-jet angle as most effects influence the jet angle itself. However, as the W bosons are likely to be produced in the direction of the beam pipe, the two jets corresponding to the same W are more often than not detected in the same hemisphere. Therefore a systematic effect on the jet angle can easily translate to a systematic effect on the jet-jet angle.

Other detector effects might respond differently to the Lorentz boost, but since the MLBZ method can only be used to estimate the sum of all systematic uncertainties this sum becomes meaningless.

We therefore argue that the MLBZ method can, contrary to what is usually advertised, not be used to determine systematic uncertainties due to detector effects. However, the method still has a very useful application in studying fragmentation effects. Since these are Lorentz invariant, and theorists are confident that the fragmentation of a hadronic Z-boson decay can be safely extrapolated to the hadronisation scale of W-decay, the MLBZ method is a valid tool in this case. Still, careful studies of detector effects are needed also in this case, as the determination of the fragmentation uncertainty is limited by the non-Lorentz invariant detector effects.

7.2.4 Future Prospects

In the near future, the W mass will be measured at the Tevatron $p\bar{p}$ collider by the D0 and CDF experiments, and from 2007 onwards by the ATLAS and CMS experiments at the pp collider LHC. In all these experiments, the W mass is derived in events with leptonic (e or

μ) W decay from the falling edge of the transverse mass spectrum of a charged lepton and a neutrino reconstructed from the missing p_T in the event.

The goal of Tevatron Run 2A is to accumulate an integrated luminosity of 2 fb^{-1} per experiment. This gives approximately 1 million W $\rightarrow \ell\nu$ events per experiment per channel. The statistical error on m_{W} per experiment, combining the e and μ channels, is estimated to be 13 MeV. Systematic errors are dominated by uncertainties in the energy scale of the calorimeters, and the momentum scale of the tracker. Even though control samples like Z $\rightarrow \ell\ell$ and $J/\psi \rightarrow \ell\ell$ are used, the systematic uncertainty on m_{W} from this source is expected to be 15 MeV. Further uncertainties are dominated by uncertainties in the parton distribution functions. Overall, an error of 30 MeV on m_{W} is expected per experiment, or 22 MeV combined.

At the LHC, an integrated luminosity of 10 fb^{-1} (one year of running at an instantaneous luminosity of 10^{33} cm^{-2} s^{-1}) would give some 60 million W $\rightarrow \ell\nu$ events and 6 million Z $\rightarrow \ell\ell$ events. Therefore the statistical error on m_{W} is expected to be very small. Systematic uncertainties at the LHC are similar as at the Tevatron, but the much larger data samples should allow for a better determination of them. Pile-up from multiple interactions in one bunch crossing decreases the resolution of the missing p_T determination, and therefore smears out the falling edge of the transverse mass distribution. At the LHC, the W mass measurement is thus best done at relatively low instantaneous luminosities, and not at 10^{34} cm^{-2} s^{-1}. Overall, ATLAS expects an error of 25 MeV on m_{W} per channel; combining the channels and ATLAS and CMS a final error of 15 MeV is expected.

Clearly, neither the Tevatron nor the LHC will lead to an order of magnitude improvement in m_{W}. For this, a linear electron-positron collider will be needed. At such a linear collider, the W mass is best measured in a threshold scan, as shown for example by studies for the proposed TESLA facility at DESY [128]. At TESLA, an integrated luminosity of 100 fb^{-1} is expected in one year of running around $\sqrt{s} = 161$ GeV, the WW threshold. By changing the beam polarization, the WW cross section and the background can be independently varied, which is of great help in separating the signal and the background. By including a point at $\sqrt{s} \approx 170$ GeV, where the cross section is almost insensitive to m_{W}, selection efficiencies can be constrained. An important pre-requisite for such a threshold scan is an accurate theoretical prediction for the WW cross section around threshold, at a level of 0.1%. This is currently not available, in particular the double-pole approximation used at higher $\sqrt{s}$ is invalid around threshold. Further systematic uncertainties are the accuracy of the beam energy, polarization and luminosity. Overall, an error on m_{W} of 6 MeV seems feasible. Together with a top mass measurement of $\mathcal{O}(100)$ MeV accuracy, this would constrain the Higgs mass to approximately 5%.

Bibliography

[1] E. Fermi, *An attempt of a theory of beta radiation*, Z. Phys. **88** (1934) 161.

[2] C. P. Sargent *et al.*, *Diffusion Cloud-Chamber Study of Very Slow Mesons. II. Beta Decay of the Muon*, Phys. Rev. **99** (1955) 885.

[3] H. Frauenfelder *et al.*, *Parity and the polarization of electrons from CO-60*, Phys. Rev. **106** (1957) 386.

[4] C. S. Wu, E. Ambler, R. W. Hayward, D. D. Hoppes and R. P. Hudson, *Experimental test of parity conservation in beta decay*, Phys. Rev. **105** (1957) 1413.

[5] M. Goldhaber, L. Grodzins, and A. W. Sunyar, *Helicity of neutrinos*, Phys. Rev. **109** (1958) 1015.

[6] R. P. Feynman and M. Gell-Mann, *Theory of the Fermi interaction*, Phys. Rev. **109** (1958) 193.

[7] D. E. Groom *et al.* Particle Data Group, *Review of particle physics*, Eur. Phys. Jour. **C 15** (2000) 1.

[8] O. Klein, in *Les Nouvelles Théories de la Physique*, Institut International de Coopération Intellectuelle, Paris (1938) 6.

[9] S.L. Glashow, *Partial symmetries of weak interactions*, Nucl. Phys. **22** (1961) 579, S. Weinberg, *A model of leptons*, Phys. Rev. Lett. **19** (1967) 1264, A. Salam, in *Elementary particle theory*, ed. N. Svartholm, Almquist and Wiksell, Stockholm (1968) 367.

[10] M. Veltman, *Perturbation theory of massive Yang-Mills fields*, Nucl. Phys. **B 7** (1968) 637, G. 't Hooft, *Renormalization of massless Yang-Mills fields*, Nucl. Phys. **B 33** (1971) 173, ibid. *Renormalizable Lagrangians for massive Yang-Mills fields*, **B 35** (1971) 167, M. Veltman and G. 't Hooft, *Regularization and normalization of gauge fields*, Nucl. Phys. **B 44** (1972) 189, ibid. *Combinatorics of gauge fields*, **B 50** (1972) 318.

[11] F. Englert and R. Brout, *Broken symmetry and the mass of Gauge vector mesons*, Phys. Rev. Lett. **13** (1964) 321, ibid. *Broken symmetries and the masses of gauge bosons*, **13** (1964) 508, P. W. Higgs, *Broken symmetries, massless particles and gauge fields*, Phys. Lett. **12** (1964) 132, P. W. Higgs, *Spontaneous symmetry breakdown without massless bosons*, Phys. Rev. **145** (1966) 1156.

[12] The Gargamelle Neutrino Collaboration, F. J. Hasert *et al.*, *Observation of neutrino-like interactions without muon or electron in the Gargamelle neutrino experiment*, Phys. Lett **B 46** (1973) 138.

[13] The UA1 Collaboration, G. Arnison *et al.*, *Experimental observation of isolated large transverse energy electrons with associated missing energy at* $\sqrt{s}$ = *540-GeV*, Phys. Lett. **B 122** (1983) 103, ibid. *Experimental observation of lepton pairs of invariant mass around 95-GeV/*c^2 *at the CERN SPS collider*, **B 126** (1983) 398, The UA2 Collaboration, M. Banner *et al.*, *Observation of single isolated electrons of high transverse momentum in events with missing transverse energy at the CERN anti-p p collider*, Phys. Lett. **B 122** (1983) 476, The UA2 Collaboration, P. Bagnaia *et al.*, *Evidence for Z0* $\rightarrow$ *e+ e- at the CERN anti-p p collider*, Phys. Lett. **B 129** (1983) 130.

[14] M. Gell-Mann, Acta Physica Austriaca, Suppl. IX **733** (1972), H. Fritzsch, M. Gell-Mann and H. Leytwyler, *Advantages of the color octet gluon picture*, Phys. Lett. **B 47** (1973) 365, D.J. Cross and F. Wilczek, *Ultraviolet behavior of non-Abelian Gauge theories*, Phys. Rev. Lett. **30** (1973) 1343; H.D. Politzer, *Reliable perturbative results for strong interactions*, Phys. Rev. Lett. **30** (1973) 1346.

[15] S. Dimopoulos N. Arkani-Hamed and G. Dvali, *The hierarchy problem and new dimensions at a millimeter*, Phys. Lett. **B 429** (1998) 263.

[16] C. Balázs *et al.*, *Collider tests of compact space dimensions using weak gauge bosons*, Phys. Rev. Lett. **83** (1999) 2112.

[17] The LEP experiments ALEPH, DELPHI, L3, OPAL, and the LEP Higgs Working Group, preprint CERN-EP/2001-055 (2001).

[18] For a review, see for example: P. Fisher, B. Kayser and K. S. McFarland, Annu. Rev. Nucl. Part. Sci. **49** (1999) 481.

[19] H. Burkhardt and B. Pietrzyk, *Update of the hadronic contribution to the QED vacuum polarization*, Phys. Lett. **B 513** (2001) 46.

[20] F. Jegerlehner, *Physics of precision experiments with zs*, Prog. Part. Nucl. Phys. **27** (1991) 1.

[21] M. W. Grünewald, *Experimental tests of the electroweak standard model at high energies*, Phys. Rept. **322** (1999) 125.

[22] M. Veltman, *Second threshold in weak interactions*, Acta Phys. Polon. **B 8** (1977) 475, M. B. Einhorn and J. Wudka, *Screening of heavy Higgs radiative effects*, Phys. Rev. **D 39** (1989) 2758.

[23] BES Collaboration, J. Z. Bai *et al.*, hep-ex/0102003, BES Collaboration, J. Z. Bai *et al.*, *Measurement of the total cross section for the hadronic production by e+ e- annihilation at energies between 2.6-GeV and 5-GeV*, Phys. Rev. Lett. **84** (2000), 594.

[24] The LEP experiments ALEPH, DELPHI, L3, OPAL, the LEP Electroweak Working Group and the SLD Heavy Flavor Group *A combination of preliminary electroweak measurements and constraints on the Standard Model*, preprint LEPEWWG/2002-01 (2002).

[25] G. Myatt, on behalf of the LEP experiments, talk given at the 2002 Rencontres de Moriond, Electroweak Interactions, March 15 2002, Les Arcs, France, to appear in the proceedings.

[26] CDF Collaboration, F. Abe *et al.*, *Measurement of the top quark mass with the Collider Detector at Fermilab*, Phys. Rev. Lett. **82** (1999) 271, plus erratum in Phys. Rev. Lett. **82** (1999) 2808(E), F. Abe *et al.*, *Observation of top quark production in anti-p p collisions*, Phys. Rev. Lett. **74** (1995) 2626, D0 Collaboration, B. Abbott *et al.*, *Measurement of the top quark mass in the dilepton channel*, Phys. Rev. **D60** (1999) 052001, B. Abbott *et al.*, *Observation of the top quark*, Phys. Rev. Lett. **74** (1995) 2632.

[27] P. Chankowski *et al.*, *Delta r in the mssm*, Nucl. Phys. **B417** (1994) 101.

[28] CDF Collaboration, T. Affolder *et al.*, *Measurement of the W boson mass with the Collider Detector at Fermilab*, Phys. Rev. **D64** (2001) 052001, D0 Collaboration, B. Abbott *et al.*, *A measurement of the W boson mass using electrons at large rapidities*, Phys. Rev. Lett. **84** (2000) 222.

[29] D. Bardin, A. Olshevskii, M. Bilenkii, and T. Riemann, *Off-shell W pair production in e+ e- annihilation: Initial state radiation*, Phys. Lett. **B 308** (1993) 403, ibid. **B 357** (1995) 725.

[30] V.A. Khoze V.S. Fadin and A.D. Martin, *On w+ w- production near threshold*, Phys. Lett. **B 311** (1993) 311.

[31] W. Beenakker D.Yu. Bardin and A. Denner, *The coulomb singularity in off-shell w pair production*, Phys. Lett. **B 317** (1993) 213.

[32] W. Beenakker, F. A. Berends and A. P. Chapovsky, *Radiative corrections to pair production of unstable particles: Results for e+ e- → 4 fermions*, Nucl. Phys. **B 548** (1999) 3.

[33] A. Denner, S. Dittmaier, M. Roth and D. Wackeroth, *O(alpha) corrections to e+ e- → W W → 4fermions(+gamma): First numerical results from RACOONWW*, Phys. Lett. **B475** (2000) 127.

[34] S. Jadach, W. Placzek, M. Skrzypek, B. F. L. Ward, and Z. Was, *Precision predictions for (un)stable w+ w- pair production at and beyond lep2 energies*, Phys. Rev. **D65** (2002) 093010.

[35] W. J. Stirling and W. James, *The Measurement of M(W) from the W+ W- threshold cross-section at LEP-2*, Nucl. Phys. **B 456** (1995) 3.

[36] J.M. Moreno J. Orloff J.-M. Frère, M. Tytgat, *Effective operators and extended symmetry*, Nucl. Phys. **B 429** (1994) 3.

[37] D. R. Yennie, S. C. Frautschi and H. Suura, *The infrared divergence phenomena and high-energy processes*, Ann. Phys. **13** (1961) 379.

[38] F. A. Berends, R. Pittau and R. Kleiss, Nucl. Phys. **B 426** (1994) 344.

[39] Y. Kurihara, J. Fujimoto, T. Munehisa and Y. Shimizu, *Hard photon distributions in e+ e- annihilation process by QEDPS*, Prog. Theor. Phys. **96** (1996) 1223.

[40] M. W. Grünewald, G. Passarino *et al.*, Proceedings of the LEP2 Monte Carlo workshop, preprint hep-ph/0005309.

[41] T. Sjöstrand, *High energy physics event generation with PYTHIA 5.7 and JETSET 7.4*, Comput. Phys. Commun. **82** (1994) 74.

[42] G. Marchesini *et al.*, *HERWIG version 5.9: A Monte Carlo event generator*, (1996).

[43] L. Lönnblad, *Ariadne version 4: A program for simulation of qcd cascades implementing the color dipole model*, Comput. Phys. Commun. **71** (1992) 15.

[44] A. Krzywicki and B. Petersson, *Breakdown of hadronic scaling or evidence for clustering"*,, Phys. Rev. **D 6** (1972) 924, J. Finkelstein and R. Peccei, *Bootstrap model of inclusive reactions*, Phys. Rev. **D 6** (1972) 2606, F. Niedermayer, *Dynamical connections between quark fragmentation functions*, Nucl. Phys., **B 79** (1974) 355, A. Casher, J. Kogut and L. Susskind, *Vacuum polarization and the absence of free quarks*,

Phys. Rev. **D 10** (1974) 732, R. D. Field and R. P. Feynman, *A parametrization of the properties of quark jets*, Nucl. Phys. **B 136** (1978) 1.

[45] JADE Collaboration, W. Bartel *et al.*, *Experimental study of jets in electron - positron annihilation*, Phys. Lett. **B 101** (1981) 129, JADE Collaboration, W. Bartel *et al.*, *Particle distribution in three jet events produced by e+ e- annihilation*, Z. Phys. **C 21** (1983) 37, OPAL Collaboration, M. Z. Akrawy *et al.*, *A Model independent observation of the string effect using quark tagging at LEP*, Phys. Lett. **B 261** (1991) 334, L3 Collaboration, M. Acciarri *et al.*, *QCD studies in e+ e- annihilation from 30-GeV to 189-GeV*, Phys. Lett. **B 489** (2000) 65.

[46] S. Banerjee and S. Banerjee, *Tuning of QCD model parameters using LEP data of hadronic Z decays*, L3 Note 1978 (1996).

[47] S. Haywood, *Where Are We Going With Bose-Einstein - a Mini-Review*, RAL Note 94-074 (1994).

[48] L. Lönnblad and T. Sjöstrand, *Modelling bose-einstein correlations at lep 2*, Eur. Phys. J. **C 2** (1998) 165.

[49] M. Acciarri *et al.* L3 Collaboration, *Measurement of Bose-Einstein correlations in* $e^+e^- \to W^+W^-$ *at* $\sqrt{s}$ *approx. = 189* GeV, Phys. Lett. **B 493** (2000) 233.

[50] J. van Dalen, *Bose-Einstein correlations in* e^+e^- *Events*, thesis Katholieke Universiteit Nijmegen (2002), ISBN 90-9015348-9.

[51] B. Andersson and M. Ringner, *Bose-Einstein Correlations in the Lund model*, Nucl. Phys. **B513** (1998) 627.

[52] S. Todorova-Nova and J. Rames, *Simulation of Bose-Einstein effects using space-time aspects of Lund string fragmentation model*, preprint 1. Inst. Rech. Subat. Strasbourg IReS-97-29, hep-ph/9710280 (1997).

[53] K. Fialkowski and R. Wit, *Implementation of Bose-Einstein interference effects in Monte Carlo generators*, Eur. Phys. J. **C2** (1998) 691; K. Fialkowski and R. Wit, *The Bose-Einstein effect and the joint WW decay*, Phys. Lett. **B438** (1998) 154; K. Fialkowski and R. Wit, *On the Bose-Einstein Effect and the W Mass*, Acta. Phys. Pol. **B28** (1997) 2039.

[54] V. G. Kartvelishvili and R. Kvatadze, *Event weights for simulating Bose-Einstein Correlations*, Phys. Lett. **B514** (2001) 7.

[55] U. Pettersson G. Gustafson and P. Zerwas, *Jet final states in w w pair production and color screening in the qcd vacuum*, Phys. Lett. **B209** (1988) 90.

[56] T. Sjöstrand and V. A. Khoze, *On color rearrangement in hadronic w+ w- events*, Z. Phys. **C 62** (1994) 281.

[57] T. Sjöstrand and V. Khoze, *Soft-particle spectra as a probe of interconnection effects in hadronic w+ w- events*, Eur. Phys. J. **C 6** (1999) 271.

[58] G. Gustafson and J. Häkkinen, *Color interference and confinement effects in w pair production*, Z. Phys. **C 64** (1994) 659.

[59] L. Lönnblad, *Reconnecting colored dipoles*, Z. Phys. **C 70** (1996) 107.

[60] D. Duchesneau, *Color Reconnection Studies in W Pair Events at LEP*, talk given at the International Europhysics Conference on High Energy Physics, July 12-18 2001, Budapest, Hungary, to appear in the proceedings; L3 Collaboration, L3 Note 2683, submitted to the International Europhysics Conference on High Energy Physics 2001; P. de Jong, *Color Reconnection in W Decays*, hep-ex/0103018 (2001).

[61] D. Decamp *et al.* ALEPH Collaboration, *A detector for electron-positron annihilations at lep*, Nucl. Instrum. Meth. **A 294** (1990) 121.

[62] P. A. Aarnio *et al.* DELPHI Collaboration, *The delphi detector at lep*, Nucl. Instrum. Meth. **A 303** (1991) 233.

[63] L3 Collaboration, *The construction of the l3 experiment*, Nucl. Instrum. Meth. **A 289** (1990) 35.

[64] K. Ahmet *et al.* OPAL Collaboration, *The opal detector at lep*, Nucl. Instrum. Meth. **A 305** (1991) 275.

[65] Vol.I LEP Design Report, *The lep injector chain*, Preprint CERN–LEP/TH/83–29, CERN, 1983.

[66] J. R. J. Bennett, *Design concept for a 100* GeVe^+e^- *storage ring (lep)*, CERN **77-14** (1977).

[67] S. Myers and C. Wyss, *LEP2 Energy Upgrade*, LEP2 Note 95-34 (1995); S. Myers and C. Wyss, *Prospects for energy and luminosity at LEP2*, CERN 96-01 Vol.1 (1996) 23.

[68] A.P. Colijn, *Measurement of the tau lepton lifetime*, Ph.D. thesis, University of Amsterdam, (1999) ISBN 90-9012782-8.

[69] G. Raven, *Measurement of invisible Z decays*, Ph.D. thesis, Utrecht University, (1995).

[70] O. Adriani *et al.*, *The L3+C Detector, a Unique Tool-Set to Study Cosmic Rays*, submitted to Nuclear Instruments and Methods in Physics Research (2001).

[71] B. Alpat *et al.*, *The design of the l3 silicon microvertex detector*, Nucl. Instrum. Meth. **A315** (1992) 197.

[72] A. H. Walenta, *The time expansion chamber and single ionization cluster measurement*, IEEE Trans. Nucl. Sci. **26** (1979) 73.

[73] R. Brun *et al.*, *GEANT 3, Detector Description and Simulation Tool*, CERN Program Library.

[74] W. Placzek M. Skrzypek, S. Jadach and Z. Was, *Monte Carlo program KORALW-1.02 for W pair production at LEP-2 / NLC energies with Yennie-Frautschi-Suura exponentiation*, Comput. Phys. Commun. **94** (1996) 216.

[75] M. Martinez W. Placzek M. Skrzypek, S. Jadach and Z. Was, *Initial state QED corrections to w pair production at LEP-2 / NLC: Monte Carlo versus semi-analytical approach*, Phys. Lett. **B 372** (1996) 289.

[76] J. Fujimoto *et al.*, *grc4f v1.1: a four-fermion event generator for e+ e- collisions*, Comput. Phys. Commun. **100** (1997) 128.

[77] S. Jadach, J. H. Kuhn and Z. Was, *TAUOLA: A library of Monte Carlo programs to simulate decays of polarized tau leptons*, Comput. Phys. Commun. **64** (1991) 275, M. Jezabek, Z. Was, S. Jadach and J. H. Kuhn, *The tau decay library TAUOLA, update with exact O(alpha) QED corrections in tau → mu. (e) neutrino anti-neutrino decay modes*, Comput. Phys. Commun. **70** (1992) 69, S. Jadach, Z. Was, R. Decker and J. H. Kuhn, *The tau decay library TAUOLA: Version 2.4*, Comput. Phys. Commun. **76** (1993) 361.

[78] R. Pittau F. A. Berends and R. Kleiss, *Excalibur: A Monte Carlo program to evaluate all four fermion processes at LEP-200 and beyond*, Comput. Phys. Commun. **85** (1995) 437.

[79] S. Banerjee and S. Banerjee, *Tuning of Parameters for HERWIG 5.9*, L3 Note 2247 (1998).

[80] S. Banerjee and S. Banerjee, *Tuning of Parameters for HERWIG 5.9 and JETSET 7.4 (without B.E. Correlation)*, L3 Note 2069 (1997).

[81] R. Smits and W. J. Metzger, *Tuning of BE parameters in new Bose-Einstein algorithms using L3 Z decay data*, L3 Note 2596 (2000).

[82] S. Banerjee and S. Banerjee, *Tuning of Parameters for PYTHIA 6.1*, L3 Note 2667 (2001) W. Metzger, private communication.

[83] H. C. Fesefeldt, *Simulation of hadronic showers, physics and applications*, technical report PITHA 85-02, III Physikalisches Institut RWTH Aachen, 1985.

[84] J. E. Hopcroft A. V. Aho and J. D. Ullman, *The design and analysis of computer algorithms*, (Addison-Wesley, 1974).

[85] M. Rescigno S. Banerjee and S. Sarkar, *Hadron group G-factors, l3 note 2394*, (1999).

[86] J. D. Bjorken and S. J. Brodsky, *Statistical model for electron - positron annihilation into hadrons*, Phys. Rev. **D 1** (1970) 1416.

[87] F. V. Tkachev, *The definition of jets*, hep-ph/9901444 (1999).

[88] F. V. Tkachev, *Measuring multijet structure of hadronic energy flow*, Int. J. Mod. Phys. **A12** (1997) 5411.

[89] M. Olsson G. Turnock S. Catani, Yu. L. Dokshitzer and B. R. Webber, *New clustering algorithm for multi - jet cross-sections in* e^+e^- *annihilation*, Phys. Lett. **B269** (1991) 432.

[90] W. Bartel *et al.*, *experimental studies on multi - jet production in* e^+e^- *annihilation at petra energies*, Z. Phys. **C33** (1986) 23.

[91] T. Sjöstrand, *The lund monte carlo for* e^+e^- *jet physics*, Comput. Phys. Commun. **28** (1983) 229.

[92] L. Lönnblad, *Arclus: A new jet clustering algorithm inspired by the color dipole model*, Z. Phys. **C58** (1993) 471.

[93] S. Moretti Yu. L. Dokshitzer, G. D. Leder and B. R. Webber, *Better jet clustering algorithms*, JHEP **08** (1997) 001.

[94] L. Lönnblad S. Moretti and T. Sjöstrand, *New and old jet clustering algorithms for electron positron events*, JHEP **08** (1998) 001.

[95] M. Grünewald, *Selection of Hadronic W-Pair Events with L3 and Determination of the W-Boson Mass*, L3 Note 1908, (1996).

[96] F. James and M. Roos, *'minuit' a system for function minimization and analysis of the parameter errors and correlations*, Comput. Phys. Commun. **10** (1975) 343.

[97] R. Barate *et al.* ALEPH Collaboration, *Measurement of the w mass by direct reconstruction in* e^+e^- *collisions at 172* GeV, Phys. Lett. **B 422** (1998) 384.

[98] T. Rognvaldsson C. Peterson and L. Lönnblad, *Jetnet 3.0: A versatile artificial neural network package*, Comput. Phys. Commun. **81** (1994) 185.

[99] R. Barlow and C. Beeston, *Fitting using finite monte carlo samples*, Comput. Phys. Commun. **77** (1993) 219.

[100] R. Brun *et al.*, *HBOOK: Statistical analysis and histogramming, version 4*, CERN Program Library entry Y250.

[101] B. F. L. Ward, S. Jadach, M. Melles, and S. A. Yost, *New results on the theoretical precision of the lep/slc luminosity*, Phys. Lett. **B450** (1999) 262.

[102] M. Acciarri *et al.*, *Measurement of hadron and lepton-pair production at 130-gev ¡ $\sqrt{s}$¡ 189-gev at lep*, Phys. Lett. **B479** (2000) 101.

[103] P. de Jong, *Fragmentation studies for W Mass and width with a fast detector simulation*, L3 Note 2628 (2000).

[104] L. Lönnblad and T. Sjöstrand, *Modeling bose-einstein correlations at lep 2*, Eur. Phys. J. **C2** (1998) 165.

[105] O. Pooth, *Bose-Einstein Correlations in fully hadronic WW decays at LEP-2*, talk given at the International Europhysics Conference on High Energy Physics, July 12-18 2001, Budapest, Hungary, to appear in the proceedings; L3 Collaboration, L3 Note 2674, submitted to the International Europhysics Conference on High Energy Physics 2001; J. van Dalen, *Bose-Einstein correlations in e^+e^- Events*, PhD. thesis Katholieke Universiteit Nijmegen (2002).

[106] R. Hanbury Brown and R. Q. Twiss, *A new type of interferometer for use in radio astronomy*, Phil. Mag. **45** (1954) 663, Nature **177** (1956) 27, Nature **178** (1956) 1046.

[107] M. Acciarri *et al.* L3 Collaboration, *Study of z boson pair production in* e^+e^- *collisions at LEP at* $\sqrt{s}$ = *189* GeV, Phys. Lett. **B 465** (1999) 363.

[108] M. Acciarri *et al.* L3 Collaboration, *Study of z boson pair production in* e^+e^- *interactions at* $\sqrt{s}$ = *192* GeV *to 202* GeV, Phys. Lett. **B 497** (2001) 23.

[109] A. Leike D. Bardin and T. Riemann, *The process e+ e- → lepton anti-lepton q anti-q at lep and nlc*, Phys. Lett. **B344** (1995) 383.

[110] D. M. Schmidt, R. J. Morrison and M. S. Witherell, *A general method of estimating physical parameters from a distribution with acceptance and smearing effects*, Nucl. Instrum. Meth. **A 328** (1993) 547.

[111] A. Button, *Mass and width of the W boson*, PhD.thesis University of Michigan (1999).

[112] R. Gill, Utrecht University, Mathematical Institute, private communication.

[113] M. Mulders, *Direct measurement of the W boson mass in e^+e^- collisions at LEP*, PhD. thesis University of Amsterdam, (2001) ISBN 90-6464-800X.

[114] OPAL Collaboration, G. Abbiendi *et al.*, *Experimental properties of gluon and quark jets from a point source*, Eur. Phys. J. **C 11** (1999) 217.

[115] M. Acciarri *et al.* L3 Collaboration, *Measurement of mass and width of the w boson at lep*, Phys. Lett. **B 454** (1999) 386.

[116] K. J. F. Gaemers and G. J. Gounaris, *Polarization amplitudes for $e^+e^- \to W^+W^-$ and $e^+e^- \to ZZ$*, Z. Phys. **C1** (1979) 259.

[117] Z. Ajaltouni *et al.*, *Triple gauge boson couplings*, CERN 96-01 Vol.1 (1996) 525, and references therein.

[118] K. J. F. Gaemers and M. R. van Velzen, *Minimal total cross section for $e^+e^- \to W^+W^-$*, Z. Phys. **C43** (1989) 103.

[119] M. Acciarri *et al.* L3 Collaboration, *Pair production of w bosons in e^+e^- interactions at $\sqrt{s}$ = 161* GeV, Phys. Lett. **B 398** (1997) 223.

[120] M. Acciarri *et al.* L3 Collaboration, *Measurement of w pair cross sections in e^+e^- interactions at $\sqrt{s}$= 172* GeV *and w decay branching fractions*, Phys. Lett. **B 407** (1997) 419.

[121] M. Acciarri *et al.* L3 Collaboration, *Measurement of w pair cross sections in e^+e^- interactions at $\sqrt{s}$ = 183* GeV *and w decay branching fractions*, Phys. Lett. **B 436** (1998) 437.

[122] M. Acciarri *et al.* L3 Collaboration, *Measurement of the w pair production cross section and w decay branching fractions in e^+e^- interactions at $\sqrt{s}$ = 189* GeV, Phys. Lett. **B 496** (2000) 19.

[123] K. Agashe and N. G. Deshpande, *Limits on low scale gravity from e+ e- $\to$ W+ W-, Z Z and gamma gamma*, Phys. Lett. **B 456** (1999), 60.

[124] J. Hewett, *Indirect collider signals for extra dimensions*, Phys. Rev. Lett. **82** (1999), 4765.

[125] L3 Collaboration, M. Acciarri *et al.*, *Search for extra dimensions in boson and fermion pair production in e+ e- interactions at LEP*, Phys. Lett. **B470** (1999) 281.

[126] NuTeV Collaboration, G. Zeller *et al.*, *A precise determination of electroweak parameters in neutrino nucleon scattering*, Phys. Rev. Lett. **88** (2002), 091802.

[127] J. F. de Troconiz and F. J. Yndurain, *Calculation of* $\alpha_{\text{Q.E.D.}}$ *on the Z*, preprint FTUAM 01-15, hep-ph/0107318 (2001).

[128] TESLA Technical Design Report, report DESY 2001-011 (2001).

Summary

Weak nuclear interactions play a role in phenomena like nuclear fusion inside the sun, β decay and many other decays of unstable particles. Remarkably, a consistent gauge theory of weak nuclear interactions can only be constructed by a unified description of both weak interactions and electromagnetism: the Standard Model of electroweak interactions. In this model, weak interactions are mediated by spin-1, massive bosons: the charged W bosons, and the neutral Z boson. Both were discovered in 1983 in $p\bar{p}$ collisions at CERN, but their exact properties were not very accurately known until the advent of the e^+e^- collider LEP in 1989.

In the first phase of LEP, the center-of-mass energy was set to be approximately equal to the Z boson mass. In this period, until 1995, the properties of the Z boson were studied in detail. In 1996, the center-of-mass energy of LEP was increased to the threshold of W-pair production, and above that threshold in the years that followed. In this phase of LEP, the properties of the W boson and its production process could be studied. It is this phase of LEP, and more precisely the data taken from 1996 to 1998, that is the topic of this thesis. In this thesis, a measurement of the production cross section of W-pairs is presented, as well as a measurement of the W boson mass, for events where both W's decay hadronically.

This thesis consists of several parts. In Chapter two a brief summary of the relevant theory is given. Subsequently, the LEP accelerator and the L3 detector are described in Chapter three. Chapter four describes how the information from the individual subdetectors is combined. In this chapter the energy determination of clusters and jets is described, and properties of individual W's are derived. Since the initial state is fully known, up to the overall relatively small effects of photon radiation, the accuracy of the reconstruction is improved by fitting the event under the constraints of energy and momentum conservation. For the W mass reconstruction further fits are performed, constraining the two reconstructed W masses to be equal.

In Chapter five, this information is used to select fully hadronically decaying W-pair events from the data, i.e. events with four hadronic jets. The dominant background for this process is the production of $q\bar{q}$-pair events with one or more hard gluons. The event selection therefore starts by requiring a clear four-jet signature, with a high multiplicity and little missing energy and momentum. This selection is 92% efficient for signal and reduces the background considerably. The remaining background resembles the signal closely. A

multivariate analysis, in this thesis implemented in the form of a neural network, is used to separate this background from the signal. This yields a single variable with a low value for background-like events and a high value for signal-like events. This event-by-event information is used in a fit to the data to derive the respective signal and background production rates with their statistical uncertainties. Systematic uncertainties are estimated using Monte Carlo studies and are dominated by fragmentation uncertainties. The cross section results for the various centre-of-mass-energies are given in Tables 5.2 and 5.4, and are illustrated graphically in Figure 5.13 on page 80.

As the W cross section at the production threshold at $\sqrt{s} = 161$ GeV is strongly dependent on the W mass, the measured cross section at this energy has been used to determine the W mass. A value of $m_{\mathrm{W}} = 81.33^{+1.17}_{-0.72} \pm 0.03$ GeV is derived.

In Chapter six, the W mass is determined directly using the W decay products. To select W pair events a minimum value for the neural network output value is required. The W mass is determined from the event sample using a likelihood fit. The event-by-event likelihood is determined using a Monte Carlo reweighting technique. The W mass result using the data from $\sqrt{s} = 172$ GeV to $\sqrt{s} = 189$ GeV is

$$m_{\mathrm{W}} = 80.571 \pm 0.107\,(\mathrm{stat}) \pm 0.034\,(\mathrm{syst}) \pm 0.055\,(\mathrm{FSI}) \pm 0.017\,(\mathrm{LEP})\ \mathrm{GeV}.$$

The dominant systematic error is due to uncertainties in the modelling of color reconnection, a process that can occur between the quarks in the final state.

The implications of the measurements are discussed in Chapter seven. Several models different from the Standard Model predict, among other things, a different W-pair production rate. Using the measured W-pair production cross section, limits can be found for several anomalous couplings. These are possible differences of observed particle-particle interactions with respect to Standard Model predictions. In particular, three limits are found:

$$\begin{aligned} -0.45 < \ & \Delta g_1^Z & < 0.50 \text{ at } 95\% \text{ CL} \\ -0.47 < \ & \lambda_\gamma & < 0.56 \text{ at } 95\% \text{ CL} \\ -0.7 < \ & \Delta\kappa_\gamma & < 1.6 \text{ at } 95\% \text{ CL}. \end{aligned}$$

Using the measured cross sections for W-pair production where one or two of the W bosons decays leptonically, the W branching fractions can be determined. Assuming lepton universality, the following results are obtained:

$$\begin{aligned} B(W \to \mathrm{q\bar{q}}) &= (68.20 \pm 0.68 \pm 0.33)\% \\ B(W \to \ell\nu) &= (10.60 \pm 0.23 \pm 0.11)\%. \end{aligned}$$

The W branching fractions are dependent on the six elements V_{ij} of the Cabibbo-Kobayashi-Maskawa quark mixing matrix not involving the top quark, in particular V_{cs}. Using the measured W branching fractions, we derive:

$$|V_{\mathrm{cs}}| = 1.008 \pm 0.032 \pm 0.016.$$

In certain models beyond the Standard Model the W boson can decay to final states unobservable to the detector. Using the measured and predicted cross sections, it can be shown that, at 95% CL, the invisible W width is less than 52 MeV.

A recent model involving gravity has hypothesised the existence of extra dimensions, which are curled up to very small sizes, not observable to us. The existence of these dimensions influences the W^+W^- cross sections due to the existence of gravitons, whose interactions are described in terms of the scale M_S and a factor λ which is of the order of unity. For values of $\lambda = \pm 1$ the following limits are obtained:

$$\begin{aligned} \lambda = -1: \quad & M_S > 0.68 \text{ TeV} \quad \text{at } 95\% \text{ CL}, \\ \lambda = +1: \quad & M_S > 0.79 \text{ TeV} \quad \text{at } 95\% \text{ CL}. \end{aligned}$$

The W mass derived in this thesis can be used as a check of the validity of the Standard Model. In Figure 7.6, the direct W and top quark mass measurements are compared to the predictions calculated using a multitude of measurements. The agreement between these quite differently derived results beautifully confirms the consistency of the Standard Model.

Taking a different approach, we can assume the validity of the Standard Model and use the world data set, including the direct W and top mass measurements, to obtain a prediction for the mass m_{H} of the at this moment still unobserved Higgs Boson:

$$m_{\mathrm{H}}^{\mathrm{All\,Data}} = 85^{+54}_{-34} \text{ GeV}.$$

Samenvatting

Zwakke wisselwerkingen spelen een rol in processen zoals kernfusie in de zon en radioactief verval. Het is opmerkelijk dat een consistente theorie van deze zwakke wisselwerkingen slechts verkregen kan worden door de zwakke kernkracht onder één noemer te brengen met electromagnetische krachten: het Standaard Model voor electrozwakke wisselwerkingen. In dit model worden de zwakke wisselwerkingen gedragen door massieve deeltjes: de geladen W bosonen en het neutrale Z boson. Beide zijn in 1983 in proton-antiproton botsingen ontdekt op CERN. Met de komst van de electron-positron versneller LEP op CERN in 1989 werden verdere metingen mogelijk gemaakt.

In de eerste fase van LEP was de zwaartepuntsenergie afgesteld op ongeveer de massa van het Z boson. Hierdoor was het mogelijk om uit een botsing van een electron op een positron een Z-boson te maken. In deze periode, die tot 1995 duurde, zijn op deze wijze de eigenschappen van het Z boson uitgebreid bestudeerd. In 1996 werd de zwaartepuntsenergie verhoogd tot de drempelwaarde voor W paar productie en vervolgens tot energieën boven deze drempelwaarde in de jaren daarna. In deze fase van LEP konden de eigenschappen van het W boson en het productieproces van dit deeltje worden bestudeerd. Deze periode, en dan met name de tijd van 1996 tot 1998, is het onderwerp van mijn proefschrift. In dit proefschrift beschrijf ik de meting van de werkzame doorsnede van W boson productie en een meting van de massa van het W boson. In beide gevallen beperk ik me tot gevallen waarbij de W-bosonen ieder in twee quarks vervallen. Deze quarks worden in de detector zichtbaar als nauwe bundels van hadronen, de zogenaamde jets.

Dit proefschrift bestaat uit verscheidene delen. In hoofdstuk twee geef ik een samenvatting van de relevante theorie. Vervolgens beschrijf ik in hoofdstuk drie de LEP versneller en de L3 detector. Hoofstuk vier beschrijft hoe de informatie uit de verschillende subdetectoren wordt gecombineerd. In dit hoofstuk beschrijf ik ook de bepaling van de energie van clusters and jets en worden de eigenschappen van individuele W's bepaald.

In hoofdstuk vijf wordt beschreven hoe ik het signaal van W paar productie probeer te onderscheiden van de achtergrond. Dit is nodig omdat er ook veel gevallen zijn die erg lijken op W paar gevallen. Op de drempelenergie voor W paar productie is de belangrijkste achtergrond zelfs een factor 100 groter dan het signaal! Omdat ik zoek naar een eindtoestand met vier quarks begint de selectie met de eis van een duidelijk vier jet geval. Deze selectie is 92% efficient voor het signaal en reduceert de achtergrond aanzienlijk.

De overblijvende achtergrond lijkt heel erg op het signaal en daarom wordt er vervolgens een neuraal net gebruikt om het signaal verder te scheiden van de achtergrond. Dit neurale

netwerk geeft uiteindelijk één variable met een lage waarde voor achtergrond-achtige gevallen en een hoge waarde voor signaal-achtige gevallen. De resultaten voor de werkzame doorsneden voor de verschillende zwaartepuntsenergieën worden gegeven in de tabellen 5.2 en 5.4, en worden grafische weergegeven in figuur 5.13 op pagina 80.

Doordat de werkzame doorsnede voor W paar productie op de drempelwaarde sterk afhangt van de W massa, kan de gemeten waarde voor de werkzame doorsnede worden vertaald naar een W massa. De waarde voor de W massa die op deze manier is bepaald is $m_{\mathrm{W}} = 81.33^{+1.17}_{-0.72}$ GeV.

In hoofdstuk zes wordt de W massa direct bepaald door gebruik te maken van de metingen van de W vervalsprodukten. Dit gebeurt met behulp van een zogenaamde Monte Carlo simulatie. Dit is een verzameling gesimuleerde gevallen, die er net zo uitzien als de echte metingen en dus in feite een soort namaak data zijn. De W massa wordt nu bepaald door meerdere sets namaakdata te maken met verschillende W massa's. Door nu te kijken welke set het beste overeenkomt met de echte data wordt de W massa bepaald. Een groot deel van hoofdstuk zes wordt in beslag genomen door systematische studies naar de kwaliteit van de Monte Carlo simulatie, en de mogelijke invloeden daarvan op de W massa meting. Ik vind uiteindelijk het volgende resultaat:

$$m_{\mathrm{W}} = 80.57 \pm 0.13 \text{ GeV}.$$

De implicaties van deze metingen worden besproken in hoofdstuk zeven. Verschillende alternatieven voor het Standaard Model voorspellen onder andere een andere werkzame doorsnede voor W paar productie. Met de gemeten werkzame doorsnede voor W paren kunnen er uitspraken gedaan worden over de waarschijnlijkheid van deze theorieën. Zo is onder andere gekeken naar de manier hoe bepaalde deeltjes aan elkaar koppelen, bijvoorbeeld naar de manier hoe een Z boson naar twee W bosonen kan vervallen. Er zijn geen aanwijzigingen gevonden voor afwijkingen van het Standaard Model.

Door gebruik te meken van de werkzame doorsnedes voor W paar productie waarin een van de twee W's vervalt in een lepton en een neutrino, kan bepaald worden hoe waarschijnlijk het is dat de W naar twee quarks vervalt. We vinden dat dit in $68.2 \pm 0.8\%$ van de gevallen gebeurt.

De W massa die in dit proefschrift is bepaald kan worden gebruikt als een test voor de geldigheid van het Standaard Model. In Figuur 7.6 worden de direct gemeten W-boson en top quark massa's vergeleken met de voorspellingen die zijn berekend met behulp van een grote hoeveelheid andere metingen. De overeenkomst tussen deze heel verschillende bepalingen is een mooie bevestiging van de consistentie van het Standaard Model.

Een andere benadering is om de geldigheid van het Standaard Model niet te testen, maar juist aan te nemen. Alle metingen van Standaard Model grootheden, waarvan de in dit proefschrift gemeten mass m_{W} er een is, kunnen dan gecombineerd worden. Dit geeft vervolgens een voorspelling voor de massa m_{H} van het op dit moment nog niet waargenomen Higgs boson:

$$m_{\mathrm{H}}^{\mathrm{All\,Data}} = 85^{+54}_{-34} \text{ GeV}.$$

Acknowledgements

Many people have contributed to this thesis and to the work described in it. This is probably true for every thesis, but as I got RSI halfway through the adventure it is certainly more true for me. Many people lent me their hands, time, patience and often even their brain. Alex, Joana, Martijn , Pieter Jan, Sandra: "thank you" doesn't even begin to express my feelings.

Alex, your big knowledge combined with your kind heart made asking your help very tempting, and especially when I was doing my mass analysis using voice recognition software your help was invaluable. By the time that was done I think your office mate also recognized my voice.

But despite all the help I got from other people the person who certainly spent most time on my thesis (apart from me) is Paul de Jong. Paul, I think your name should also appear as an author. You started working with me when my health was bad and continued despite the fact that it kept getting worse. There was a period when you seemed to have more faith in a happy end than I did, and I cannot tell you how happy I am that you were right. Still, the lack of progress must have exasperated you on many occasions. I don't think I have thanked you often enough during the long, long period of writing but let me be clear about it now: this thesis would not have been finished if it was not for you and for that I will always be grateful.

Going back to the start of this thesis, I want to thank Frits Erné for having confidence in me, starting by hiring me and later by giving me a lot of freedom during my time in Geneva. It is a pity we didn't finish this thesis together. I want to thank Frank Linde for taking over as my main promotor. Frank, thanks as well for your continued belief in me when my health got worse, and for your flexibility. I have appreciated your direct style and admired your lightning-fast brain on many occasions. Paul, apart from, greatly, appreciating the enormous amount of help you gave me I also want to thank you for your many useful suggestions and your infinite supply of constructive ideas as a co-promotor. At CERN I have enjoyed sharing an office for a while with Gerjan Bobbink. Gerjan, thank you for keeping the bureaucratic stuff far away from me as well as for your kindness and your interest.

I have enjoyed working in the L3 collaboration in general and in the W physics group in particular. Alan, Arno, Luca, Mario, Raja and all the others I forgot to mention: thanks for the interesting discussions and the friendly atmosphere. Alex, in the times when I could still type abundantly I enjoyed our fruitful collaboration very much. A very special thanks goes to Martin Grünewald. Martin, when I was new in the W group you gave me excellent

guidance and later you followed up with excellent ideas whenever I needed. Asking your advice was always very useful.

Niels Kjaer always came with challenging and educational ideas from the DELPHI camp, thanks.

Kees Huyser, thanks a bundle for the, of course last minute, help with the intricate adobe programs.

To everybody the L3 group at NIKHEF, whose only students nowadays are Mark and Vinod, my thanks for the interesting discussions and the help. Gerhard, thanks for teaching me how to catch all those interesting bugs that from time to time popped up in my code.

For helping me understand the statistics mystery that absolutely nobody I knew could figure out I want to thank professor Richard Gill. In my opinion the experimental HEP community should consult statisticians more often.

For the dinners in Geneva, Amsterdam or wherever they took place, for the skiing with the flying dutchman, for supporting me every time I was demotivated, for the bridge adventures, for the parties and simply for all the nice times we had together my thanks goes to Alan, Ann & André, Ari, Bart, Bert & Tanja, Bob, Chris, Ernst, Frank & Tasja, Frenk, Ilmar, Ivo & Julia, Jannes, Lisbet, Marat, Martijn, Martin, Michiel, Mike & Nienke, Mirna & Gerhard, Myfanwy, Patrick, Pieter Jan & Ludmila, the René's of all ages, Simon, Saali and last but not least Sandra & Jord, who could easily open a restaurant and finally got me cooking. Alex, your subtle & cynical humor cheered me up on many occasions; it was great having you around! A very warm thanks goes to Kaia & Rego: there were weeks when I spent more time at your place than at my own. Without you my time in Geneva would not have been the same. Daniel, thanks for all the wonderful and on occasion very lively discussions. You have an amazing mind. Marianne, thanks for the friendship and support.

Professor Gerard 't Hooft kindly provided me the calculations used for my cover, thank you very much!

Of the people who are helping me overcome my RSI I want to thank Peter van Kervel for continuing to treat me even while he was writing a book. The people at Physical Sense developed a new way of looking at RSI, contradicting much of the existing "knowledge". Thanks for taking me in and make me finally get better! Jelle, Riet: you are geniuses. Henry, thanks for teaching me all the right moves again, and for all the patience!

Mijn vader, mijn moeder en mijn zus hebben altijd onvoorwaardelijk van me gehouden. Bedankt voor alles!

Joana, your love and support were simply invaluable. Without you the "laadste loodjes" would have been much heavier. I love your merry character, the way you enjoy life, and, of course, you. Te amo muito!

Dank jullie wel!